Dissertation Submitted to
Graduate School of Science of Osaka University
for the Degree of Doctor of Physics

Photoproduction of multi-kaons in an effective Lagrangian approach

Huiyoung Ryu

2013

Research Center for Nuclear Physics (RCNP), Osaka University
Mihogaoka 10-1, Ibaraki, Osaka 567-0047, Japan

OSAKA UNIVERSITY

Dissertation Submitted to

Graduate School of Science of Osaka University
for the Degree of Doctor of Physics

Photoproduction of multi-kaons in an effective Lagrangian approach

Huiyoung Ryu

2013

Research Center for Nuclear Physics (RCNP), Osaka University
Mihogaoka 10-1, Ibaraki, Osaka 567-0047, Japan

OSAKA UNIVERSITY

Acknowledgement

First of all, I would like to sincerely express my gratitude to the supervisor, Professor Atsushi Hosaka for enlightening discussion, helpful suggestions and continuous encouragements. I also appreciate Professor Hiroshi Toki (土岐　博　先生) for his advice and comments. He himself is a one of the good standard scientist. I have been happy to study at RCNP and I will remember their kindness and passion for physics.

The work presented in this thesis has been done with my collaborators, Professor Hyun-Chul Kim (Inha university), Doctor A. Titov (JINR), Professor Yongseok Oh (Kyunbook Univ.). I would like to thank them all again for the fruitful collaborations and advices as a senior.

I also appreciate the five-membered committee for my graduation, Prof. Hosaka (保坂　淳　先生) , Prof. Nakano (中野貴志　先生) , Prof. Kubota (窪田高弘　先生) , Prof. Noumi (野海博之　先生) and Prof. Ogata (緒方一介　先生). Their fruitful advices are very helpful to improve my thesis and presentation. I will keep in mind their questions and comments.

I also would like to appreciate to MEXT scholarship to support my studying at RCNP in Osaka universty. Many staffs in the department of science have helped me to graduate and learn Japanse culture.

Finally I express my thankfulness to my lovely wife Kyungmoon Jung for generous understanding of my study in foregin country and taking care of our children.

Abstract

Photoproduction of strange particles at medium energies helps us understand the dynamics of strangeness production.In this thesis, several photoproduction processes of multi-kaons are investigated in an effective Lagrangian method.

In one kaon photoproduction, we review three reactions with different Lambda hyperons, Lambda(1116), Lambda(1405) and Lambda(1520). By using them, basic reaction dynamics and its relevance with hadron structure are discussed. Special emphasis is put on the meaning of the form factor, which is an important ingredient of the reaction dynamics.

In two kaon photoproductions, first we study hidden strangeness production associated with the phi-meson production. It has provided puzzles for a long time as an OZI suppress process. Several attempts have been made so far, however, with not much success. To approach the problem, we perform an elaborated analysis by including hadronic rescattering processes near the threshold region in addition to the conventional Pomeron exchange at high energies. We have then found that the rescattering though Lambda(1520) resonance could provide significant contribution near the threshold which mimics the bump like structure in the cross section observed in the latest experimental data from the LEPS group by carefully choosing the form factor. We have then studied, as a prediction of our model, spin density matrices which are sensitive to the spin-parity quantum numbers of a t-channel exchanged particle. We have found results which are consistent with the experimental data, indicating that spin-parity in the t-channel is dominated by natural parity. This is the first result and is nontrivial so far. Thus our study indicates the importance of the hadronic process of the phi-photoproduction near the the threshold region while the Pomeron dynamics dominates in the high energy region.

As another process of two kaon production, we study Ξ baryon production and have obtained once again results consistent with the existing data.

Finally we have studied the three-kaon production associated with Ω baryon. This is a totally new theoretical study and provids an estimate for the total production rate. We found that the rate is about factor ten smaller than what we naively expect from the extrapolation from one to two kaon productions.

Contents

List of Figures

List of Tables

Part I

Introduction and review

1

Introduction

1.1 Historical review of hadron physics

Modern nuclear physics started with the obervation of H. Becquerel[1]. After Becquerel's obervation, Marie Curie and her collaborators found radioactivity. Soon after that period, Ernest Rutherford had invastigated inside of atom.

Hardron physics started with the prediction of Yukawa Hideki[2]. In 1935, he predicted the field quantum with a finite mass to explain the interaction between nucleons. Even though his prediction of pi meson is the important step to explain thet strong interaction, it was found that pi meson itself is not the fundamental quantum of strong force for several reasons. In 1954, Yang-Mills theory was proposed as the simplest non-Abelian gauge theory. It was the first step to explain nuclear force using the gauge theory.

After invention of the particle accelerator, physicist had found that there are so many hadrons. Sakata tried to expain mesons and baryons using proton, neutorn and Λ. His work and similar invastigation had tried to explain *too many* hadrons using more fundamental particles. Those *too many* hadrons are rearranged systematically by the quark model suggested by M. Gell-Mann and G. Zweig.

In 1967, S. Weinberg proposed 'a model of leptons' which became the starting point of the standard model. And asymptotic freedom of QCD was discovered by t'Hooft (Holland), Grass and Wilczek (USA) and Politzer (USA) independently.

[1] Antoine Henri Becquerel (1852-1908) : French physicist. He won the 1903 Nobel prize in Physics with Marie Curie and Pierre Curie

[2] Yukawa Hideki (23 January 1907 – 8 September 1981) a Japanese theoretical physicist and the first Japanese Nobel laureate.

Table 1.1: Timeline of modern hadron physics

	1896	A. H. Becquerel reported the rays emitted from uranium.
	1929	The first particle accelerator
Y. Hideki predicted 100 MeV mass meson.	1935	
π^+ was discovered	1947	$K^0 \to \pi^+ + \pi^-$ was discovered
CERN was founded	1954	Yang-Mills theory
The Sakata model	1956	
Ω^- was predicted in the quark model	1962	
	1964	$K^- p \to \Omega^- K^+ K^0$ was discovered
	1967	Model of leptons
The discovery of *asymptotic freedom*	1973	
	1997	Spring-8 was opened for users.
Higss-like particle was reported.	2012	

1.2 Effective field theory and symmetries

1.2.1 Effective field theory

Strong interaction is described by Quantum Chromodynamics. However, at low energy, it is not easy to study the dynamics of strong interaction directly from QCD. The purpose of the effective Lagrangian method is to represent in a simple way the dynamical content of a theory in the low energy limit, where effects can be incorporated into a few constants. The basic strategy is to write down the most general set of Lagrangians consistent with the symmetries of the theory.

To construct the effective Lagrangian, S. Weinberg introduced the guiding principal or theorem in 1979. The effective field theory is based mainly on a "theorem" suggested by [1]:

If one writes down the most general possible Lagrangian, including all terms consistent with assumed symmetry principals, and then calculates matrix elements with this Lagrangian to any given order of perturbation theory, the result will simply be the most general possible S-matrix consistent with analyticity, perturbative unitarity, cluster decomposition and the assumed symmetry principles.

According to Weinberg's theorem, we can construct the most general effective Lagrangian for the strong interaction with the relevant symmetries. The Lagrangian has therefore an infinite number of terms and thus an infinie number of free parameters. They have to be obtained by fitting to experiment or lattice results. For certain physical problems, one can calculate Feynman diagrams with a proper Lagrangian set.

1.2.2 Symmetries of QCD Lagrangian

Here we breifly review symmetries which are base or guidelines for construction of effective Lagrangian.

Gauge symmetry: Quantum chromodynamics is a quantized non-Abelian gauge field theory. The gauge field theories are of a particular kind of field theories which are based on the gauge principle. The gauge principle is the requirement that the theory be invariant under the local gauge transformation. Quantum electrodynamics can be constructed by the phase transformation of the Abelian gropu $U(1)$, while Quantum chromodynamcis can be done by non-Abelian phase transformation of $SU(3)$, whose representations are identified with the color degrees of freedom.

Chiral symmetry: From the Dirac equation for a massless particle, we get the following chial fields:

$$\psi_L = \Gamma_L \psi \,, \quad \psi_R = \Gamma_R \psi. \tag{1.1}$$

where the matrices $\Gamma_{\substack{L\\R}} \frac{1}{2}(1 \pm \gamma_5)$ are chirality projection operators and ψ is a solution of the Dirac equation. $\Gamma_{R,L}$ obey the following properties:

$$\Gamma_L + \Gamma_R = 1\,, \quad \Gamma_L\Gamma_L = \Gamma_L\,, \quad \Gamma_R\Gamma_R = \Gamma_R\,, \quad \Gamma_L\Gamma_R = \Gamma_R\Gamma_L = 0\,. \tag{1.2}$$

We can apply this chirality decomposition to a Lagrangian for a massless noninteracting fermion.

$$\mathcal{L} = i\bar{\psi}\partial\!\!\!/\psi = \mathcal{L}_L + \mathcal{L}_R, \tag{1.3}$$

where

$$\mathcal{L}_{L,R} = i\bar{\psi}_{L,R}\partial\!\!\!/\psi_{L,R} \tag{1.4}$$

These Lagrangian densities are invariant under the global chiral phase transformations

$$\psi'_{L,R} = e^{-i\alpha_{L,R}}\psi_{L,R}\,, \tag{1.5}$$

where the phases $\alpha_{L,R}$ are constant. Using these left- and right-handed fields, ψ_L, ψ_R, we can construct the Lagrangian which satisfies chiral symmetry as follows:

$$\mathcal{L} = -\frac{1}{2}\mathrm{tr}[G_{\mu\nu}G^{\mu\nu}] + \bar{\psi}_L i\gamma^\mu D_\mu\psi_L + \bar{\psi}_R i\gamma^\mu D_\mu\psi_R\,, \tag{1.6}$$

$$G_{\mu\nu} = \partial_\mu A_\nu - \partial_\nu A_\mu - ig[A_\mu, A_\nu]\,, \quad D_\mu = \partial_\mu - igA_\mu\,, \quad A_\mu = \sum_a T^a A^a_\mu, \tag{1.7}$$

where $A^a_\mu(a = 1 \sim 8)$ are the gluon fields, $T^a = \lambda^a/2$ are the generators of the color SU(3) group with Gell-Mann matrices λ^a, and g is the gauge coupling constant.

Discrete symmetry: Invariance of the physics under a transformation means that quantity can be represente by unitary operator. Parity (P) and charge conjugation (C) are discrete groups and they are conserved in both QCD and QED, whereas weak interacitons do not respect these sysmetries.

1.3 Strangeness particle in the hadron physics

In 1962, Gell-Mann and Neèman predicted a new baryon, Ω^-, with $S = -3$, $J^P = 3/2^+$, and a mass of about 1670 MeV [77]. After their prediction, the $\Omega^-(1670)$ was discovered at BNL [74] in 1964, which confirmed the hypothesis of SU(3)$_F$. The Babar Collaboration measured the spin of the Ω^- using $\Xi^0_c \to \Omega^- K^+$, $\Omega^-_c \to \Omega^- K^+$ and $\Omega^- \to \Lambda K^-$ events under the assumption that the charm baryons have spin 1/2, as expected form the quark model, the angular distribution of Λ from Ω decay is cossistent with spin assignment 3/2 for the Ω^- and inconsistent with all half-integer spin assignments [75].

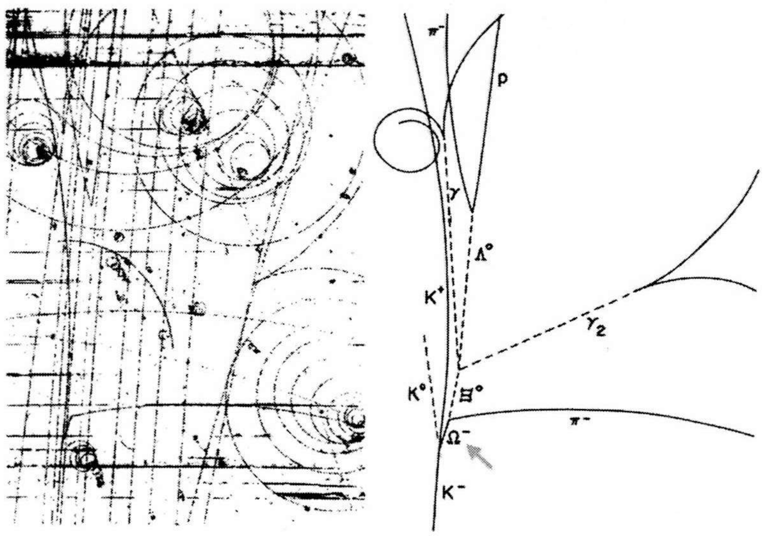

FIG. 1.1: The discovery of a hyperon with strangeness minus three. Photograph and line diagram of event showing decay of Ω^-. These figures are taken from [74].

FIG. 9.1 shows the Ω^- line in the bubble chamber and FIG. 1.2 shows the spin predictions of the $\Omega-$ baryon and the experimental data.

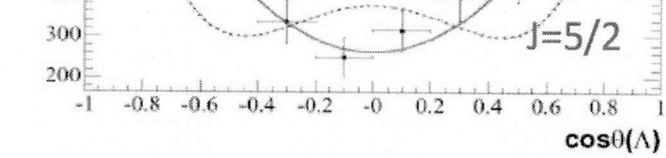

FIG. 1.2: Mesearment of Ω^-. The green, red and blue lines are their expection for the spin of Ω^-. Data are taken from [75].

1.3.1 Ξ and Ω production

Very few Ω/Ξ baryons have been identified in the last 50 years. Even fewer have their quantum numbers determined. Kaon beam was the primary source for the discoveries of Ω/Ξ. But photon beam could be a powerful alternative.

Flavor SU(3) symmetry predicts the existence of as many Ξ resonances [15]. However, not much is known about these resonances. Recently, the CLAS Collaboration at the Thomas Jefferson National Accelerator Facility (JLab) started a cascade physics plan [16]; in particular, the feasibility to do cascade baryon spectoscopy via photoproduction reactions such as $\gamma p \to K^+K^+\Xi^-$ and $\gamma p \to K^+K^+\pi^-\Xi^0$ [16, 17].

Table 1.2: Some Ω/Ξ baryons

	$(J)^P$	M (MeV)	Γ (MeV)	
Ξ	$(1/2)^+$	1318		+ is the quark model prediction
$\Xi(1530)$	$(3/2)^+$	1530	9.1	
$\Xi(1690)$	$(1/2?)^?$	1690	< 30	
$\Xi(1820)$	$(-3/2?)^-$	1823	24	
$\Xi(1950)$	$(?)^?$	1950	60	
Ω	$(3/2)^+$		1672	$(3/2)^+$ is the quark-model prediction
$\Omega(2250)$	$?^?$	2250		

Table 1.2 shows our recent knowlodge of Ω/Ξ baryons. We have a few information about them and theri dynamcis is not well known.

1.3.2 ϕ meson (1020) photoproduction

$\gamma p \to \phi p$ scattering process is very special and interesting phenomenon. Evne though this process violates OZI rule shown in FIG 1.3, that process is not suppressed.

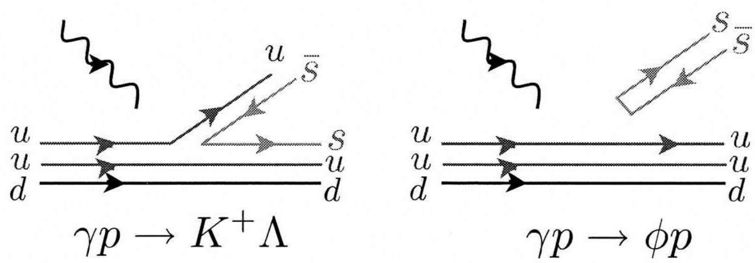

FIG. 1.3: Strangness particle production processes

In this point of view, this special property of ϕ meson photoproduction is very good subject to investigate the hidden strangeness in the hadronic scattering process. In the present thesis, we would like to introduce several hadronic approach to explain ϕ meson photoproduction. In the beginning, Pomeron and one meson exchange process are reviewed. Next we would like to explain one exotic particle exchange and rescattering process.

1.3.3 General questions for the open strangeness physics

The production of open strangeness in photo-induced reactions at intermediate energies allows studies of the transition from the conventional hadron dynamics to the underlying dynamics of quarks, since a strange quark and antiquark must be created.

The questions which gave the motivation for this work are:

1. *Do quark degrees of freedom control the open strangeness production?*

2. *Does chiral symmetry govern the threshold region and up to which energy ?*

3. *Is the Feynman diagram method sufficient for an adequate description or are different concepts like Regge exchange more appropriate to understand associated strangeness production ?*

From the experimetal side, data of sufficient accuracy are needed to answer these questions. As a theoretical side, investigating production of kaon and hyperon in this work, we would like to contribute the way to answer the above two questions.

In this work, we study the muti kaons production to understand strangeness production dynamcis more deeply.

Part II

One Kaon Photoproduction

2

$\gamma\, p \;\rightarrow\; K^{+}\Lambda(1116)$

2.1 Introduction

The production of strange particles in photoproduction at medium energies could give us more deeper insight of the strangeness in the hadron physics. To study this subject, many facilities, like SAPHIR [3] and CLAS have performed several hyperon production experiments.

In this chapter, we review the ground Lambda particle production process, $\gamma p \rightarrow K^{+}\Lambda(116)$. This process is well described with resonance in an effective Lagrangian scheme [13]. In this work, we try to describe the ground Lambda photo-induced production with the gauge invariant set without a resonace since the goal of the review of the one kaon photoproduction is to test several form factors types and to find available parameter values to investigate Ξ and Ω production.

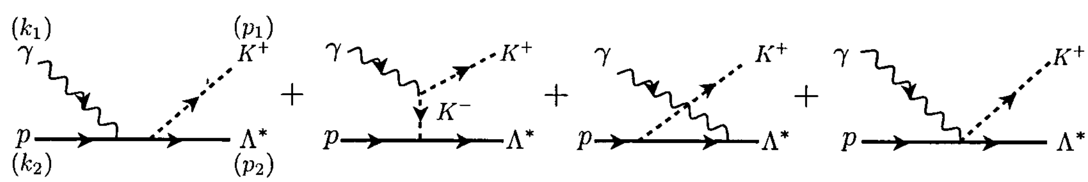

FIG. 2.1: Gauge invariant diagram set of $\gamma p \rightarrow K^{+}\Lambda(116)$

We consider the four gauge invariant diagrams in the FIG. 2.1. We are going to show the formalism we used and next the numerical result step by step.

2.2 Formalism

Effective Lagrangian is given by

$$\mathcal{L}_{\gamma NN} = -e\bar{N}\left[\gamma^\mu - \frac{\kappa_p}{2M_N}\sigma_{\mu\nu}\partial^\nu\right]A^\mu N \tag{2.1}$$

$$\mathcal{L}_{Kp\Lambda} = g_{kp\Lambda}\bar{\Lambda}\gamma^\mu\gamma_5\partial_\mu K^- p \tag{2.2}$$

$$\mathcal{L}_{\gamma KK} = -ie(K^-\partial_\mu K^+ - K^+\partial_\mu K^-)A^\mu \tag{2.3}$$

$$\mathcal{L}_{\gamma\Lambda\Lambda} = e\bar{\Lambda}\left[\frac{\kappa_\Lambda}{2M_\Lambda}\sigma_{\mu\nu}\partial^\nu\right]A^\mu\Lambda \tag{2.4}$$

$$\mathcal{L}_{\gamma Kp\Lambda} = ieg_{\gamma Kp\Lambda}\bar{\Lambda}\gamma^\mu\gamma_5 K^- pA^\mu. \tag{2.5}$$

In our calculation $g_{\gamma Kp\Lambda} = g_{Kp\Lambda}$ and we use the following parameters.

Table 2.1: Parameters in this work

κ_p	1.79	PDG
$g_{Kp\Lambda}$	6.15	SU(3)
κ_Λ	-0.613	PDG

T-matrices for each diagram are given by

$$T_s = ieg_{pK\Lambda}\bar{u}(p_2)\not{p}_1\gamma_5\left[I + \frac{\kappa_p}{2M_p}(\not{k}_1 + \not{k}_2 + m_p)\right]\not{k}_1\not{\epsilon}_\gamma u(k_2)\frac{1}{(k_1+k_2)^2 - m_p^2} \tag{2.6}$$

$$T_t = -ieg_{pK\Lambda}\bar{u}(p_2)(\not{k}_1 - \not{p}_1)\gamma_5 u(k_2)\frac{2p_1\cdot\epsilon_\gamma}{(k_1-p_1)^2 - m_k^2} \tag{2.7}$$

$$T_u = ieg_{pK\Lambda}\frac{\kappa_\Lambda}{2m_\Lambda}\bar{u}(p_2)\not{k}_1\not{\epsilon}_\gamma\frac{\not{k}_2 - \not{p}_1 + m_\Lambda}{(k_2-p_1)^2 - m_\Lambda^2}\not{p}_1\gamma_5 u(k_2) \tag{2.8}$$

$$T_c = -ieg_{pK\Lambda}\bar{u}(p_2)\not{\epsilon}_\gamma\gamma_5 u(k_2) \tag{2.9}$$

T^{inv} and T^{viol} stand for the self gauge invariant part of T and the gauge violating part of T. One can apply type I or type II form facotr to gauge invariant part and some common type form factor to gauge violating part. Surely summation of gauge violating parts satisfies the gauge invariance.

As a next step, we apply the gauge invariant form factors as follows:

$$T = T_s^{\mathrm{inv}} F(s) + (T_s^{\mathrm{viol}} + T_t + T_c) F_c + T_u F(u). \tag{2.10}$$

T_s^{inv} and T_s^{viol} denote the gauge invariant part of T_s and the gauge violating part of T_s respectively. F_c stands for the common form factor and defined by

$$F_c = 1 - (1 - F(s))(1 - F(t))(1 - F(u)). \tag{2.11}$$

We try the three form factor type for each F. Type I form factor is defined by

$$F_M(p^2) = \frac{\Lambda_M^2 - m^2}{\Lambda_M^2 - p^2} \tag{2.12}$$

$$F_B(p^2) = \left[\frac{n\Lambda_M^4}{n\Lambda_M^4 + (p^2 - M^2)}\right]^n \tag{2.13}$$

where F_M and F_B stand for the form factors of the scalar meson and the baryon respetively.

In type II form factor, F_M has same form as F_B :

$$F_M(p^2) = F_B(p^2) = \left[\frac{n\Lambda_M^4}{n\Lambda_M^4 + (p^2 - M^2)}\right]^n. \tag{2.14}$$

As the 3rd form factor, let me introduce type III form factor. This overall form factor is motivated in the rescattering process in ϕ photoproduction in chapter 7 and I check that this kinds of form factor gives us available magnitude of the cross section even in one kaon photoproduction. Type III form factor are applied as follows:

$$T = (T_s + T_t + T_c + T_u) F(s) F(t). \tag{2.15}$$

We use the same form factor in Eq.(2.14) as $F(s)$ and $F(t)$. Since the summation of the four T-matrices are gauge invariant, this scheme doesn't violate the gauge invariance. But we can see this form factor gives us smaller value than type I and type II because two form factor are multiplied. Nevertheless this type III form factor is very sensitive to the cut-off, then we get the reasonable megnitude in a little lager cut-off than cut-offs in other two types.

To test these three type of form factors, I apply these to the energy dependent cross section calculation and we can see the result in the next section.

2.3 Numerical result

2.3.1 Contribution of each channels

Here we show the cross section of each channel. At first, the cross section without form factor is shown in the below.

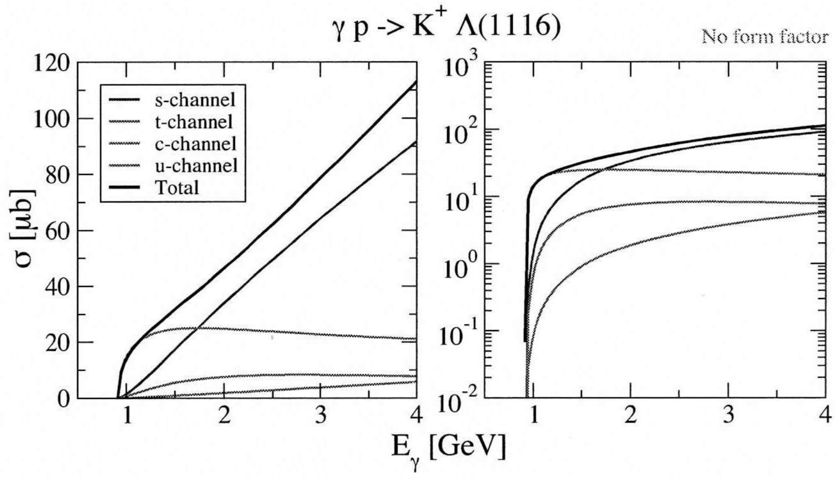

FIG. 2.2: Contributions of each channels with form factor in different scales.

As we see in FIG. 2.2, c-channel contribution is dominant near the threshold but s-channel is dominant as the photon energy increases. In the right pannel, we can distingush the difference of the channels' contribution in the log scale.

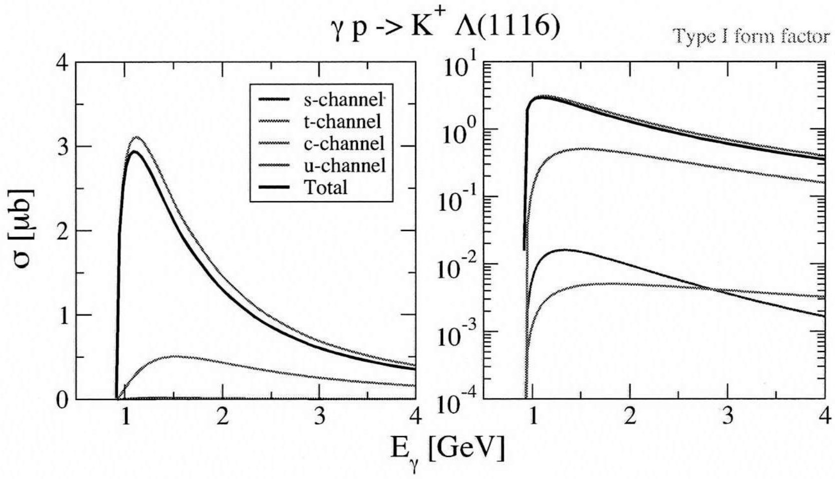

FIG. 2.3: Channels' contribution with form factor. Type I form factor is used with $n = 1$, $\Lambda_M = 0.7$ GeV and Λ_B =0.7 GeV.

With the form factor, c-channel is the most dominant one in thw whole energy region.

2.3.2 Energy dependent cross section

Here the energy dependent cross sections are shown with the three form factors.

Type I form factor

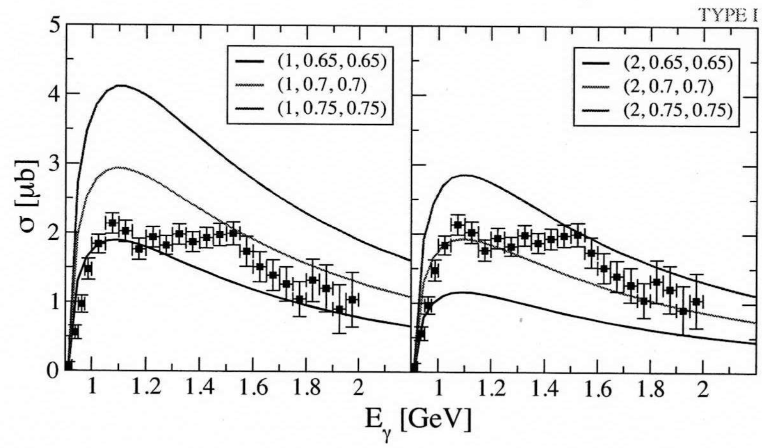

FIG. 2.4: The total cross section with various parameters. Parameters in the legend denote $(n, \Lambda_M, \Lambda_B)$.

We can see that experimental data are well described with cut-off value, around 0.65 GeV. Resonances contribution is well known in $\gamma p \to K^+\Lambda(1116)$ process, but in this chapter we treat the basic gauge invariant set only for simplicity.

Type II form factor

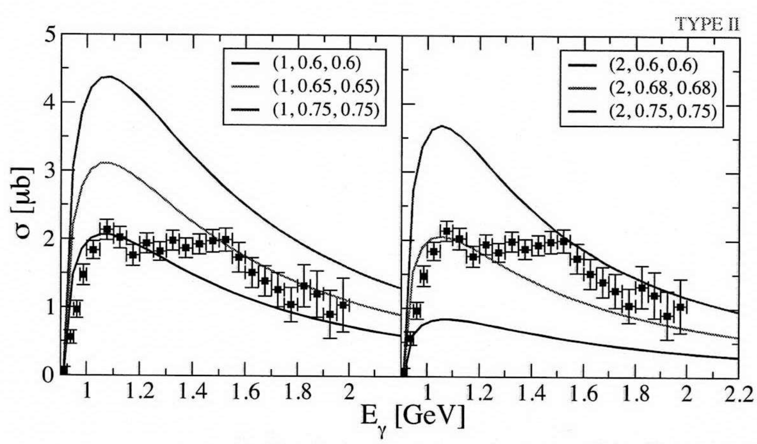

FIG. 2.5: The total cross section as a functon of the photon energy, E_γ with type II form factor. Parameters in the legend denote $(n, \Lambda_M, \Lambda_B)$.

This form factor makes more sharp peak near the threshold region than type I form factor.

Type III form factor

This type III form factor is motivated from the study of ϕ meson photoproduction. We use this kinds of form factor when we describe the rescattering of ϕ meson photoproduction with the $K^+\Lambda(1520)$ intermediate state.

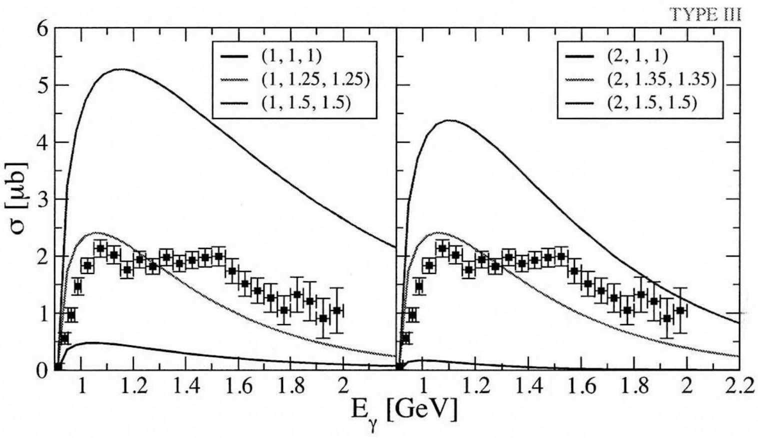

FIG. 2.6: The total cross section as a functon of the photon energy, E_γ with type III form factor. Parameters in the legend denote $(n, \Lambda_M, \Lambda_B)$.

Since two form factors are mutiplied to T-matrix, type III form factor gives us small value but we can see this form factor is really sencitive to cut-off parameter. Such a property makes this form factor give a relevant magnitude in ϕ meson photoproduction, I guess. As a alternative of the form factor in the hadronic process, we would like to test availability of this form factor in the several cases.

2.3.3 Angle dependent differential cross section

Here the differential cross section as a function of the scattering angle at specific energy. We show some plot usging type I form factor with same parameter set which we used in the previous section. We can see that the experimant data can be well described except the threshold energy region, $E_\gamma = 0.925$ GeV. We use only basic four gauge invariant set. Some discrepancy could be explained with some resonaces and t-channel K^* exchange, I guess.

Here we show the differential cross section with type I form factor only. In the case it is need to investigate the form factor dependence of the cross section, we can do that with parameter set described previously. The goal of this section is to check the compatibility of each form factor in some cases. And we want to apply this resut to understand Ξ and Ω production cases.

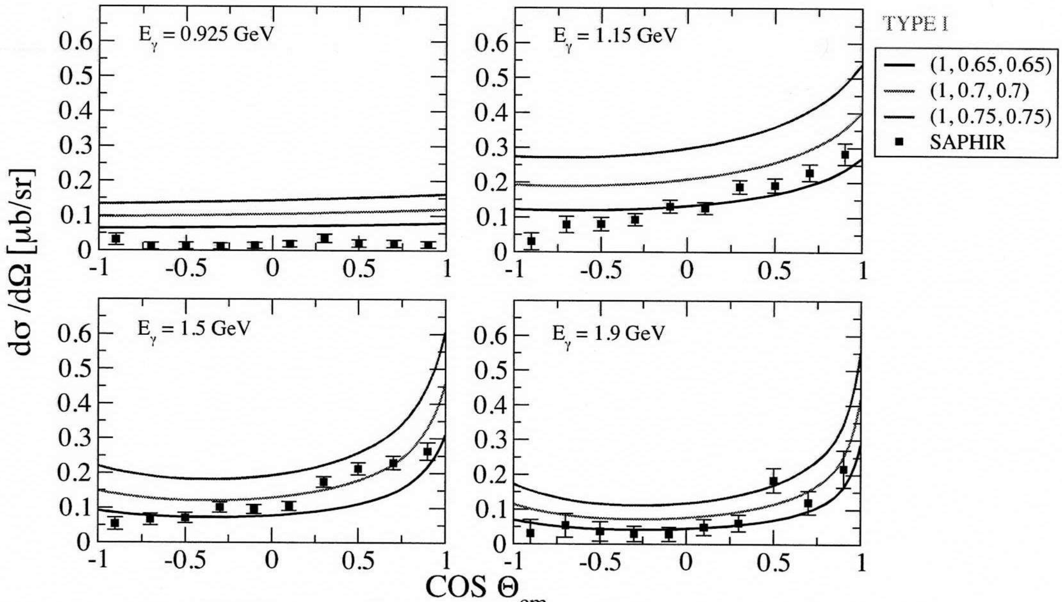

FIG. 2.7: The differential cross section as a functon of $\cos\theta$.

2.3.4 Beam asymmetry

The beam asymmetry shows that there are some polariaztion dependence when we measure the observable in the laboratory. We can measure this using the linearly polarized photon beam.

Here the beam asymmetry as a funciton of E_γ and $\cos\theta_{c.m.}$ are shown. The beam asymmetry which we used here is difined by

$$\Sigma = \frac{d\sigma_\perp/d\Omega - d\sigma_\parallel/d\Omega}{d\sigma_\perp/d\Omega + d\sigma_\parallel/d\Omega}. \tag{2.16}$$

where $d\sigma_\perp/d\Omega$ and $d\sigma_\parallel/d\Omega$ are the differential sections with linearly polarized photon in the perpendicular direction and in the parallel to the reaction plane. Since we choose XZ plane as a reaction plane, the perpendicular direction to the reaction plane is y direction and the parallel direction to the reaction plane is x direction.

In this section we show the energy dependent and scattering angle dependent beam asymmetry. Even though there is no experimental data of the beam asymmetry of $\gamma p \to K^+\Lambda(1116)$ process, it can be a kind of prediction or a guideline for the future work.

First we show the scattering angle dependent beam asymmetry with type I form factor. We describe the beam asymmetry with varing parameters. Using the same form factor and parameters, we show the energy dependent one also.

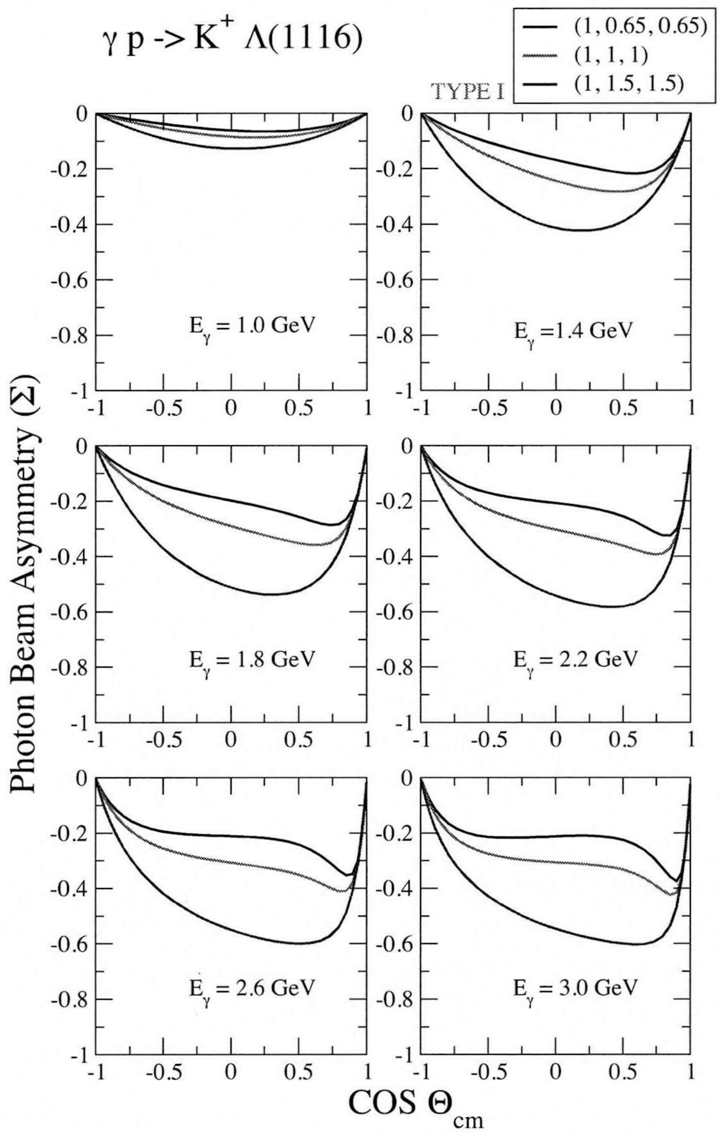

FIG. 2.8: The photon beam asymmetry as a functon of $\cos\theta$.

In FIG. 2.8, we show the beam asymmetry with type I form factor at each scattering angle. Since there are very small difference in the range, 0.65 GeV $< \Lambda < 0.75$ GeV, we try larger cut-off Λ value, 1 GeV and 1.5 GeV which are used in other photoproductions. Next let us consider the energy dependent beam asymmetry.

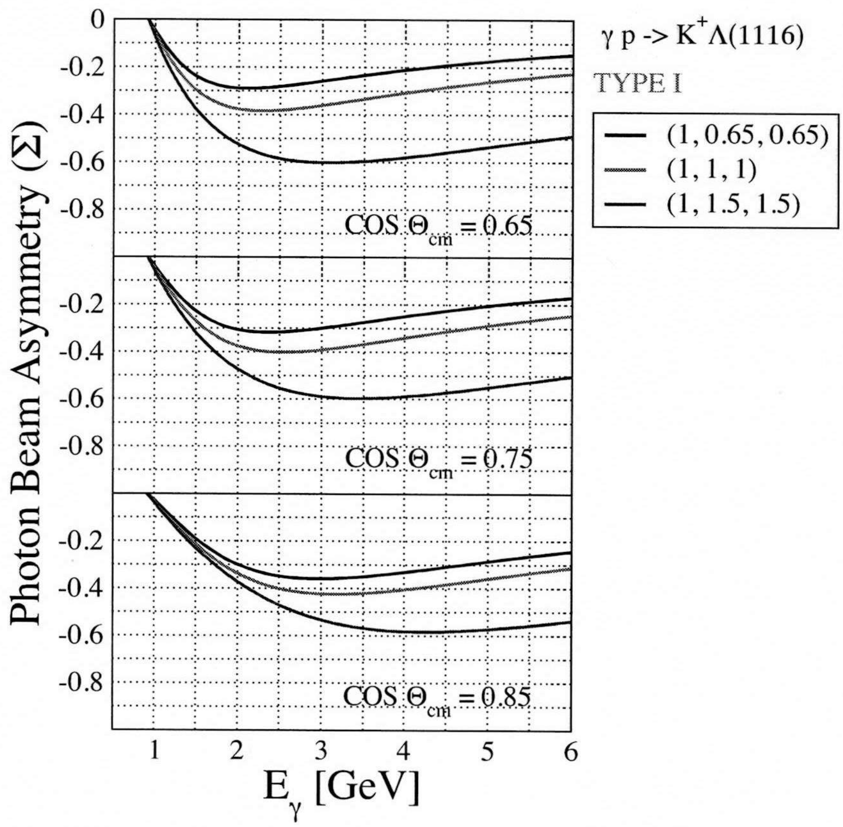

FIG. 2.9: The photon beam asymmetry as a functon of E_γ.

2.4 Summary of this chapter

$\Lambda(1116)$ production is important as the ground state of Λ baryon which occurs in the most kaon production cases. In this point of view, to study $\gamma p \to K^+\Lambda(1116)$ is basic and important.

In this chater, we show that we can successfully describe $\gamma p \to K^+\Lambda(1116)$ scattering process in an effective Lagrangian approach. We test three types of form factors not only for checking the validity of the form factors but also for the mult-kaons production calculation. Futhermore we show beam asymmetry estimations for the future work.

3

$\gamma\, p \;\rightarrow\; K^{+}\Lambda(1405)$

3.1 Introduction

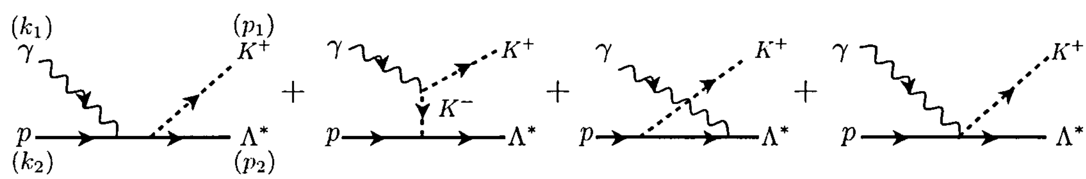

FIG. 3.1: Gauge invariant diagram set of $\gamma p \rightarrow K^+\Lambda(1405)$

The $\Lambda(1405)$ resonace is a negative parity baryon resonacne with spin 1/2, isospin $I = 0$ and strangeness $S = -1$. The resonance is located slightly below the KN threshold and decays into the $\pi\Sigma$ channel through the strong interaction. Theoretically, the existence of $\Lambda(1405)$ was predicted in 1959 by Dalitz and Tuan, based on the analysis of the experimental data of the $\overline{K}N$ scattering length [4, 5]. An experimental evidence of this resonance was reported as early as 1961 in the invariant mass spectrum of the $\pi\Sigma$ channel in the $K^-p \rightarrow \pi\pi\pi\Sigma$ reaction at 1.15 GeV [12]. In recent years, the structure of $\Lambda(1405)$ has been found to be important in various aspects in the strangeness sector of nonperturbative QCD. At the same time, the experimental information on $\Lambda(1405)$ is being rapidly improved by new data, such as the $\pi\Sigma$ mass spectra in several reactions and the precise measurement of the energy level of the kaonic hydrogen. Thus, it is an important and urgent issue to understand the nature of the $\Lambda(1405)$ resonance.

In this chapter, we calculate the cross section and the beam asymmetry as a function of E_γ and $\cos\theta$

by considering four Feynmann diagrams in FIG. 3.1. The parameters determined in this calculation can be considered as $s\bar{s}$ production and would be used to estimate multi-$s\bar{s}$ production processes. We use the form factor set which we used $\gamma p \to K^+\Lambda(1116)$.

3.2 Formalism

Effective Lagrangians are given by

$$\begin{aligned}
\mathcal{L}_{\gamma KK} &= -ie(\partial^\mu K^- K^+ - \partial^\mu K^+ K^-)A_\mu &(3.1)\\
\mathcal{L}_{\gamma NN} &= -e\overline{N}\left[\gamma^\mu - \frac{\kappa_N}{2M_N}\sigma^{\mu\nu}\partial^\nu\right]A_\mu N &(3.2)\\
\mathcal{L}_{N\Lambda^* K} &= g_{N\Lambda^* K}\partial_\mu K^- \Lambda^* \gamma^\mu N &(3.3)\\
\mathcal{L}_{\gamma N\Lambda^* K} &= ieg_{N\Lambda^* K} A_\mu K^- \Lambda^* \gamma^\mu N &(3.4)\\
\mathcal{L}_{\gamma\Lambda^*\Lambda^*} &= e\frac{\kappa_{\Lambda^*}}{2M_{\Lambda^*}}\overline{\Lambda}^* \sigma_{\mu\nu}(\partial^\nu A^\mu)\Lambda^*. &(3.5)
\end{aligned}$$

Here $\Lambda^* = \Lambda(1405)$ and we use the following parameter set.

Table 3.1: Parameters in this work

κ_p	1.79	PDG
$g_{Kp\Lambda^*}$	± 1.9486	flavor singlet assumptions
κ_{Λ^*}	0.25	Skyrme model [11], unitarized ChPT [6]

T-matrices for each channel are given by

$$\begin{aligned}
T_s &= ieg_{p\Lambda^* K}\bar{u}(p_2)\not{p}_1 \frac{\not{k}_1 + \not{k}_2 + M_p}{(k_1+k_2)^2 - M_p^2}\left[1 + \frac{\kappa_p}{2M_p}\not{k}_1\right]\not{\epsilon}_\gamma u(k_2) &(3.6)\\
T_t &= -ieg_{p\Lambda^* K}\bar{u}(p_2)(\not{k}_1 - \not{p}_1)u(k_2)\frac{2(p_1\cdot\epsilon_\gamma)}{(k_1-p_1)^2 - m_k^2} &(3.7)\\
T_u &= -i\frac{2\kappa_{\Lambda^*}}{2M_{\Lambda^*}} g_{p\Lambda^* K}\bar{u}(p_2)\not{k}_1\not{\epsilon}_\gamma \frac{\not{k}_2 - \not{p}_1 + M_{\Lambda^*}}{(k_2-p_1)^2 - M_{\Lambda^*}^2}\not{p}_1 u(k_2) &(3.8)\\
T_c &= ieg_{p\Lambda^* K}\bar{u}(p_2)\not{\epsilon}_\gamma u(k_2) &(3.9)
\end{aligned}$$

We can easily check T_s, T_t and T_c consists of gauge invariant set and T_u is gauge invariant itself.

$$T = T_s^{\rm inv} F(s) + \left(T_s^{\rm viol} + T_t + T_c\right) F_c(s,t,u) + T_u F(u) \tag{3.10}$$

3.3 Numerical result

3.3.1 Contribution of each channel

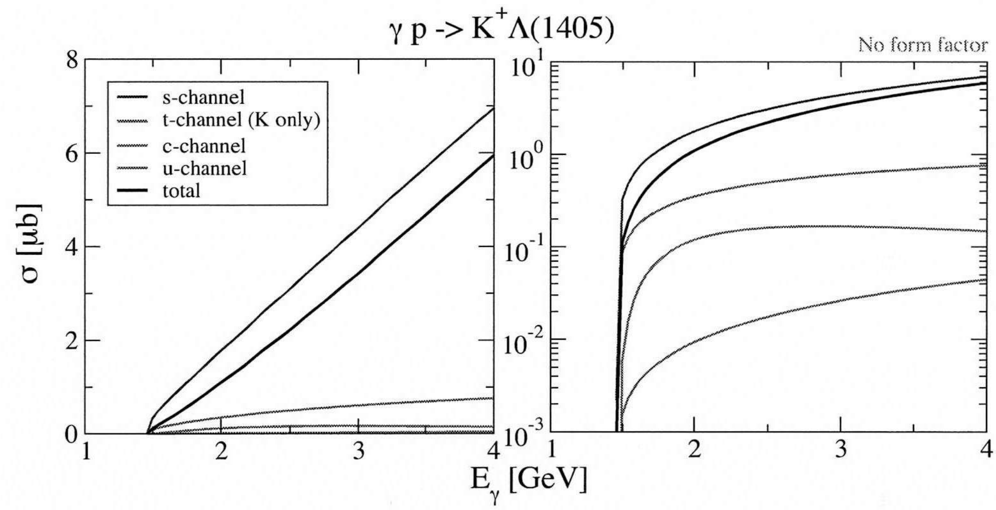

FIG. 3.2: Total cross section without form factor. Two plots are same but in different scale.

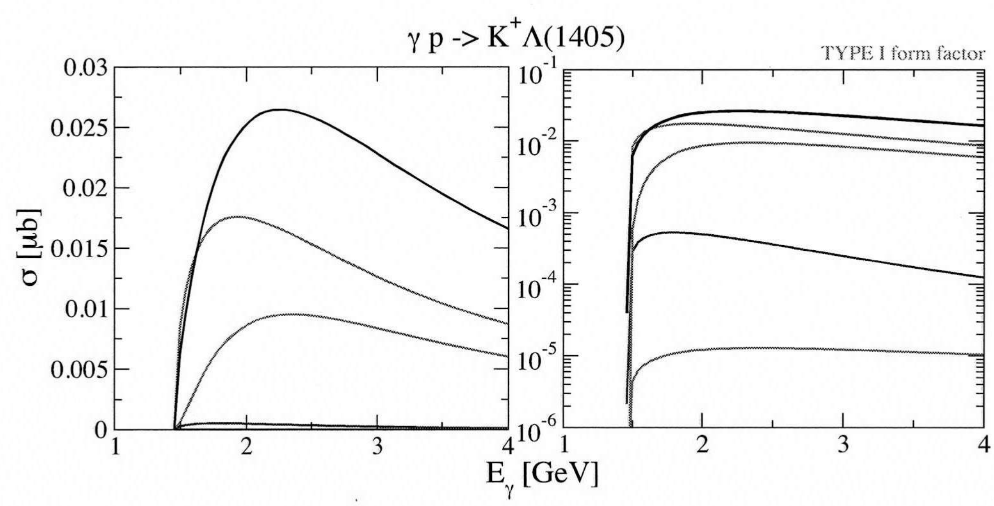

FIG. 3.3: The total cross section with the type I form factor. They are shown in the different scale and each line is denoted in the same way of FIG. 3.2.

FIG. 3.2 tells us that s-channel is dominant and there are negative interference effect between s-channel and others since s-chaanel contribution is larger than the total. The total cross section with the form factor are shown in FIG. 3.3. Here the contribution of c-channel is larger than that of s-channel.

3.3.2 Energy dependence with form factors

The total cross sections with the type I and type II form factor are shown. Usually $\Lambda \simeq 0.7$ GeV value is available to expalin one $s\bar{s}$ production. But here I try several cou-offs which appear in the other photoproduction.

Type I form factor

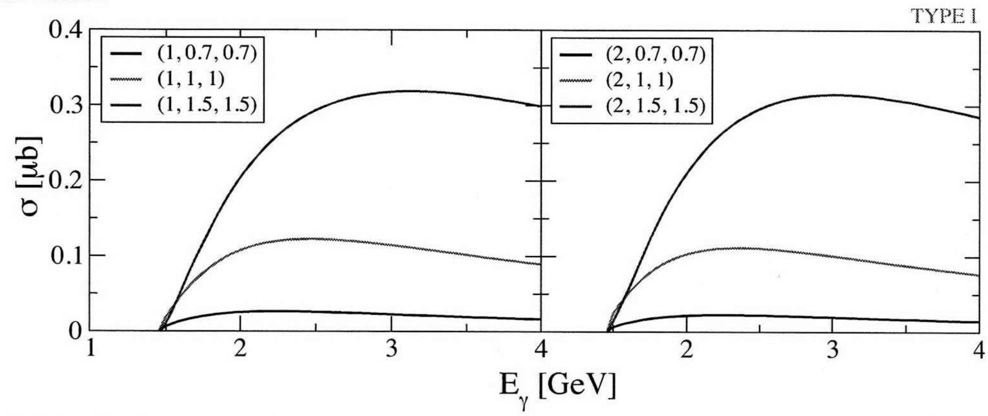

FIG. 3.4: Total cross section without form factor. Two plots are same but in different scale.

Type II form factor

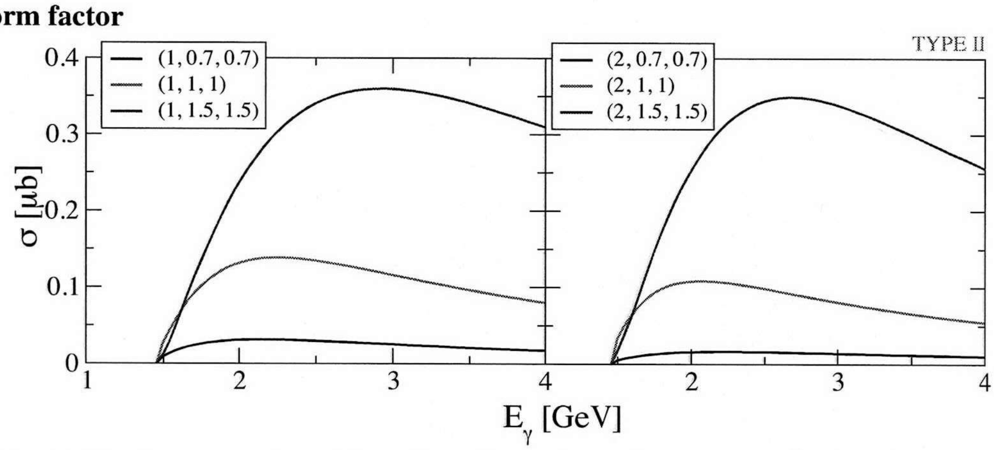

FIG. 3.5: Total cross section without form factor. Two plots are same but in different scale.

3.3.3 Angular dependence with form factors

Here we show with parameter at several E_γ.

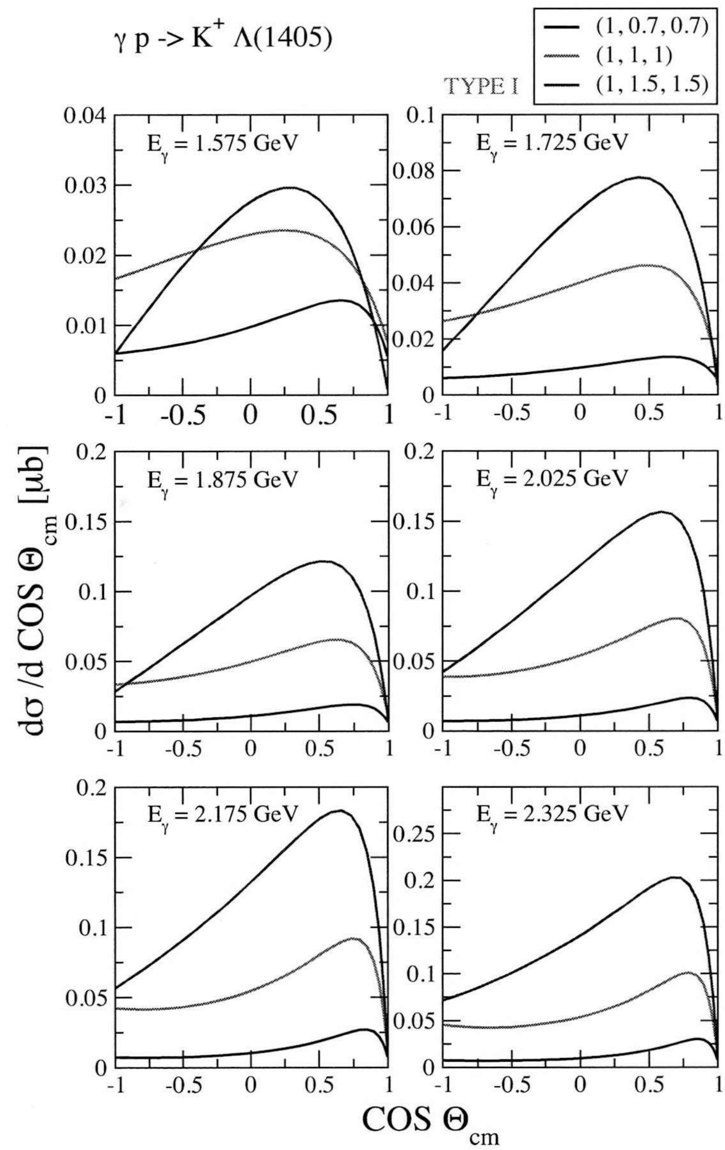

FIG. 3.6: Differential cross section as a function of $\cos\theta_{\rm cm}$.

We can observe that the maximum values increase as E_γ increases. And maximums appear forward, $\cos\theta \sim 0.7$.

3.3.4 Photon beam asymmetry

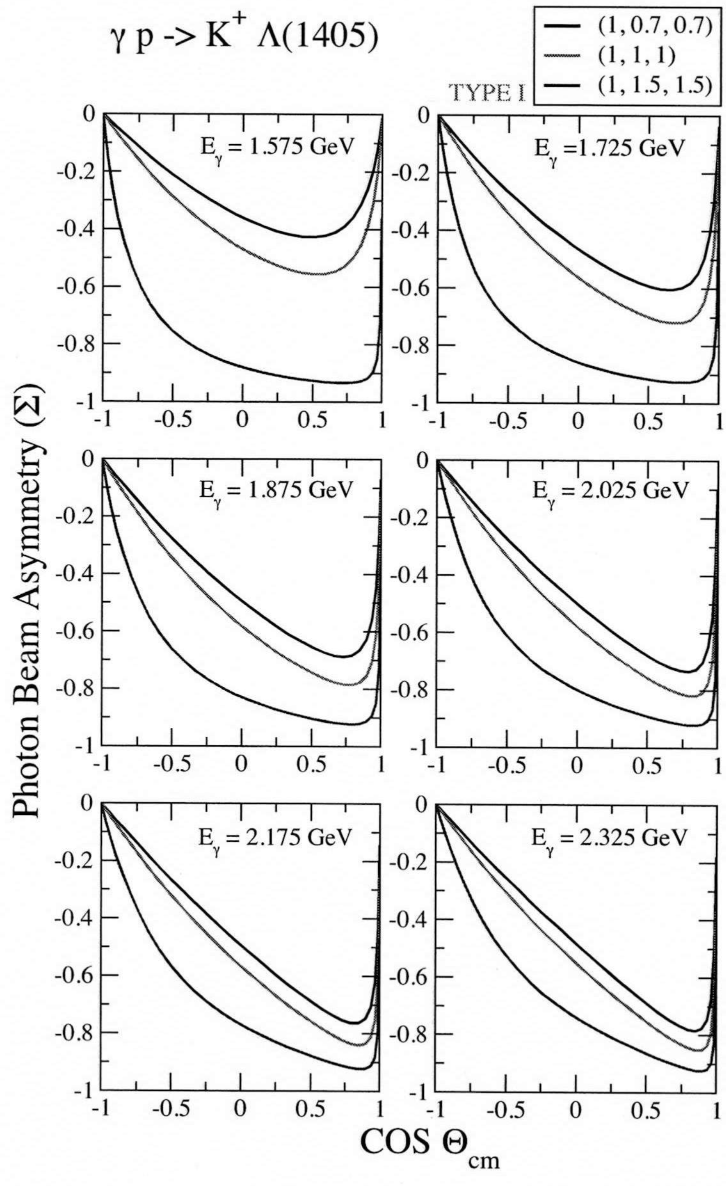

FIG. 3.7: Photon beam asymmetry as a function of $\cos\theta$ with type I form factor.

We use the same definition of the beam asymmetry in Eq.(2.16). We shold be careful the definition and the sign of beam asymmetry. Our result shows that the sign of photon symmetry is negative. It means that the electric photon-hadron coupling is larger than the magnetic one.

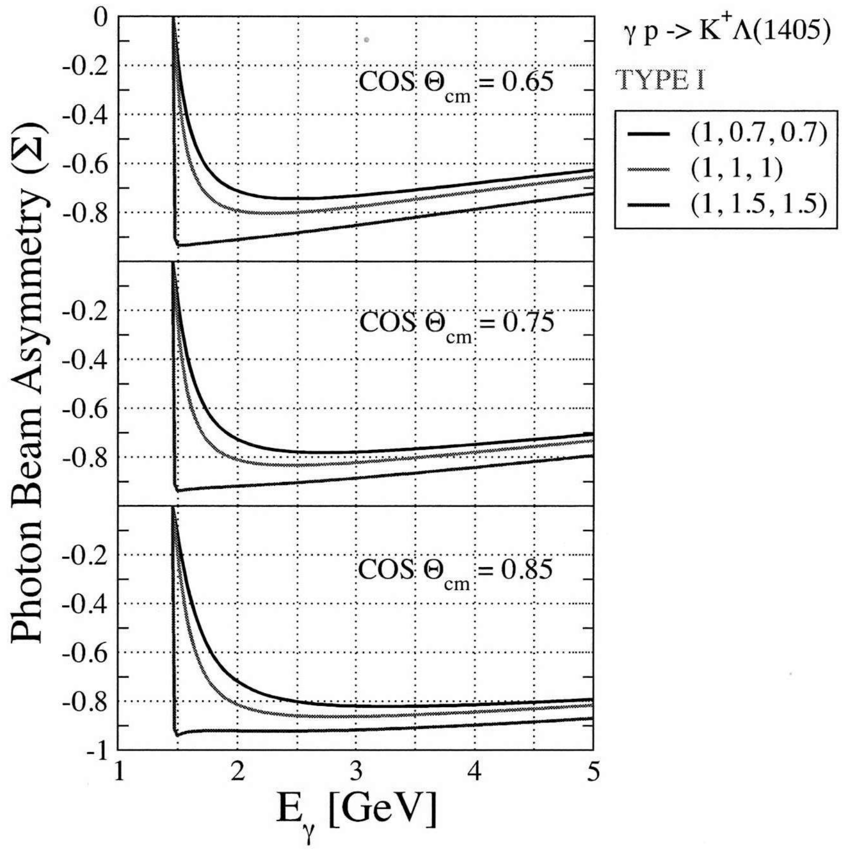

FIG. 3.8: Photon beam asymmetry as a function of the photon energy E_γ with type I form factor.

3.4 Summary of this chapter

$\Lambda(1405)$ resonance baryon is considered as not only 3 quarks state but also strongly bouned $\overline{K}N$ state. We don't still understand this resonance particle well and it means that it is very interesting subject to investigate. In this point of view, to study the $\Lambda(1405)$ resonance baryon is very important to obtain deeper understanding of the strangess in the hadron physics. In this chapter we calculate the cross section and the beam asymmetry as a function of E_γ and $\cos\theta$ in reasonable cut-off range. There are not many clear data of $\gamma p \to K^+\Lambda(1405)$, we extimate observables in an effective Lagrangian approach. Our work in this chapter is not only predictions of the $\Lambda(1405)$ production but also a basic step to understand the muti-kaons production. In the next chapter, we investigate other hyperon resonance, $\Lambda(1520)$.

4

$\gamma\, p \rightarrow K^+\Lambda(1520)$

4.1 Introduction

The $\Lambda(1520)$ baryon resonance has been spotlighted because its mass is similar to that of the expected Θ^+ but strangeness is opposite. As far as the experimental of the $\Lambda(1520)$ production are concerned, there are experiments reported so far: Boyarski *et al* (photoproduction)[7], the Daresbury group (photoproduction) [8] and the CLAS collaboration (electroproduction)[10]. Recently the LEPS collaboration is searching for the Θ^+ associated with the production of the $\Lambda(1520)$ in photoproduction off the deuteron.

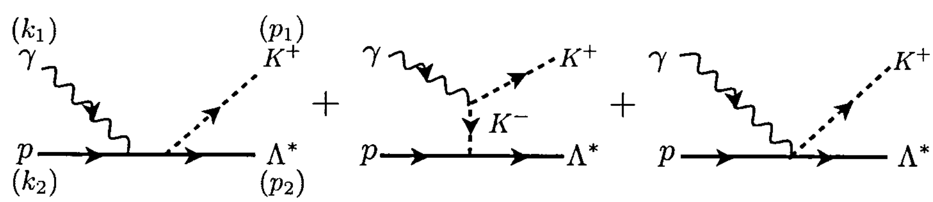

FIG. 4.1: Gauge invariant diagram set of $\gamma p \rightarrow K^+\Lambda(1520)$

In this chapter, we investigate the $\Lambda(1520)$ photoproduction near the threshold energy. We use the same gauge invariant form factor formalism which we apply the $\Lambda(1116)$ and $\Lambda(1405)$ previously. We can use the results of $\gamma p \rightarrow K^+\Lambda(1520)$ to test the effective Lagrangian formalism and to estimate multi-kaons photoproduction. We consider the s, t, c-channel except the u-channel because the magnetic moment of $\Lambda(1520)$ is not known well and the u-channel contribution is supressed in usual $K^+\Lambda$ producton case.

4.2 Formalism

Effective Lagrangian is given by

$$\mathcal{L}_{\gamma NN} = -e\overline{N}\left[\gamma_\mu - \frac{\kappa_N}{2M_N}\sigma_{\mu\nu}\partial^\nu\right]A^\mu N \tag{4.1}$$

$$\mathcal{L}_{\gamma KK} = -ie(\partial^\mu K^- K^+ - \partial^\mu K^+ K^-)A_\mu \tag{4.2}$$

$$\mathcal{L}_{KN\Lambda^*} = \frac{g_{KN\Lambda^*}}{m_K}(\partial^\nu K^-)\overline{\Lambda}_\nu \gamma_5 N \tag{4.3}$$

$$\mathcal{L}_{\gamma KN\Lambda^*} = i\frac{g_{KN\Lambda^*}}{m_K}A^\nu K^- \overline{\Lambda}_\nu \gamma_5 N \tag{4.4}$$

with $|g_{KN\Lambda^*}| = 10.9$. T-matrices are given by

$$T_s = ieg_{KN\Lambda^*}\bar{u}^\alpha(p_2)p_{1\alpha}\gamma_5\frac{k_1 + \not{k}_2 + M_p}{(k_1+k_2)^2 - M_p^2}\left[1 + \frac{\kappa_p}{2M_p}\not{k}_1\right]\not{\epsilon}_\gamma u(p_1) \tag{4.5}$$

$$T_t = -ieg_{KN\Lambda^*}\bar{u}^\alpha(p_2)(k_1 - p_1)_\alpha\gamma_5 u(p_1)\frac{2p_1\cdot\epsilon_\gamma}{(k_1-p_1)^2 - m_K^2} \tag{4.6}$$

$$T_c = -ieg_{KN\Lambda^*}\bar{u}^\alpha(p_2)\gamma_5 u(p_1)\epsilon_{\gamma\alpha} \tag{4.7}$$

We apply the form factor which preserves the gauge invariance as follows:

$$T = T_s^{\text{inv}}F(s) + (T_s^{\text{viol}} + T_t + T_c)F_c \tag{4.8}$$

where $F_c = 1 - (1 - F(s))(1 - F(t))$. s and t are defined $s = (k_1 + k_2)^2 = (p_1 + p + 2)^2$ and $t = (k_1 - p_2)^2 = (k_2 - p_2)^2$ respectively. T_s^{inv} denotes the self-gauge invariant part of T_s and T_s^{viol} is gauge violating part of T_s. Since sumation of T_s^{viol}, T_t and T_c preserve the gauge invariance, form factors in Eq.(4.8) don't violate the gauge invariance of T. As we discussed in the previous chapters, we try two form factor type for F_s and F_t with various parameters. We employ the Rarita-Schwinger field for spin-3/2 particles and they are defined in Appendix A.

At first, we would like to check the contribution of each channel without the form facotr and with form facotr. After that we will discuss about the energy and angular dependent cross section and beam asymmetry. Through this prosedure, we can find avaible value or range of cut-off in the form factor with experimental data. We will use these parameter values to extimate the multi-kaons photoproductions later.

4.3 Numerical result

4.3.1 Channel contritution

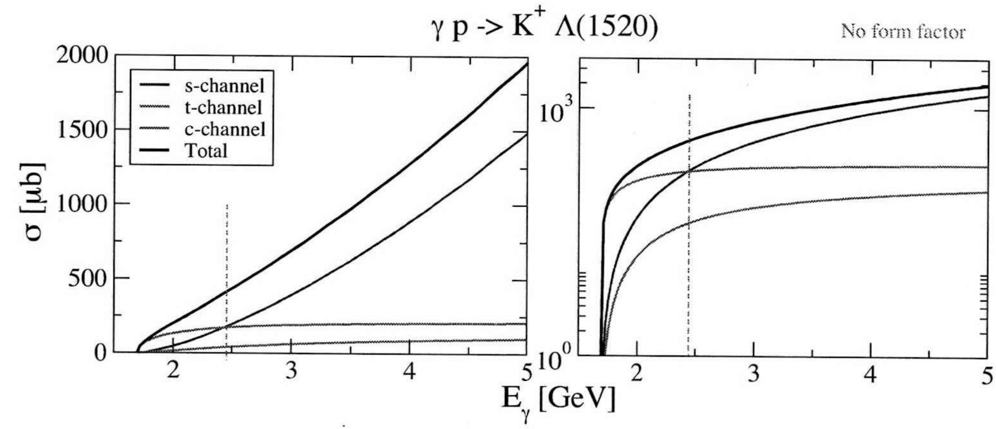

FIG. 4.2: Total cross section as a function the photon energy E_γ without form factor.

Near the threshold, c-channel contribution is dominant. But in large photon energy region, s-channel contribution is larger than c-channel.

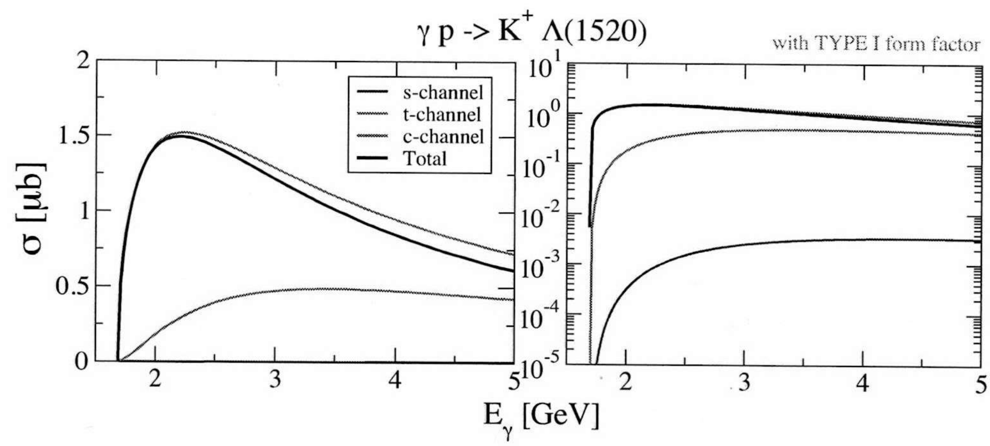

FIG. 4.3: Total cross section as a function the photon energy E_γ with type I form factor. Two plots describe same graph. The left is ploted in a linear scale and the left is ploted int log scale. Parameters of form factor are choosen as $(n, \Lambda_M, \Lambda_B) = (1,\ 0.75,\ 0.75)$.

FIG. 4.3 shows form facotrs make s-channel depressed very much. Form factors are really important not only to fit the experimental data but also to determine each channel's contribution. Next section we will test form factors with several parameters when we describe the cross section and beam asymmetry.

4.3.2 Energy dependence

Type I form factor

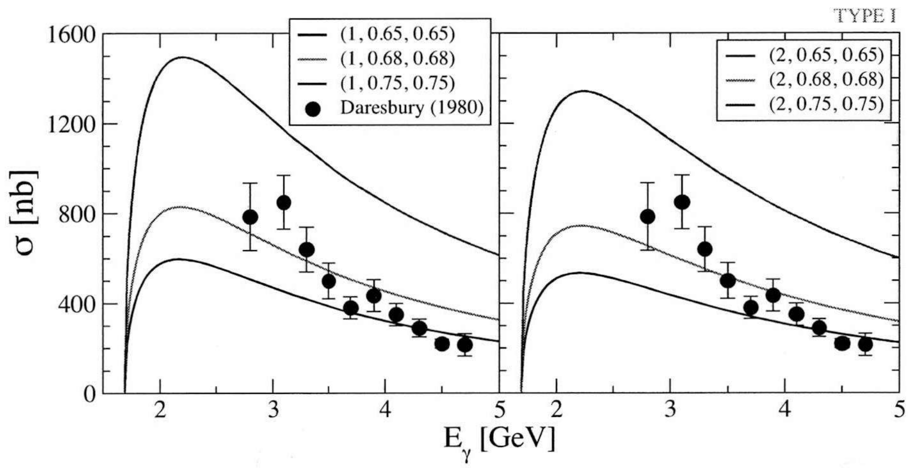

FIG. 4.4: Total cross section with the type I form factor.

$\Lambda_M = \Lambda_B = 0.68$ GeV is the best fit (the green line) and other cut-offs are tried also (black and blue line).

Type II form factor

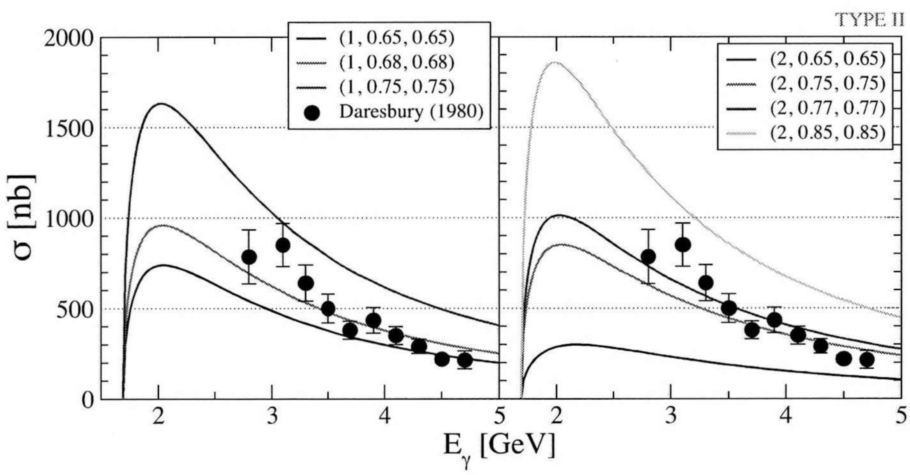

FIG. 4.5: Total cross section with the tyep II form factor.

The experimental data are well described with type II form factor with the same cut-off range of type I form factor.

4.3.3 Angle dependence

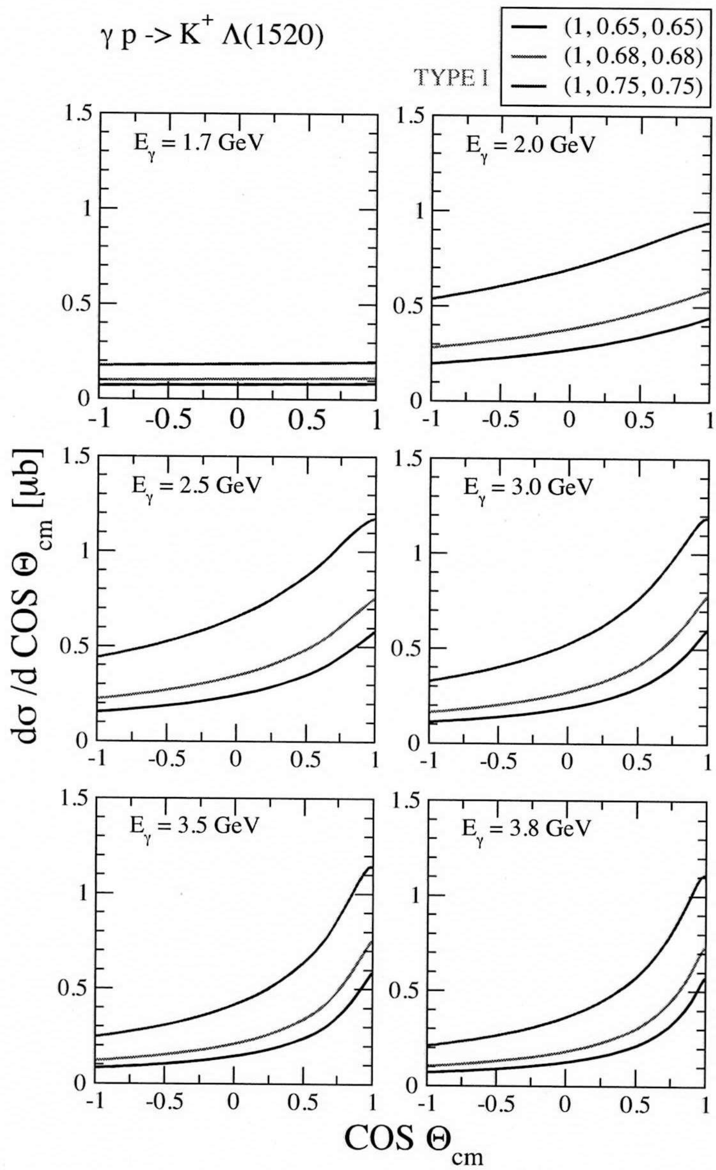

FIG. 4.6: Total cross section with the type I form factor.

The differential cross sections at several photon energies are shown in the FIG. 4.6. We observe that there is almost no angle dependence near the threshold. It looks reasonable that there are no so many $\Lambda(1520)$ baryon production near threshold. The cross section increase when the scattering angle goes to the forward.

4.3.4 Beam asymmetry

We use the definition of the beam asymmetry in Eq. (2.16).

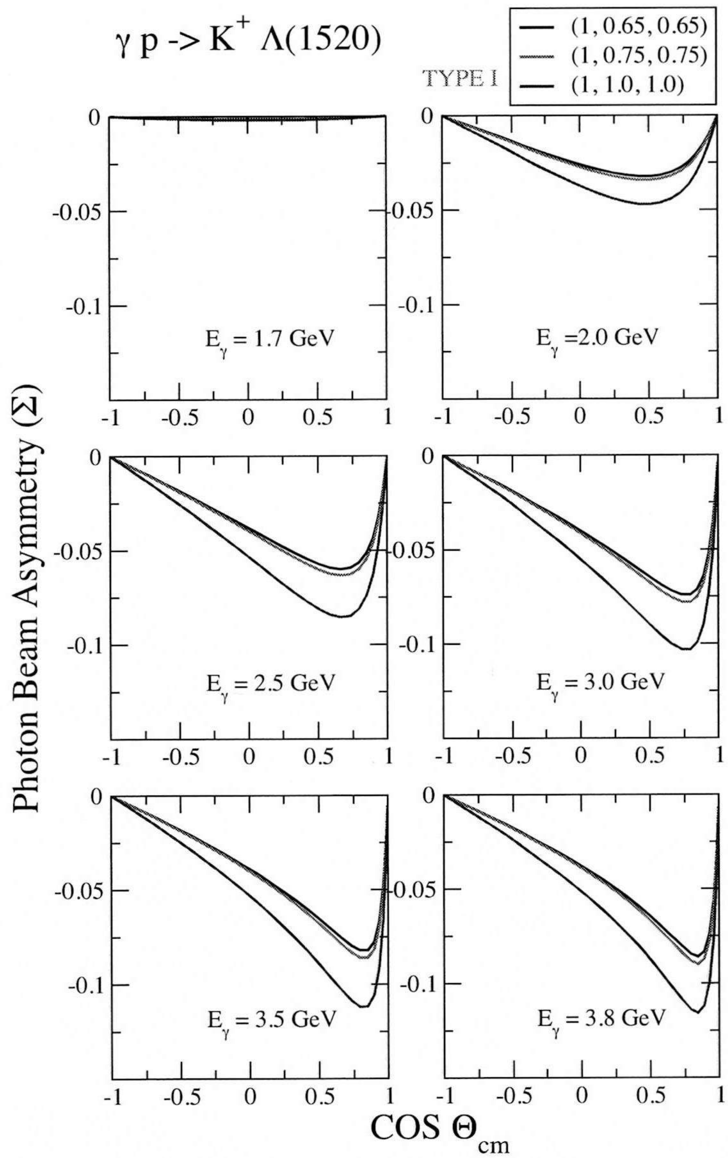

FIG. 4.7: The beam asymmetry as a function of $\cos\theta_{c.m.}$ with the type I form factor.

It is difficult to distingush the difference between the parellel and the perpendicular components of the photon beam near the threshold (the upper left pannel). The maximum magnitude increase as the photon energy increases and the beam asymmetries are zero at the forward and backward angles. FIG. 4.7 tells us that the beam asymmetry is larger near the forward angle region than the backward angle region.

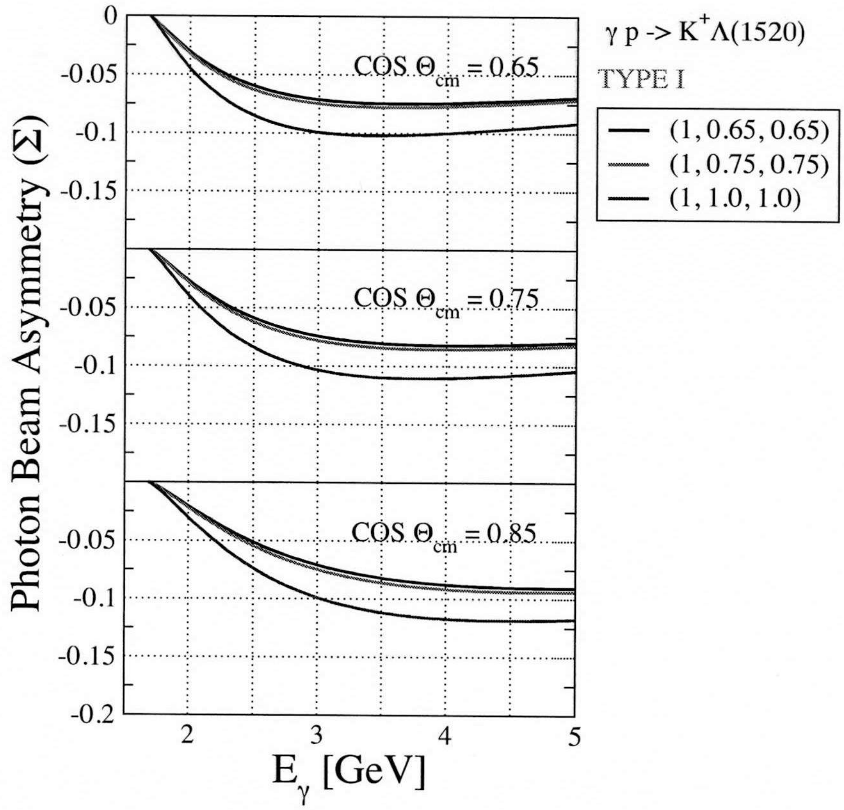

FIG. 4.8: The beam asymmetry as a function of E_γ with the type I form factor.

FIG. 4.8 shows the energy dependence of the beam asymmetry near the backward region. Since there is no experimental data, these result are prediction.

4.4 Summary and outlook

Strangeness photoproduction is an important to obtain a deeper understanding of the nature of baryon resonances. Up to now, some nucleon resonances have been observed at the near-threshold energy in the KY photoproduction. Investigating $K\Lambda^*$ state is a good waty to study poorly understood nucleon resonacnes with a heavy mass since the threshold of $K\Lambda^*$ is relatively high compared with that for the πN, ηN and $K\Lambda$ photoproduction. In the present work, we describe the $K^+\Lambda(1520)$ photoproduction with an effective Lagrangian method. We would like to extend this fromalism to the multi-kaons photoproduction.

Another interesting point is a bump structure of the differential cross section of $\gamma p \to K^+\Lambda(1520)$ [9]. We would like to reproduce this bump with the coupled-channel method. There are still many curioud area in $K\Lambda^*$ photoduction.

Part III

Two Kaons Photoproduction

5

ϕ photoproduction: Introduction and Tree level calculation

5.1 Introduction

$\phi(1020)$ photoproduction has been an interesting subject because of characteristic property of ϕ meson. The $\phi(1020)$ meson is distinguished from other vector mesons, since it contains mainly strange quarks. Because of its dominant strange quark content, its decays to lighter mesons and coupling to the nucleon are known to be suppressed by the Okubo-Zweig-Iizuka (OZI) rule. In fact, the strange vector form factors of the nucleon, which is implicitly related to the ϕ meson via the vector-meson dominance, is reported to be rather small [18]. This large $s\bar{s}$ content of the ϕ meson makes the meson-exchange picture unfavorable in describing photoproduction of the ϕ meson. Thus, the Pomeron [19, 20] is believed to be the main contribution to ϕ photoproduction, since it explains the slow rise of the differential cross sections of ϕ photoproduction as the energy increases. However, while it is true in the higher energy region, a recent measurement reported by the LEPS collaboration [21] shows a bump-like structure around the photon energy $E_\gamma \approx 2.3$ GeV. It seems that the Pomeron alone cannot account for this bump-like structure and requires that one should consider other production mechanism of ϕ photoproduction near the threshold energy. Moreover, a recent measurement of the spin-density matrix elements near the threshold region [22] implies that hadronic degrees of freedom play essential role in the vicinity of the threshold.

So far, the theoretical understanding of the production mechanism for the ϕ photoproduction can be summarized as follows:

- General energy-dependence of the cross sections is mainly explained by Pomeron exchange that can be taken as either a scalar meson or a vector meson with charge conjugation $C = +1$. While the Pomeron explains the increase of the differential cross section $d\sigma/dt$ in the forward direction, it cannot describe the behavior of $d\sigma/dt$ near the threshold.

- The exchange of neutral pseudoscalar mesons (π^0, η) provides a certain contribution to $d\sigma/dt$ near the threshold but it is not enough to explain the threshold behavior of $d\sigma/dt$ [23]. Moreover, π^0 and η exchanges cannot explain the spin-density observables and, in particular, ρ^1_{1-1} matrix element (see Appendix for its definition).

- Usual vector meson-exchanges such as ρ and ω are forbidden due to their negative charge conjugations ($C = -1$). Otherwise, the charge conjugation symmetry will be broken.

- Vector meson-exchanges with exotic quantum number such as $I(J^{PC}) = 1(1^{-+})$ are allowed but those vector mesons are not much known experimentally. Moreover, as for the experimental data from the deuteron target, exchange of isoscalar mesons is more plausible. On the other hand, there is no experimental evidence for isoscalar hybrid-exotic mesons [24].

- The contribution of scalar mesons such as σ and f_0 are negligibly small for $d\sigma/dt$ [23].

Understanding this present theoretical and experimental situation in ϕ photoproduction, Ozaki et al. [25] proposed a coupled-channel method based on the K-matrix formalism. They considered the $\gamma N \to K\Lambda^*(1520)$ and $K\Lambda^* \to \phi N$ kernels [26] in the coupled-channel formalism in addition to $\gamma N \to \phi N$ and $\phi N \to \phi N$. It is a very plausible idea; since the threshold energy for the $K\Lambda^*$ is quite close to that for the bump-like structure ($E_\gamma \approx 2.3$ GeV), the $\Lambda^*(1520)$ resonance may influence ϕ photoproduction. Moreover, the $\gamma p \to K\Lambda^*(1520)$ reaction can be regarded as a subreaction for the $\gamma p \to K\overline{K}p$ process together with the $\gamma p \to \phi p$ one in Ref. [26]. In addition, a possible nucleon resonance ($J^P = 1/2^-$) with large $s\bar{s}$ content was also taken into account. Interestingly, the coupled-channel effects were shown to be not enough to explain the bump-like structure $E_\gamma \approx 2.3$ GeV. On the other hand, the bump-like structure was described by their possible N^* and was interpreted as a destructive interference arising from the N^* resonance [40, 41].

Table 5.1 shows the previous important work relevant to the present work. Before 1999, people have tried to understand $\phi(1020)$ photoproduction with Pomeron prescripton. In 2005 LEPS collaboration found there is a bump like structure near the threshold. Many people have tried to understand this threshold behavior via Pomeron, scalar particle exchange mechnism and resonances.

Table 5.1: Timeline of ϕ photoproduction research

Author	Date	What they did	Ref.
Titov *et al*	1999	Structure of the ϕ photoproduction at a few GeV	[23]
T. Mibe *et al*	2005	Near-Threshold Diffractive ϕ-Meson Photoproduction from the proton	[21]
S. Ozki *et al*	2009	Coupled-channel analysis for ϕ photoproduction with $\Lambda(1520)$	[25]
W. C. Chang *et al*	2010	Measurement of spin-density matrix elements for ϕ-meson photoproduction from protons and deuterons near threshold	[22]
A. Kiswandhi *et al*	2010	Is the nonmonotonic behavior in the cross section of ϕ photoproduction near threshold a signature of a resonance ?	[41]
H. Y. Ryu *et al*	2012	ϕ photoproduction with couple-channel effects	[76]

Recently LEPS measured the spin density matrix at backwark region to investigate ϕ photoproduction nature deeply. In the present work, we show that we can explain the bump-like structure near the threshold and density matrix using not only conventional method but also hadronic rescattering process.

5.2 Pomeron exchange amplitudes

Kinematics is given by

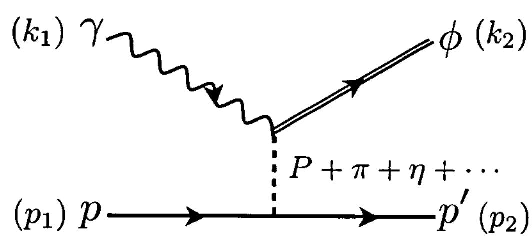

FIG. 5.1: Kinematics of tree level diagram

Incoming photon momentum and ougoing phi meson momentum are denoted by k_1 and k_2 respectively, and incoming proton momentum and outgoing proton momentum are by p_1 and p_2 as shown in Fig(5.1). P stands for pomeron and π, η and σ are other exchanged particles. The amplitude of the Pomeron-exchange [29, 30, 31] is given by

$$\mathcal{M} = -\bar{u}(p_2)\mathcal{M}_{\mu\nu}u(p_1)\epsilon_\phi^{*\mu}\epsilon_\gamma^\nu, \tag{5.1}$$

where ϵ_ϕ and ϵ_γ are the polarization vectors of the ϕ meson and photon. $\mathcal{M}_{\mu\nu}$ is

$$\mathcal{M}^{\mu\nu} = M(s,t)\Gamma^{\mu\nu}, \tag{5.2}$$

where the transition operator $\Gamma^{\mu\nu}$ is defined as

$$\begin{aligned}\Gamma^{\mu\nu} &= \not{k}_\gamma\left(g^{\mu\nu} - \frac{k_2^\mu k_2^\nu}{k_2^2}\right) - \gamma^\nu\left(k_\gamma^\mu - k_2^\mu\frac{k_1\cdot k_2}{k_2^2}\right)\\ &\quad -\left(k_2^\nu - \bar{p}^\nu\frac{k_\gamma\cdot k_2}{\bar{p}\cdot k_1}\right)\left(\gamma^\mu - \frac{\not{k}_2 k_2^\mu}{k_2^2}\right),\end{aligned} \tag{5.3}$$

with $\bar{p} = (p_1 + p_2)/2$. Note that the Pomeron amplitude preserves gauge invariance $k_1^\nu\mathcal{M}_{\mu\nu} = 0$. The corresponding invariant amplitude $M(s,t)$ in Eq.(5.2) is written as [25]

$$M(s,t) = C_pF_N(t)F_\phi(t)\frac{1}{s}\left(\frac{s-s_{\rm th}}{4}\right)^{\alpha_P(t)}\exp\left(-\frac{i\pi}{2}\alpha_P(t)\right), \tag{5.4}$$

where $s = (k_1+p_1)^2$ and $t = (k_1-k_2)^2$. $F_N(t)$ is the isoscalar form factor of the nucleon, whereas $F_\phi(t)$ is the form factor for the photon-ϕ meson-Pomeron vertex. They are parameterized, respectively, as

$$\begin{aligned}F_N(t) &= \frac{4M_N^2 - a_N^2 t}{(4M_N^2 - t)(1-t/t_0)^2},\\ F_\phi(t) &= \frac{2\mu_0^2}{(1-t/M_\phi^2)(2\mu_0^2 + M_\phi^2 - t)}.\end{aligned} \tag{5.5}$$

The Pomeron trajectory $\alpha_p(p) = 1.08 + 0.25\,t$ in Eq.(5.4) is determined from hadron elastic scattering in the high-energy region. The prefactor C_p in Eq.(5.4) governs the overall strength of the amplitude and $s_{\rm th}$ determines the starting energy at which the Pomeron-exchange comes into play. We will discuss the determination of these two parameters later.

5.3 π and η exchange amplitude

To calculate pseudoscalar meson ($\varphi = \pi^0,\ \eta$) exchange in the t channel, we introduce the following effective Lagrangians:

$$\begin{aligned}
\mathcal{L}_{\phi\gamma\varphi} &= \frac{e}{m_\phi} g_{\phi\gamma\varphi}\epsilon^{\mu\nu\alpha\beta}\partial_\mu\phi_\nu\partial_\alpha A_\beta\varphi\,, \\
\mathcal{L}_{\varphi NN} &= \frac{g_{\varphi NN}}{2M_N}\bar{N}\gamma_\mu\gamma_5 N\partial^\mu\varphi,
\end{aligned} \tag{5.6}$$

where ϕ_ν, A_β, and N denote the ϕ vector meson, photon, and nucleon fields, respectively, m_ϕ and M_N stand for the masses of the ϕ meson and nucleon, respectively, and e represents the electric charge. The t-channel amplitude then takes the following form:

$$\mathcal{M} = \frac{eg_{\varphi NN}g_{\phi\gamma\varphi}}{m_\phi}\frac{iF_{\varphi NN}(t)F_{\phi\gamma\varphi}}{t-M_\varphi^2}\bar{u}(p_2)(\not{k}_1-\not{k}_2)\gamma_5 u(p_1)\epsilon^{\mu\nu\alpha\beta}k_{2\mu}\epsilon^*_{\phi\nu}k_{1\alpha}\epsilon_{\gamma\beta}, \tag{5.7}$$

where r is the four momentum of an exchanged pseudoscalar meson. We introduce the monopole-type form factors for each vertex $F_{\varphi NN}(t)$ and $F_{\phi\gamma\varphi}$ defined as

$$F_{\varphi NN}(t) = \frac{\Lambda^2_{\varphi NN}-M^2_\varphi}{\Lambda^2_{\varphi NN}-t}, \quad F_{\phi\gamma\varphi}(t) = \frac{\Lambda^2_{\phi\gamma\varphi}-M^2_\varphi}{\Lambda^2_{\phi\gamma\varphi}-t}. \tag{5.8}$$

As for the coupling constants for the ϕNN, we follow Ref. [23]: $g_{\pi NN} = 13.26$, $g_{\eta NN} = 3.527$ for the πNN and ηNN coupling constants, respectively. We use $\Lambda_{\pi NN} = 0.7\,\text{GeV}$ and $\Lambda_{\eta NN} = 1\,\text{GeV}$ for the cut-off masses of the corresponding form factors. Though these values are different from the phenomenological nucleon-nucleon potentials [32, 33], the effects of the φ-meson exchanges on ϕ photoproduction are rather small. Thus, we will take the values given above typically used in ϕ photoproduction. Those of the coupling constants for the $\phi\gamma\varphi$ vertices are determined by using the radiative decays of the ϕ meson to π and η. Using the data from the Particle Data Group (PDG) [24], one can find $g_{\phi\gamma\pi} = -0.141$ amd $g_{\phi\gamma\eta} = -0.707$. The negative signs of these coupling constants were determined by the phase conventions in SU(3) symmetry as well as by π photoproduction [23]. We choose the cut-off masses for the $\phi\gamma\pi$ and $\phi\gamma\eta$ form factors as follows: $\Lambda_{\phi\gamma\pi} = 0.77$ GeV and $\Lambda_{\phi\gamma\eta} = 0.9$ GeV, respectively.

5.4 Numerical result

FIG. 5.2 shows the differential cross section at the forward angle $d\sigma/dt$ ($\theta = 0$) with various contribution of Pomeron, π meson and η meson shown separately. The parameter set for Pomeron is taken from [25]. We

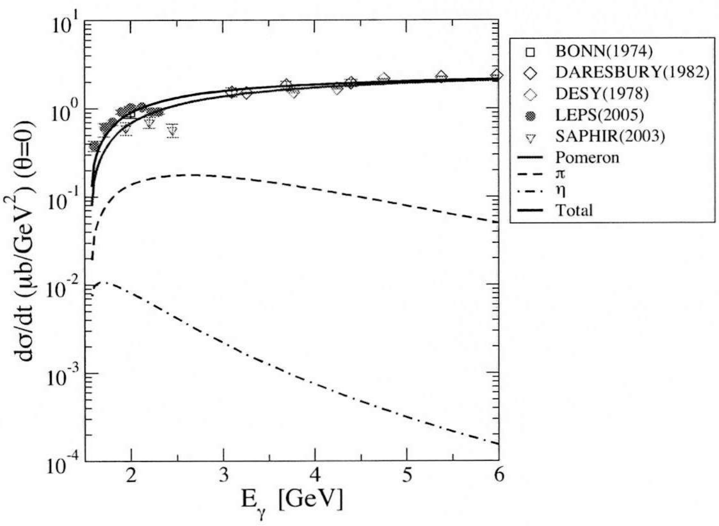

FIG. 5.2: The differential cross section as a function of the E_γ.

see that the total contribution describes the monotonically increasing behavior but the bump structure near the threshold energy is not produced. Also the contribution of the hadronic processes, π and η exchange, are not important. These are the reasion why we try to find other hadronic process to explain the threshold behavior. We are going to explain that part in chapter 7.

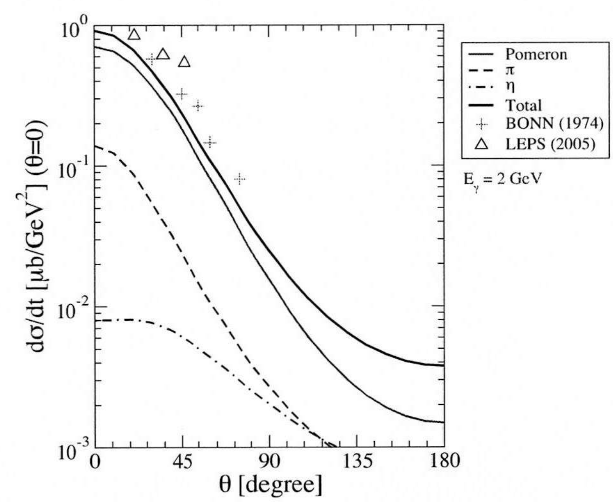

FIG. 5.3: The differential cross section as a function of the angle between photon momentum and ϕ meson momentum in C.M. system.

FIG. 5.3 shows the angular dependence of $d\sigma/dt$ at $E_\gamma = 2$ GeV. The diffractive behavior with the forward peak is well decribed through t-channel Pomeron, π and η exchange.

6

ϕ photoproduction: vector meson exchange contribution

6.1 Introduction

In the begining of ϕ photoproduction, we tested several one meson exchange model to explain the experimental data. After we review π^0, η and σ exchange mechanism, we also investigated the effect of vector mesons exchange. Vector meson exchange model can be one candidate which causes the ϕ photoproduction since Pomeron is expected $J^P = 1^{-1}$ or $J^P = 0^1$.

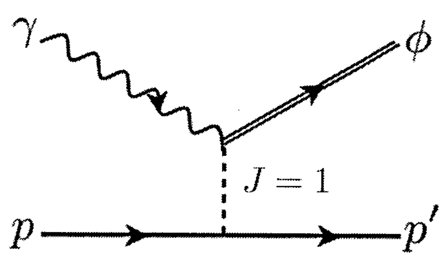

FIG. 6.1: Vector meson ($J = 1$) exchange process

As a simple case, we applyed $\omega(782)$ exchange model to see what happens when the vector meson is considered. Interestingly vector meson exchang model gives us the raising behavior as Pomeron does. Furthermore we can reproduce the angular distribution of the differential data using $\omega(782)$ exchange model.

But the negative charge conjugation tells us that $\omega(782)$ exchange process is forbidden. It makes us to find other vector meson exchange case and as a next trial, we tested $\pi_1(1400)$.

$\pi_1(1400)$ has the lightest exotic vector meson with $J^{PC} = 1^{1+}$. $\pi_1(1400)$ exchange model also gives us the raising behavior when we treat coupling constants of each vertex as free parameters. For more realistic consideration we calculated coupling constants with loops calculations. In the end, we found that our result is much smaller than what we expected as free parameters.

6.2 Vector meson exchange mechanism

Here we would like to shortly review what effect a vector meson exchange model produce. First of all, I will introduce Lagrangian and invariant amplitude. After that I will discuss the numerical results.

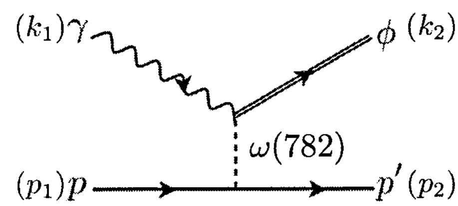

FIG. 6.2: $\omega(782)$ exchange process.

We use the following Lagrangians:

$$\mathcal{L}_{\gamma\phi\omega} = eg_{\gamma\phi\omega}(\partial_\mu A_\nu - \partial_\nu A_\mu)\phi^\mu\omega^\nu \tag{6.1}$$

$$\mathcal{L}_{\omega NN} = g_{\omega NN}\overline{N}\gamma_\mu N\omega^\mu \tag{6.2}$$

where $g_{\omega NN}$[1] and $g_{\gamma\phi\omega}$ are free parameters in our calculation. From the above Lagrangian, we obtain the following invariant amplitudes:

$$\begin{aligned}\mathcal{M} &= ieg_{\gamma\omega}g_{\omega NN}\frac{1}{t-m_\omega^2}\bar{u}(p_2)\Big[(k_1\cdot\epsilon_\phi^*)\not{\epsilon}_\gamma - (\epsilon_\gamma\cdot\epsilon_\phi^*)\not{k}_1 - \frac{q}{m_\omega^2}(k_1\cdot\epsilon_\phi^*)(\epsilon_\gamma\cdot q) \\ &\quad + \frac{\not{q}}{m_\omega^2}(k_1\cdot q)(\epsilon_\gamma\cdot\epsilon_\phi^*)\Big]u(p_1)\times\left\{\frac{\Lambda_{\omega\gamma\phi}^2 - m^2}{\Lambda_{\omega\gamma\phi}^2 - t}\right\}\left\{\frac{\Lambda_{\omega NN}^2 - m^2}{\Lambda_{\omega NN}^2 - t}\right\}\end{aligned} \tag{6.3}$$

where k_1 and k_2 are the photon momentum and ϕ momentum respectively. $q = k_1 - k_2$ and $t = q^2$. Using the this formalism, we calculated the differential cross section as a funcion of the C.M. energy and the scattering angle.

[1] $g_{\omega NN} = 10.3557$ in [2].

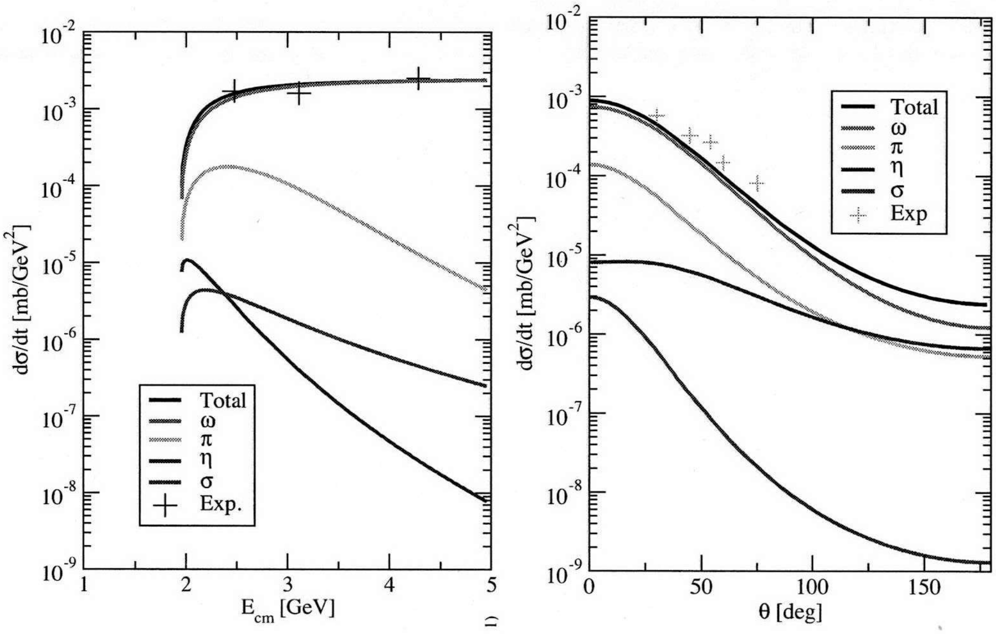

FIG. 6.3: From the left, the differential cross section as a function of the center of mass energy $E_{\rm cm}$ at forward angle ($\theta = 0$) and a function of the scattering angle θ at $E_\gamma = 2$ GeV. $g = 15.8533$, $g_{\omega\phi\gamma} = 1.9045$, $\Lambda_{\omega NN} = 1$ GeV and $\Lambda_{\omega\gamma\phi} = 0.9$ GeV are used.

FIG. 6.3 shows that ω exchange can mimik what Pomeron does. Detailed analysis tells us that such a characteristic behavior comes from the term $\bar{u}(p_2)\not{k}_1 u(p_1)$ in the invariant amplitude of Eq. (6.3). Interesting point is that the same term is in Pomeron amplitude also as shown in Eq (6.4).

$$\begin{aligned}\mathcal{M}_{\rm Pomeron} &= \bar{u}(p_2)\Big[\not{k}_1\Big(g^{\mu\nu} - \frac{k_2^\mu k_2^\nu}{k_2^2}\Big) - \gamma^\nu\Big(k_1^\mu - k_2^\mu\frac{k_1\cdot k_2}{k_2^2}\Big) \\ &\quad -\Big(k_2^\nu - \frac{\bar{p}(k_1\cdot k_2)}{\bar{p}\cdot k_1}\Big)\Big(\gamma^\mu - \frac{\not{k}_2 k_2^\mu}{k_2^2}\Big)\Big] u(p_1)\epsilon_\phi^{*\mu}\epsilon_\gamma^\nu F(s,t) \qquad (6.4)\end{aligned}$$

Simple analysis shows that the propagator of a vecotor meson makes $\bar{u}(p_2)\not{k}_1 u(p_1)$. It is very important message because we may need vector meson-like particle exchange model to obtain the raising behavior as the energy increases within the frame of the effective Lagrangian method. From this finding we can see that which diagram is crucial in the invariant amplidude level.

So far everything seems all right. However, if we consider charge conjugation symmetry, this process is forbidden because of breaking of the symmetry for the ordinary vector meson of $J^{PC} = 1^{--}$. This is the motivation of study of the exotic meson exchange model. As a lightest exotic particle with $J^{PC} = 1^{-+}$, we investigate $\pi_1(1400)$ exchange mechanism.

6.3 $\pi_1(1400)$ exchange mechanism

$\pi_1(1400)$ is the lightest particle which pereserves the charge conjugation in the photoproduction. Since the structures of vertexes are same as the those of ω, we can easily guess that $\pi_1(1400)$ exchange process gives us similar increasing behavior.

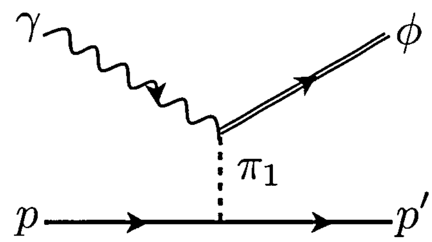

FIG. 6.4: $\pi_1(1400)$ meson exchange process

In this section we intoduce the effective Lagrangian and invariant amplitudes described by π_1 exchange model. After that, we discuss the numerical results.

Effective Lagrangians are given by

$$\mathcal{L}_{\gamma\pi_1\phi} = eg_{\gamma\pi_1\phi}(\partial_\mu A_\nu - \partial_\nu A_\mu)\phi^\mu\pi_1^\nu \tag{6.5}$$

$$\mathcal{L}_{\pi_1 NN} = g_{\pi_1 NN}\overline{N}\gamma_\mu N\pi_1^\mu \tag{6.6}$$

$g_{\gamma\pi_1\phi}$ and $g_{\pi_1 NN}$ are input parameters. In this work multiplication of two coupling constants is parameter. The invariant amplitude is given by

$$\begin{aligned}\mathcal{M} = {} & i\frac{eg_{\gamma\phi\pi_1}g_{\pi_1 NN}}{q^2 - m_{\pi_1}^2}\bar{u}(p_2)\Big[(k_1\cdot\epsilon_\phi^*)\not{\epsilon}_\gamma - (\epsilon_\gamma\cdot\epsilon_\phi^*)\not{k}_1 - \frac{\not{q}}{m_{\pi_1}^2}(k_1\cdot\epsilon_\phi^*)(\epsilon_\gamma\cdot q) \\ & + \frac{\not{q}}{m_{\pi_1}^2}(k_1\cdot q)(\epsilon_\gamma\cdot\epsilon_\phi^*)\Big]u(p_1)\end{aligned} \tag{6.7}$$

where $q\ (= k_1 - k_2)$ is the momentum of π_1. For simplicity, we define g_{π_1} as follows:

$$g_{\pi_1} = g_{\gamma\phi\pi_1}g_{\pi_1 NN}. \tag{6.8}$$

Our reuslt is shown in FIG. 6.5 and our best choice is $g_{\pi_1} \simeq 13$.

Although there are still some ambiguities about the t-channel exchanged particle in ϕ photoproduction, there are some data which supports that the exchanged particle has the natural parity. $\pi_1(1400)$ has the natural parity since $P = (-1)^{-1}$. Therefore the next step is to check whether π_1 exchange process is realistic or not. To do that we calculate the coupling constants by using the known decay modes.

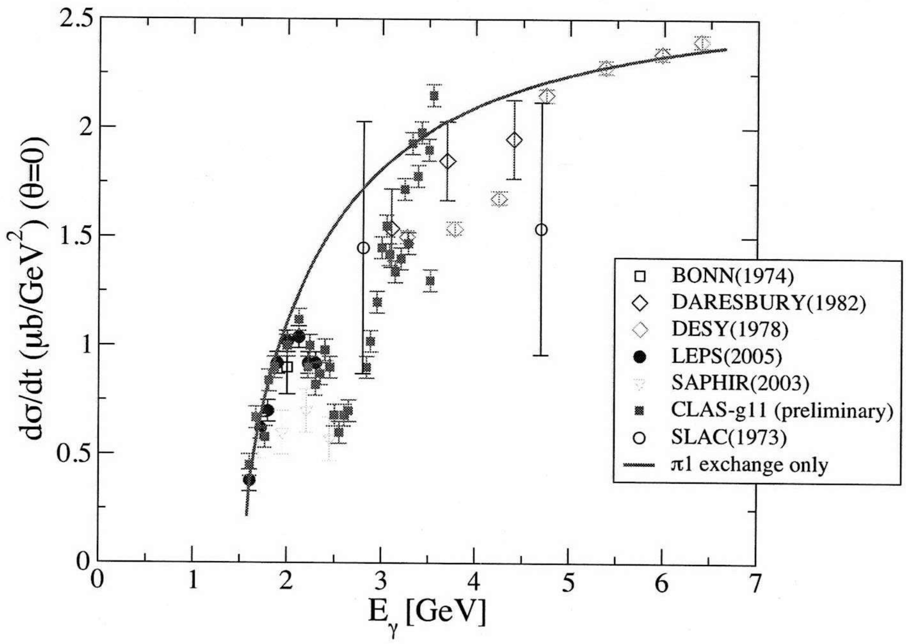

FIG. 6.5: Differential cross section with $\pi_1(1400)$ exchange calculation

6.4 Microscopic structure of $\pi_1(1400)$ vertexes

FIG. 6.6 shows the diagrams which we consider to calculate the coupling constant of $\pi_1(1400)$ vertexes. Triangle type loop are constructed from three decay modes. Let me explain $\gamma - \pi_! - \phi$ vertex part firstly.

6.4.1 $\gamma\pi_1\phi$ vertex

To calculate $g_{\gamma\pi_1\phi}$ we use the following Lagrangian:

$$\mathcal{L}_{\phi\rho\pi^0} = \frac{g_{\phi\rho\pi^0}}{m_\phi}\epsilon^{\mu\nu\alpha\beta}\partial_\mu\phi_\nu\partial_\alpha\rho_\beta\pi^0 \tag{6.9}$$

$$\mathcal{L}_{\pi_1\eta\pi^0} = g_{\pi_1\eta\pi^0}\pi_1^\mu(\partial_\mu\pi^0\eta - \partial_\mu\eta\pi^0) \tag{6.10}$$

$$\mathcal{L}_{\gamma\rho\eta} = \frac{eg_{\gamma\rho\eta}}{m_\rho}\epsilon^{\mu\nu\alpha\beta}\partial_\mu A_\nu\partial_\alpha\rho_\beta\eta. \tag{6.11}$$

Our strategy is that the invariant amplitude of $\pi_1\phi$ vertex is same as that of the above triangle loop vertex. Then we obtain the divergent integration and we need a regulariztion to calculate the integration. $g_{\gamma\pi_1\phi}$ is given by

$$g_{\gamma\pi_1\phi} = -\frac{g_{\phi\rho\pi}g_{\pi\pi_1\eta}}{m_\phi m_\eta}\epsilon^{\mu\nu\alpha\beta}\epsilon^{\mu'\nu'\alpha'\beta'}\int\frac{d^4\ell}{(2\pi)^4}\frac{\left(-g^{\beta\beta'}+\frac{\ell^\beta\ell^{\beta'}}{m_\rho^2}\right)}{\ell^2-m_\rho^2}$$
$$\times\frac{(p-k-2\ell)\cdot\epsilon^*_{\pi_1}\epsilon^\nu_\phi}{(p-\ell)^2-m_\pi^2}\times\frac{p_\mu\ell_\alpha\ell_{\alpha'}k_{\mu'}k_{\nu'}}{(k-\ell)^2-m_\eta^2} \quad (6.12)$$

$$\simeq \frac{m_{\pi_1}^2}{m_\rho m_\phi}\frac{g_{\phi\rho\pi_1}g_{\pi_0\eta\pi_1}}{2(4\pi)^2}\int dx\, dy\log\left(\frac{\Lambda^2+\Delta}{\Delta}\right). \quad (6.13)$$

We took only leading contribution of Λ and $\Delta = (1-x)m_\eta^2 + y^2m_\phi^2 - y(m_\phi^2 - m_\pi^2 + m_\eta^2)$. ℓ is momentum of ρ meson.

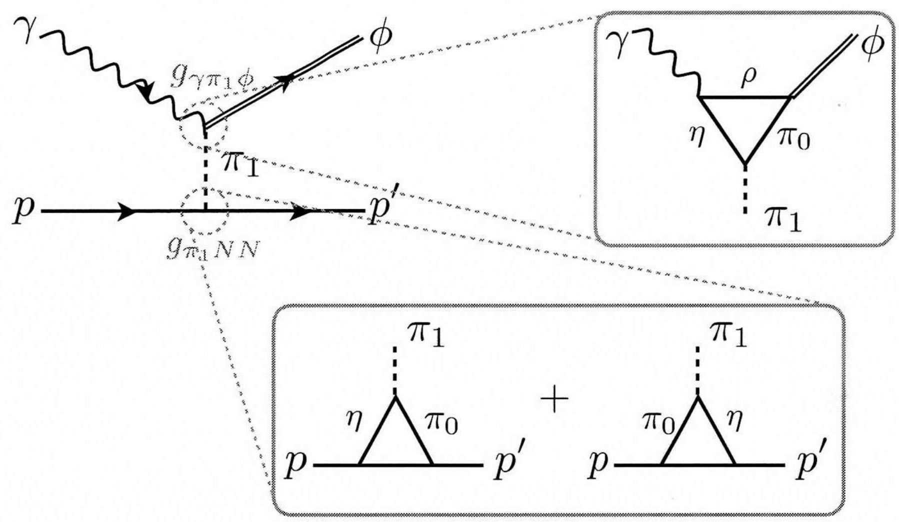

FIG. 6.6: Microscopic structure of $\pi_1(1400)$ vertexes.

Similarly we can calculate the coupling constant for π_1NN vertex. For π_1NN vertex calculation, we use the following Lagrangian

$$\mathcal{L}_{\pi^0NN} = \frac{g_{\pi^0NN}}{2M_N}\overline{N}\gamma_\mu\gamma_5N\partial^\mu\pi^0 \quad (6.14)$$

$$\mathcal{L}_{\eta NN} = \frac{g_{\eta NN}}{2M_N}\overline{N}\gamma_\mu\gamma_5N\partial^\mu\eta \quad (6.15)$$

$$\mathcal{L}_{\pi_1\pi^0\eta} = g_{\pi_1\pi^0\eta}\pi_1^\mu(\partial_\mu\pi^0\eta - \partial_\mu\eta\pi^0) \quad (6.16)$$

We can calculate two loop diagrams related to $\pi_1 NN$ vertex by using the above Lagrangian. Calculating the invariant amplitudes give us the following result:

$$g_{\pi_1 NN} = \frac{g_{\pi_0 NN} g_{\eta NN} g_{\pi_0 \eta \pi_1}}{4m_p^2} \frac{\Lambda^2}{2(4\pi)^2}. \tag{6.17}$$

We used the following coupling constant set:

Table 6.1: parameters in this calculation

$g_{\phi\rho\pi_0}$	2
$g_{\gamma\eta\rho}$	1.23
$g_{\pi_0\pi_1\eta}$	8
$g_{\pi NN}$	13.5
$g_{\eta NN}$	6

Eq. (6.13) and Eq. (6.17) tells us that coupling constants, $g_{\gamma\pi_1\phi}$ and $g_{\pi_1 NN}$ are function of the cutoff Λ. When we choose a little large cutoff, $\Lambda = 1.1$ GeV, we obtain

$$g_{\gamma\pi_1\phi} g_{\pi_1 NN} \simeq 0.02 \tag{6.18}$$

This result is just 0.15% of parameter value ($\sim$ 13) in the tree level calculation.

6.5 Summary and conclusion

To find a alternative of Pomeron which explain the cross section of ϕ meson photoproduction in the high energy region, we have investigated vector meson exchange mechanism.

Although we found that ω exchange model could mimk the Pomeron exchange modelt, this mechanism violate the charge conjugation symmetry. After that we try the simplest exotic particle $\pi_1(1400)$. $\pi_1(1400)$ exchange process can explain monotonically increasing behavior of the total cross section, but their coupling constants are not known. To estimate the magnitude of the cross section of $\pi_1(1400)$ exchange process, we calculate coupling constants in microscopic picture. Using the decay modes in PDG, we can calculate the maximum value of coupling constants of each vertex of loop diagrams. The result shows that the possibility of such a process is very small.

Even though it is not so successful to find the other alternative process instead of Pomeron exchange, we found that vector-like exotic particles could be one chance to investigate the behavior in high energy region. We can try the other exotic particles heavier than $\pi_1(1400)$.

7

ϕ photoproduction: hadronic rescattering contribution

7.1 Introduction

In the present work, we want to scrutinize in detail the nontrivial hadronic contributions arising from hadronic box diagrams in addition to Pomeron and pseudoscalar meson exchanges. Extending the idea of Ref. [25], we consider seven possible box diagrams with intermdiate ρN, ωN, σN, πN, $K\Lambda(1116)$, $K^*\Lambda(1116)$, and $K\Lambda(1520)$ states. However, it is quite complicated to compute these box diagrams explicitly, so that we use the Landau-Cutkosky rule [27, 28], which yields the imaginary part of the box diagrams by its discontinuity across the branch cut. Though their real part may contribute to the transition amplitude, we will show that the imaginary part already illuminates the coupled-channel effects on the production mechanism of $\gamma p \to \phi p$ near the threshold. The parameters such as the coupling constants and cut-off masses of the form factors will be fixed by describing the corresponding processes and by using experimental and empirical data. Yet unknown parameters are varied as compared to the present experimental data. In addition, we tune the strength of the Pomeron amplitude near the threshold region, where the hadronic contribution seems more significant. It is a legitimate procedure, since the Pomeron gets more important as the energy increases. Thus, we determine the threshold parameter in such a way that the Pomeron exchange becomes effective in the higher energy region. We did not consider any N^* resonance, since we do not have much information on them above the ϕN threshold [24]. We will show that the coupled-channel effects are indeed essential in explaining the recent LEPS data, which is the different conclusion from Ref. [25].

The present thesis is organized as follows. In Section II, we explain the basic formalism. We show how to compute the box diagrams mentioned above. In Section III, we present the numerical results such as the energy dependence of the forward cross sections, the angular distributions, and the spin observables. We also discuss how the $K\Lambda^*(1520)$ channel can explain the bump-like structure together with the Pomeron exchange tuned. We discuss in detail the spin-density matrix elements for ϕ-photoproduction. The final Section is devoted to summary and outlook. In the Appendix, we present the definition of the spin-density matrix elements for reference.

7.2 Formalism

We will employ the effective Lagrangians to compute hadronic rescattering process in addition to the Pomeron-exchange. In Fig. 7.1, we draw the relevant Feynman diagrams. The first diagram corresponds

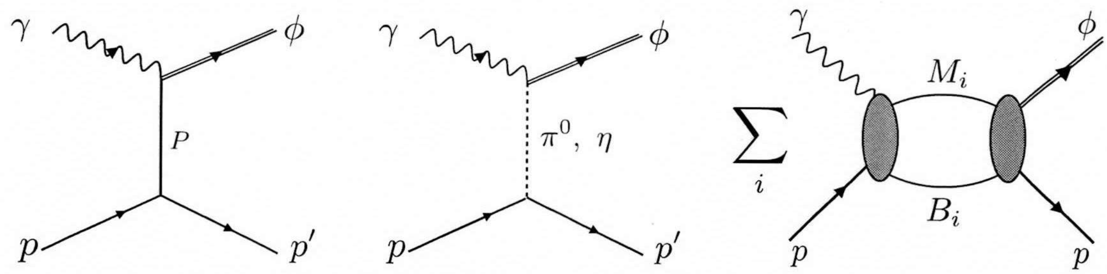

FIG. 7.1: Relevant Feynman diagrams for ϕ photoproduction: We draw, from the left, the diffractive Pomeron exchange, the pseudoscalar meson-exchanges, and the generic box diagram for hadronic rescattering that includes intermediate meson M_i and baryon B_i states.

to the Pomeron-exchange, and the second one depicts π^0- and η-exchanges. The last diagram represents generically all the contributions from various box diagrams with intermediate hadron states, i.e. ρN, ωN, σN, πN, $K\Lambda(1116)$, $K^*\Lambda(1116)$, and $K\Lambda(1520)$, among which the last one was already considered in Ref. [25]. From now on, we will simply define the ρN box diagram as that with intermediate ρ and N states, and so on. We also define the 4-momenta of the incoming photon, outgoing ϕ, the initial (target) proton and the final (recoil) proton as k_1 and k_2, p_1 and p_2, respectively. In the center of mass (CM) frame, these variables are written as $k_1 = (k, k)$, $k_2 = (E_\phi, p)$, $p_1 = (E_p, -k)$ and $p_2 = (E_{p'}, -p)$, where $k = |k|$, $E_\phi = \sqrt{m_\phi^2 + |p|^2}$, $E_p = \sqrt{m_p^2 + |k|^2}$, and $E_{p'} = \sqrt{m_{p'}^2 + |p|^2}$, respectively.

7.2.1 $K^+\Lambda(1520)$ box diagram

In addition to the Pomeron- and pseudoscalar meson-exchanges, we include the seven different box diagrams: ρN, ωN, σN, πN, $K\Lambda(1116)$, $K^*\Lambda(1116)$, and $K\Lambda(1520)$. Since the $K\Lambda(1520)$ box diagram is the most significant one among several possibie box diagram in describing ϕ photoproduction, we first discuss the $K^+\Lambda(1520)$ one and then deal with all other box diagrams in the next subsection. In The $\gamma N \to K^+\Lambda(1520)$ process was investigated within an effective Lagrangian method in Ref. [26] of which the results were in good agreement with the experimental data. Thus, we will take the formalism developed in Ref. [26] so that we may take into account the $K\Lambda(1116)$ coupled-channel effects more realistically.

The effective Lagrangians for $\gamma N \to K^+\Lambda(1520)$ are written as

$$\begin{aligned}
\mathcal{L}_{KN\Lambda^*} &= \frac{g_{KN\Lambda^*}}{M_K}\bar{N}\gamma_5\partial_\mu K^+\Lambda^{*\mu}, \\
\mathcal{L}_{\phi KN\Lambda^*} &= -i\frac{g_{KN\Lambda^*}}{M_K}g_{\phi KK}\bar{N}\gamma_5\phi_\mu K^+\Lambda^{*\mu}, \\
\mathcal{L}_{\phi KK} &= -ig_{\phi KK}(\partial^\mu K^- K^+ - \partial^\mu K^+ K^-)\phi_\mu, \\
\mathcal{L}_{\phi NN} &= -g_{\phi NN}\bar{N}\left[\gamma_\mu - \frac{\kappa_\phi}{2M_N}\sigma^{\mu\nu}\partial_\nu\right]\phi^\mu N, \\
\mathcal{L}_{\gamma KK} &= -ie(\partial^\mu K^- K^+ - \partial^\mu K^+ K^-)A_\mu, \\
\mathcal{L}_{\gamma NN} &= -e\bar{N}\left[\gamma^\mu - \frac{\kappa_N}{2M_N}\sigma^{\mu\nu}\partial_\nu\right]A_\mu N, \\
\mathcal{L}_{\gamma KN\Lambda^*} &= -i\frac{eg_{KN\Lambda^*}}{M_K}\bar{N}\gamma_5 A_\mu K^+\Lambda^{*\mu},
\end{aligned} \tag{7.1}$$

where K and $\Lambda^{*\mu}$ denote the K meson and $\Lambda(1520)$ fields. For $\Lambda(1520)$, we utilize the Rarita-Schwinger formalism. M_K is the kaon mass. The $KN\Lambda^*$ coupling constant is taken from Ref. [26], since we use the amplitude derived in it. The ϕKK coupling constant can be determined from the experimental data for the decay width $\Gamma_{\phi\to KK}$. On the other hand, $g_{\phi NN}$ is not much known experimentally. Recent experiments measuring the strange vector form factors imply that the strange quark gives almost no contribution to the nucleon electromagnetic (EM) form factors [18]. One can deduce from this experimental fact that the ϕNN coupling constant should be very small. In Ref. [35], the ϕNN was estimated by using a microscopic hadronic model with $\pi\rho$ continuum: $g_{\phi NN} = \pm 0.25$ and $\kappa_\phi = 0.2$, which are compatible with the recent data for the strange vector form factors. Thus, we will take these values in the present work. However, note that the s-channel contribution with the ϕNN vertex is almost negligible. In Table 7.1, the relevant strong coupling constants and anomalous magnetic moments are listed.

Based on the effective Lagrangians given in Eq.(7.1), we can write down the amplitude for the $K^+\Lambda^*(1520)$ box diagram. It contains both real and imaginary parts. The real part is divergent, which is also the case for other box diagrams and the rigorous calculation is rather involved. Thus we consider that the real part can be

Table 7.1: The strong coupling constants and anomalous magnetic moments used in the present work.

$g_{KN\Lambda^*}$	11	Ref. [26]
$g_{\phi KK}$	4.7	Ref. [24]
$g_{\phi NN}$	0.25	Ref. [35]
κ_p	1.79	Ref. [24]
κ_ϕ	0.2	Ref. [35]

taken into account effectively by the reenormalization of various coupling constants, and calculate only the imaginary part explicitly. The reasoning behind is similar to the concept of K-matrix formalism for the S-matrix. Physically, the imaginary part corresponds to rescattering and is obtained by the Landau-Cutkosky rule, Ref. [27, 28].

Having computed the Lorentz-invariant phase space volume factors, we obtain the imaginary part of the amplitude as

$$\mathrm{Im}\mathcal{M}_{K^+\Lambda^*\mathrm{box}} = -\frac{1}{8\pi}\frac{r}{\sqrt{s}}\int\frac{d\Omega}{4\pi}\mathcal{M}_L(\gamma p \to K^+\Lambda^*)\mathcal{M}_R^\dagger(K^+\Lambda^* \to \phi p), \tag{7.2}$$

where r is the magnitude of the K^+ momentum. This imaginary part of the amplitude is schematically drawn in Fig. 7.2. The shaded ellipse in the left-hand side represents the invariant amplitude for $\gamma p \to K^+\Lambda^*$, which is basically the same as that of Ref. [26] except for different form factors as will be explained later. It consists of three different types of the Feynman diagrams as shown below the left dashed arrow. On the other hand, the right ellipse stands for the $K^+\Lambda^* \to \phi p$ process that contains the diagrams below the right arrow, generically. Note that we use a similar method as in Ref. [25] but we choose the different form factors and parameters. The corresponding invariant amplitudes $\mathcal{M}_L(\gamma p \to K^+\Lambda^*)$ and $\mathcal{M}_R(K^+\Lambda^* \to \phi p)$ with the form factors are defined as follows:

$$\begin{aligned}
\mathcal{M}_L(\gamma p \to K^+\Lambda^*) &= (\mathcal{M}_{L,s} + \mathcal{M}_{L,t} + \mathcal{M}_{L,c})F_L(s,t), \\
\mathcal{M}_R(K^+\Lambda^{*\prime} \to \phi p) &= (\mathcal{M}_{R,s} + \mathcal{M}_{R,t} + \mathcal{M}_{R,c})F_R(s,t),
\end{aligned} \tag{7.3}$$

where $\mathcal{M}_{L,s}$ ($\mathcal{M}_{R,s}$), $\mathcal{M}_{L,t}$ ($\mathcal{M}_{R,t}$), and $\mathcal{M}_{L,c}$ ($\mathcal{M}_{R,c}$) represent the s-channel, the t-channel, and the contact-term contributions to the $\gamma p \to K^+\Lambda^*$ ($K^+\Lambda^* \to \phi p$) process, respectively:

$$\begin{aligned}
\mathcal{M}_{L,s} &= \frac{e g_{KN\Lambda^*}}{M_K}\bar{u}^\mu k_{2\mu}\gamma_5\frac{\not{k}_1 + \not{q} + M_N}{q^2 - M_N^2}\not{\epsilon}_\gamma u(p_1), \\
&+ \frac{e\kappa_p g_{KN\Lambda^*}}{2M_N M_K}\bar{u}^\mu k_{2\mu}\gamma_5\frac{\not{q} + M_N}{q^2 - M_p^2}\not{\epsilon}_\gamma \not{k}_1 u(p_1),
\end{aligned}$$

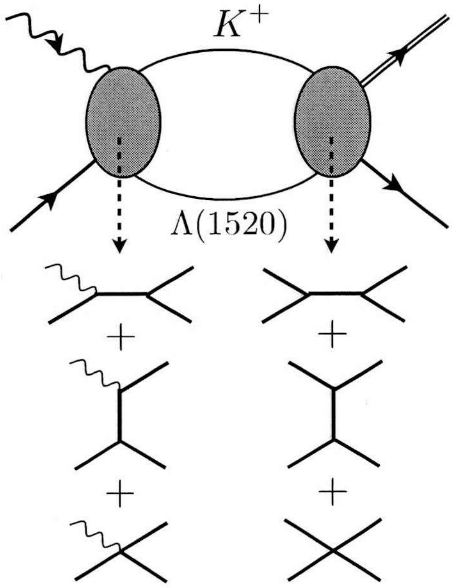

FIG. 7.2: Feynman diagrams for the $K^+\Lambda(1520)$ box. The form factors are introduced in a gauge-invariant way.

$$
\begin{aligned}
\mathcal{M}_{L,t} &= -\frac{2eg_{KN\Lambda^*}}{M_K}\bar{u}^\mu\gamma_5 u(p_1)\frac{q_K^\mu}{t_K-M_K^2},\\
\mathcal{M}_{L,c} &= \frac{eg_{KN\Lambda^*}}{M_K}\bar{u}^\mu\epsilon_\mu\gamma_5 u(p_1),\\
\mathcal{M}_{R,s} &= -i\frac{g_{KN\Lambda^*}g_{\phi NN}}{M_K}\bar{u}(p_2)\not{\epsilon}^*_\phi\frac{\not{q}+M_p}{q^2-M_p^2}\gamma_5 k_1^\alpha u^\alpha(p_1),\\
&\quad + i\frac{g_{KN\Lambda^*}g_{\phi NN}}{M_K}\frac{\kappa_\phi}{2M_p}\bar{u}(p_2)\not{k}_2\not{\epsilon}^*_\phi\frac{\not{q}+M_p}{q^2-M_p^2}\gamma_5 k_1^\alpha u^\alpha(p_1),\\
\mathcal{M}_{R,t} &= \frac{-ig_{KN\Lambda^*}g_{\phi KK}}{M_K}\frac{2k_1\cdot\epsilon^*_\phi}{q_K^2-M_K^2}\bar{u}(p_2)\gamma_5 q_t^\alpha u^\alpha(p_1),\\
\mathcal{M}_{R,c} &= \frac{-ig_{KN\Lambda^*}g_{KNN}}{M_K}\bar{u}(p_2)\gamma_5\epsilon^{*\mu}_\phi u^\mu(p_1).
\end{aligned}
\tag{7.4}
$$

We introduce the form factors $F_R(s,t)$ and $F_L(s,t)$ for $\mathcal{M}_R$ and $\mathcal{M}_L$, respectively, in particular, in a gauge-invariant manner for the $\gamma p \to K^+\Lambda^*$ rescattering:

$$
\begin{aligned}
F_R(s,t) &= \left[\frac{n_1\Lambda_1^4}{n_1\Lambda_1^4+(s-M_p^2)^2}\right]^{n_1}\left[\frac{n_2\Lambda_2^4}{n_2\Lambda_2^4+t^2}\right]^{n_2},\\
F_L(s,t) &= \left[\frac{n_3\Lambda_3^4}{n_3\Lambda_3^4+(s-M_p^2)^2}\right]^{n_3}\left[\frac{n_4\Lambda_4^4}{n_4\Lambda_4^4+t^2}\right]^{n_4},
\end{aligned}
\tag{7.5}
$$

where the cut-off masses Λ_i and powers n_i are fitted to the experimental data for the $\gamma p \to K^+\Lambda^*$ and

$\gamma p \to \phi p$, which are listed in Table 7.2. In Fig. 7.3, we draw the numerical result of the total cross section

Table 7.2: Cut-off parameters used in Eq.(7.5)

n_1	1
n_2	1
n_3	2
n_4	1
Λ_1	0.8 GeV
Λ_2	0.8 GeV
Λ_3	1.0 GeV
Λ_4	1.0 GeV

for $\gamma p \to K^+\Lambda^*$ in comparison with the experimental data taken from Ref. [37]. It is in good agreement with the data.

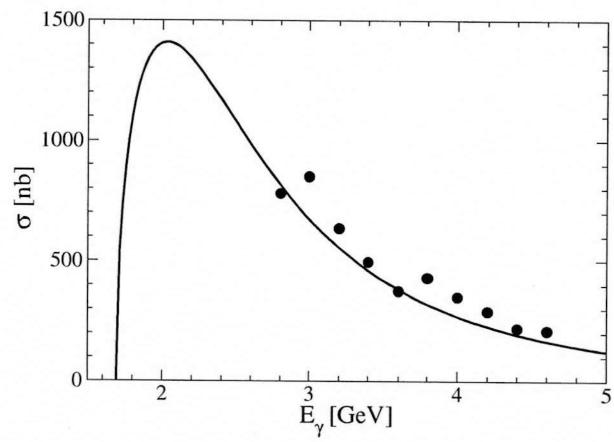

FIG. 7.3: Total cross-section of the $\gamma p \to K\Lambda(1520)$ reaction as compared to the experimental data [37].

7.2.2 All other box diagrams

In the same manner as done for the $K^+\Lambda^*$ box diagram, we consider the six intermediate box diagrams as shown in Fig.7.4, i.e. the ρN, ωN, σN, πN, $K\Lambda(1116)$, and $K^*\Lambda(1116)$ box diagrams. ρ photoproduction has been studied theoretically [38, 39, 40, 41] in which the contributions of the t-channel π- and σ-exchanges were considered and σ-exchange was found to be the dominant one, since it selects the isovector part of the EM current. Thus, we take into account the ρp box diagram with the σ- and π-exchanges in the t-channel, as shown in the first diagram of Fig. 7.4. We will show later in Fig. 7.5 that indeed the σ-exchange describes qualitatively well the $\gamma p \to \rho p$ reaction. In Ref. [38] ω photoproduction was also

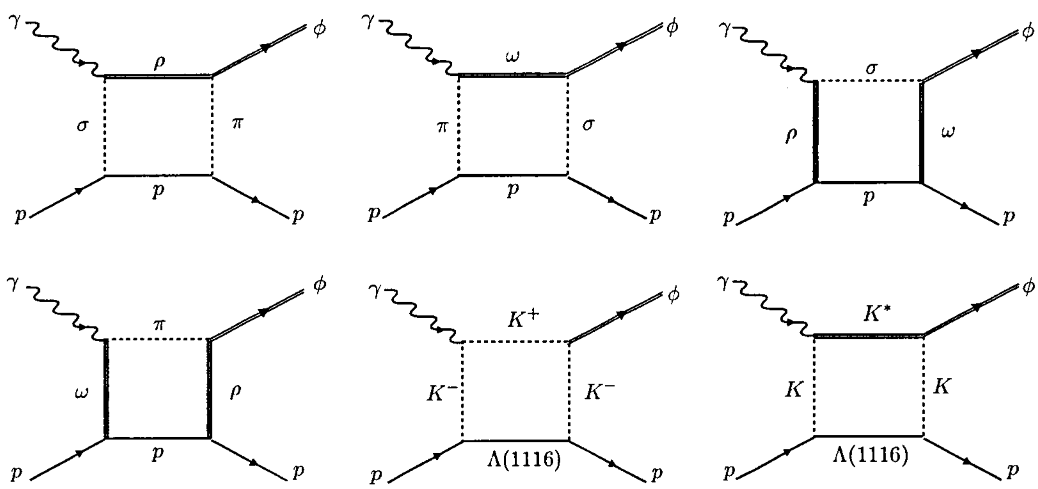

FIG. 7.4: Feynman diagrams for the six hadronic box contributions.

discussed within the same framework. In contrast to the $\gamma p \to \rho p$ reaction, the π-exchange appeared to be dominant, since it picks up the isoscalar part of the EM current. Correspondingly, we consider the ωp box contribution as in the second diagram of Fig. 7.4, where ω is produced by the one pion exchange. The σp and πp box diagrams are obtained by reversing the ρp and ωp box diagrams. The $\gamma p \to K\Lambda(1116)$ and $\gamma p \to K^*\Lambda(1116)$ reactions were measured by several experimental collaborations [42, 43, 44, 45, 46, 47] and were investigated theoretically [48, 49, 50, 51, 52]. While we consider all the relevant diagrams for the $K\Lambda^*(1520)$ box contribution because of its significance, we will take into account only the K-exchange diagrams in the t-channel for the $K\Lambda$ and $K^*\Lambda$ box diagrams, since these two box diagrams turn out to have tiny effects on ϕ photoproduction.

The relevant effective Lagrangians for these box diagrams are given as follows:

$$
\begin{aligned}
\mathcal{L}_{\gamma\rho\sigma} &= \frac{g_{\gamma\rho\sigma}}{m_\rho}[\partial_\mu A_\nu \partial^\mu \rho^\nu - \partial_\mu A_\nu \partial^\nu \rho^\mu]\sigma, \\
\mathcal{L}_{\sigma NN} &= g_{\sigma NN}\bar{N}N\sigma, \\
\mathcal{L}_{\pi^0 NN} &= -ig_{\pi NN}\bar{N}\gamma_5\tau_3 N\pi^0, \\
\mathcal{L}_{\pi\rho\phi} &= \frac{g_{\pi\rho\phi}}{m_\phi}\epsilon_{\mu\nu\alpha\beta}\partial^\nu\phi^\mu\partial^\beta\rho^\alpha\pi_0, \\
\mathcal{L}_{\omega\phi\sigma} &= \frac{g_{\omega\phi\sigma}}{m_\phi}(\partial_\mu\omega_\nu\partial^\mu\phi^\nu - \partial_\mu\omega_\nu\partial^\nu\phi^\mu), \\
\mathcal{L}_{\gamma\omega\pi} &= \frac{g_{\gamma\omega\pi}}{m_\omega}\epsilon_{\mu\nu\alpha\beta}\partial^\nu A^\mu\partial^\beta\omega^\alpha\pi^0, \\
\mathcal{L}_{VNN} &= -g_{VNN}\bar{N}\left(\gamma_\mu V^\mu - \frac{\kappa_V}{2M_N}\sigma^{\mu\nu}\partial_\nu V_\mu\right)N\,, \quad (V=\omega,\,\rho), \\
\mathcal{L}_{\gamma KK} &= -ie\left[(\partial^\mu K^+)K^- - (\partial^\mu K^-)K^+\right]A_\mu,
\end{aligned}
$$

$$
\begin{aligned}
\mathcal{L}_{\phi KK} &= ig_{\phi KK}\left[(\partial^\mu K^+)K^- - (\partial^\mu K^-)K^+\right]\phi_\mu, \\
\mathcal{L}_{KN\Lambda} &= -ig_{KP\Lambda}\bar{\Lambda}\gamma_5 N K^-, \\
\mathcal{L}_{\gamma KK^*} &= \frac{g_{\gamma KK^*}}{m_{K^*}}\epsilon_{\mu\nu\alpha\beta}\partial^\nu A^\mu \partial^\beta K^{*\alpha}K, \\
\mathcal{L}_{\phi KK^*} &= \frac{g_{\phi KK^*}}{m_\phi}\epsilon_{\mu\nu\alpha\beta}\partial^\nu \phi^\mu \partial^\beta K^{*\alpha}K,
\end{aligned}
\tag{7.6}
$$

where the coupling constants and the cut-off masses are listed in Table 7.3. The invariant amplitudes for

Table 7.3: Coupling constants and cut-off masses used in box diagrams of Fig. 7.4

$g_{\gamma\rho\sigma}$	0.82	Ref.[38]
$g_{\sigma NN}$	10.026	Ref.[38]
$g_{\pi NN}$	13.26	Ref.[38]
$g_{\pi\rho\phi}$	-1.258	Ref.[24]
$g_{\phi\omega\sigma}$	-0.45	Ref.[24]
$g_{\gamma\omega\pi}$	0.557	Ref.[24]
$g_{\omega NN}$	10.35	Ref.[34]
$g_{\rho NN}$	3.72	Ref.[34]
$g_{\phi KK}$	4.48	Ref.[24]
$g_{KN\Lambda}$	-13.26	Ref.[54]
$g_{\gamma KK^*}$	0.254 GeV^{-1}	Ref.[24]
$g_{\phi KK^*}$	10.74	Ref.[24, 53]
κ_ω	0	Ref.[34]
κ_ρ	6.1	Ref.[56]
$\Lambda_{\pi\rho\phi}$	1.05 GeV	Ref.[31]
$\Lambda_{\pi NN}$	1.05 GeV	Ref.[31]
$\Lambda_{\gamma\rho\sigma}$	1.05 GeV	Ref.[38]
$\Lambda_{\sigma NN}$	1.1 GeV	Ref.[38]
Λ_σ	1 GeV	Ref.[38]
$\Lambda_{\sigma\rho\rho}$	0.9 GeV	Ref.[38]
$\Lambda_{\sigma\omega\phi}$	0.9 GeV	Ref.[24]
$\Lambda_{\pi\gamma\omega}$	0.6 GeV	Ref.[34]
Λ_V	1.227 GeV	Ref.[57]
Λ_K	1 GeV	

these box diagrams are derived as follows:

$$
\begin{aligned}
\mathcal{M}_{1,L} &= \frac{g_{\gamma\rho\sigma}g_{\sigma NN}}{M_\rho(t_\sigma - M_\sigma^2)}\left[(k_1\cdot r)(\epsilon_\gamma\cdot\epsilon_\rho^*) - (k_1\cdot\epsilon_\rho^*)(\epsilon_\gamma\cdot r)\right]\bar{u}(q)u(p_1)\left\{\frac{\Lambda_{\gamma\rho\sigma}^2 - M_\sigma^2}{t_\sigma - M_\sigma^2}\cdot\frac{\Lambda_{\sigma NN}^2 - M_\sigma^2}{t_\sigma - M_\sigma^2}\right\}, \\
\mathcal{M}_{1,R} &= \frac{-ig_{\phi\rho\pi}g_{\pi NN}}{M_\phi(t_\pi - M_\pi^2)}\epsilon_{\mu\nu\alpha\beta}\epsilon_\phi^{*\mu}k_2^\nu\epsilon_\rho^\alpha r^\beta\bar{u}(p_2)\gamma_5 u(q)\times\left\{\frac{\Lambda_{\phi\rho\pi}^2 - M_\pi^2}{t_\pi - M_\pi^2}\cdot\frac{\Lambda_{\pi NN}^2 - M_\sigma^2}{t_\pi - M_\pi^2}\right\},
\end{aligned}
$$

$$
\begin{aligned}
\mathcal{M}_{2,L} &= \frac{-ig_{\gamma\omega\pi}g_{\pi NN}}{M_\omega(t_\pi - M_\pi^2)}\epsilon_{\mu\nu\alpha\beta}\epsilon_\gamma^\mu k_1^\nu \epsilon_\omega^{*\alpha} r^\beta \bar{u}(q)\gamma_5 u(p_1) \times \left\{\frac{\Lambda_{\gamma\omega\pi}^2 - M_\pi^2}{t_\pi - M_\pi^2}\cdot\frac{\Lambda_{\pi NN}^2 - M_\pi^2}{t_\pi - M_\pi^2}\right\}, \\
\mathcal{M}_{2,R} &= \frac{-ig_{\phi\omega\sigma}g_{\sigma NN}}{M_\phi(t_\sigma - M_\sigma^2)}\bar{u}(p_2)u(q)\left[(r\cdot k_2)(\epsilon_\omega\cdot\epsilon_\phi^*) - (r\cdot\epsilon_\phi^*)(k_2\cdot\epsilon_\omega)\right] \\
&\quad \times\left\{\frac{\Lambda_{\phi\omega\sigma}^2 - M_\sigma^2}{t_\sigma - M_\sigma^2}\cdot\frac{\Lambda_{\sigma NN}^2 - M_\sigma^2}{t_\sigma - M_\sigma^2}\right\}, \\
\mathcal{M}_{3,L} &= \frac{g_{\rho NN}g_{\gamma\rho\sigma}}{M_\rho(t_\rho - M_\rho^2)}\left[k_1^\alpha(\epsilon_\gamma\cdot r) - \epsilon_\gamma^\alpha(k_1\cdot r)\right]\bar{u}(p_2)\left[\gamma_\alpha(1+\kappa_\rho) - \frac{\kappa_\rho}{M_p}q^\alpha\right]u(p_1) \\
&\quad \times\left\{\left(\frac{\Lambda_\rho^2}{\Lambda_\rho^2 - (k_1 - r)^2}\right)^2\right\}, \\
\mathcal{M}_{3,R} &= \frac{g_{\omega NN}g_{\phi\omega\sigma}}{M_\phi(t_\omega - M_\omega^2)}\left[(r\cdot\epsilon_\phi^*)k_2^\mu - (r\cdot k_2 - M_\phi^2)\epsilon_\phi^{*\mu}\right] \\
&\quad \times\bar{u}(p_1)\left[\gamma_\mu(1+\kappa_\omega) - \frac{\kappa_\omega}{2M_p}q_\mu\right]u(q)\left\{\left(\frac{\Lambda_\omega^2}{\Lambda_\omega^2 - (r - k_2)^2}\right)^2\right\}, \\
\mathcal{M}_{4,L} &= \frac{-g_{\omega NN}g_{\gamma\omega\pi}}{M_\omega(t_\omega - M_\omega^2)}\epsilon_{\mu\nu\alpha\beta}\epsilon_\gamma^\mu k_1^\nu r^\beta \bar{u}(q)\left[\gamma^\alpha(1+\kappa_\omega) - \frac{\kappa_\omega}{M_P}q^\alpha\right]u(p_1) \\
&\quad \times\left\{\left(\frac{\Lambda_\omega^2}{\Lambda_\omega^2 - (r - k_2)^2}\right)^2\right\}, \\
\mathcal{M}_{4,R} &= \frac{-g_{\rho NN}g_{\phi\rho\pi}}{M_\phi(t_\rho - M_\rho^2)}\epsilon_{\mu\nu\alpha\beta}\epsilon_\phi^{*\mu}k_2^\nu r^\beta \bar{u}(p_2)\left[\gamma^\alpha(1+\kappa_\rho) - \frac{\kappa_\rho}{M_N}ql^\alpha\right]u(q), \\
&\quad \times\left\{\left(\frac{\Lambda_\rho^2}{\Lambda_\rho^2 - (k_1 - r)^2}\right)^2\right\}, \\
\mathcal{M}_{5,L} &= \frac{-2ieg_{KP\Lambda}}{(t_L - M_K^2)}(r\cdot\epsilon_\gamma)\bar{u}(q)\gamma_5 u(p_1)\times\left\{\left(\frac{\Lambda_K^2 - M_K^2}{t_K - M_K^2}\right)^2\right\}, \\
\mathcal{M}_{5,R} &= \frac{2ig_{\phi KK}g_{KP\Lambda}}{(t_R^2 - M_K^2)}(r\cdot\epsilon_\phi^*)\bar{u}(p_2)\gamma_5 u(q)\times\left\{\left(\frac{\Lambda_K^2 - M_K^2}{t_K - M_K^2}\right)^2\right\}, \\
\mathcal{M}_{6,L} &= \frac{-ig_{\gamma KK^*}g_{KP\Lambda}}{M_{K^*}(t_L - M_K^2)}\epsilon_{\mu\nu\alpha\beta}\epsilon_{\gamma\mu}k_1^\nu\epsilon_{K^*}^\alpha r^\beta\bar{u}(q)\gamma_5 u(p_1)\times\left\{\left(\frac{\Lambda_K^2 - M_K^2}{\Lambda_K^2 - t_K}\right)^2\right\}, \\
\mathcal{M}_{6,R} &= \frac{ig_{\phi KK^*}g_{KP\Lambda}}{M_\phi(t_R - M_K^2)}\epsilon_{\mu\nu\alpha\beta}\epsilon_\phi^{*\mu}k_2^\nu\epsilon_{K^*}^\alpha r^\beta\bar{u}(p_2)\gamma_5 u(q)\times\left\{\left(\frac{\Lambda_K^2 - M_K^2}{\Lambda_K^2 - t_K}\right)^2\right\},
\end{aligned}
\tag{7.7}
$$

where the subscripts $1,\cdots 6$ correspond to the box diagrams appearing in Fig. 7.4 in order. The other subscripts L and R denote the $\gamma p \to MB$ and $MB \to \phi p$ parts, respectively. In Figs. 7.5 and 7.6 we draw the results of the total cross sections for the $\gamma p \to \rho p$ and $\gamma p \to \omega p$ reactions, respectively. The results are qualitatively in agreement with the experimental data.

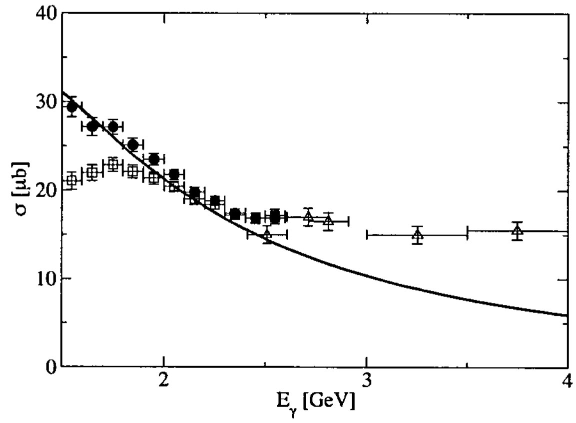

FIG. 7.5: Total cross-section of the $\gamma p \longrightarrow \rho^0 p$ reaction. The solid curve depicts the present result obtained from the t-channel σ-exchange diagram. The closed circles and the open squares are taken from Ref. [58], where as the open triangles represent those from Ref. [59].

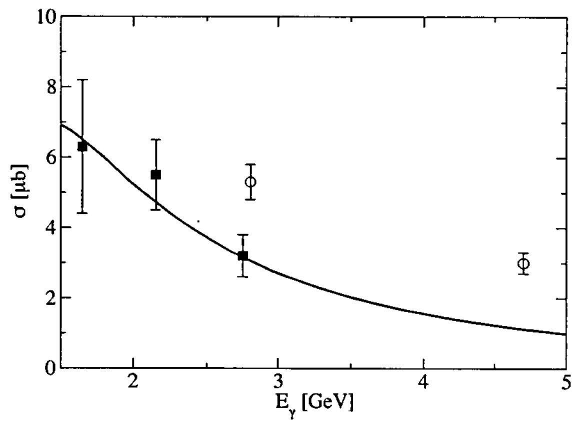

FIG. 7.6: Total cross-section of the $\gamma p \longrightarrow \omega p$ reaction. The solid curve depicts the present result obtained from the t-channel π-exchange diagram. The closed squares denote the experimental data from Ref. [60] whereas the open circles represent those from Ref. [61].

7.3 Numerical result and discussion

We are now in a position to discuss the numerical results for ϕ photoproduction. We start with the differential cross section at the forward angle $d\sigma/dt(\theta = 0)$ as a function of the photon energy E_γ in the laboratory frame. The parameters are determined in the following manner. Since the the Pomeron-exchange in the low-energy region is not much understood, we fit the parameter for the overall strength C_p and that for the threshold $s_{\rm th}$ in Eq.(5.4) in such a way that the Pomeron-exchange reproduces the high energy behavior of the differential cross section: $C_p = 8\,\mathrm{GeV}^{-1}$ and $s_{\rm th} = 3.83\,\mathrm{GeV}^2$. On the other hand, We fix the cut-off parameters for the $K\Lambda^*(1520)$ box diagrams to describe the E_γ dependence of $d\sigma/dt$ in lower energy region, in particular, to explain the well-known bum-like structure around $E_\gamma \approx 2.3$ GeV. The parameters

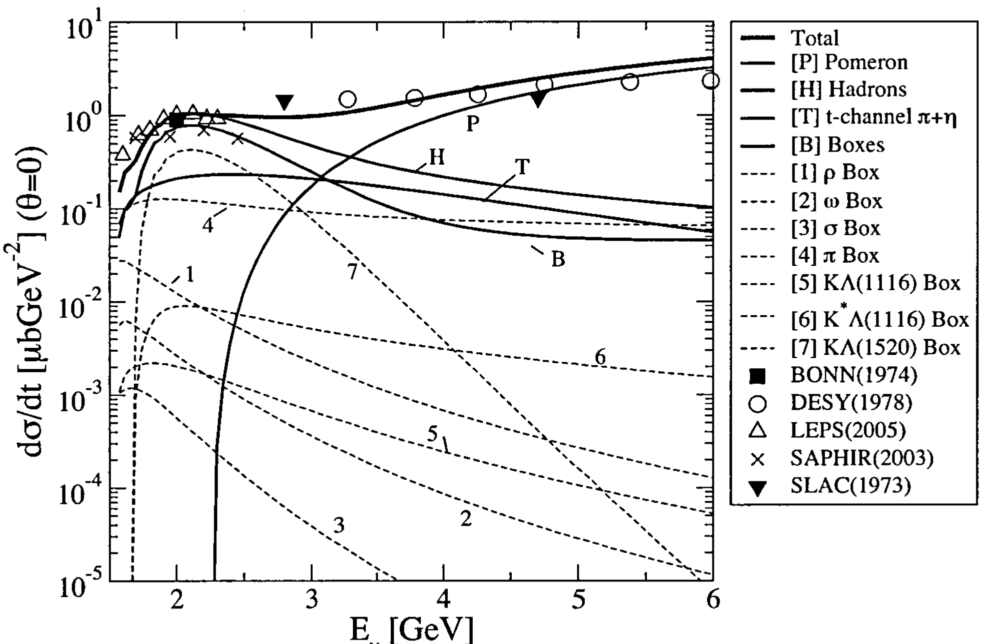

FIG. 7.7: Differential cross section as a function of the photon energy E_γ. The thick solid curve depicts the result with all contributions included. The solid curves with the symbols P, T, B and H represent the Pomeron contribution, those of π- and η-exchanges, those of all the box diagrams, and the total contribution of hadronic diagrams ($T + B$), respectively. The dashed curves with numbers in order denote the effects of the seven box diagrams separately.

of all other hadronic diagrams are taken from existing references as explained in the previous section.

Figure 7.7 illustrates various contributions to $d\sigma/dt(\theta = 0)$ as a function of the photon energy E_γ from the Pomeron-exchange, the t-channel π- and η exchanges, and seven box diagrams. The solid curve with symbol P draws the contribution of the the Pomeron-exchange to $d\sigma/dt$. As expected, it governs E_γ dependence in the higher energy region ($E_\gamma \geq 3$GeV). Note, however, that the Pomeron does not contribute to $d\sigma/dt$ below around $E_\gamma = 2.3\,\text{GeV}$ in the present work. The π- and η-exchanges provide a certain amount of effects on the differential cross section (solid curve with symbol T). The contribution of the π- and η-exchanges start to increase from the threshold energy and then it decreases very slowly when it reaches approximately 3 GeV. Thus, the effects of the π- and η-exchanges are quite important in the lower E_γ energy region up to 3 GeV, where the Pomeron-exchange overtakes the π- and η-exchanges.

Except for the $K\Lambda^*(1520)$ box diagram, all other box contributions turn out to be negligibly small. However, the $K\Lambda^*(1520)$ box diagram plays an essential role in describing the experimental data for $d\sigma/dt$ in the lower E_γ region, in particular, in explaining the bump-like structure near 2.3 GeV. This is very different from the conclusion of Ref. [25], where the $K\Lambda^*(1520)$ seems to be suppressed in the K-matrix formalism. The reason lies in the fact that we have introduced different form factors for the $\gamma p \to K\Lambda^*$

and $K\Lambda^* \to \phi p$ reactions. In general, form factors are given as functions of two Mandelstam variables for the box diagrams, i.e. $F(s,\, t)$, since we have two off-shell particles in the s-channel and other two off-shell particles in the t-channel. However, it is very difficult to preserve the gauge invariance in the presence of the form factors. Thus, we have introduced a type of overall form factors to keep the gauge invariance in the $\gamma p \to K\Lambda^*$ part, as written in Eq.(7.5). To keep the consistency, we also have included a similar type of the form factors in the $K\Lambda^* \to \phi p$ part. With these form factors considered, we find that the $K\Lambda^*$ box diagram is indeed enhanced as shown in Fig. 7.7 in comparision with Ref. [25]. The contribution of the $K\Lambda^*$ box diagram increases sharply up to $E_\gamma \approx 2$ GeV and then falls off linearly. The result of the $K\Lambda^*$ box diagram indicates that the off-shell effects, which arise from the form factors and the rescattering equation, may come into play.

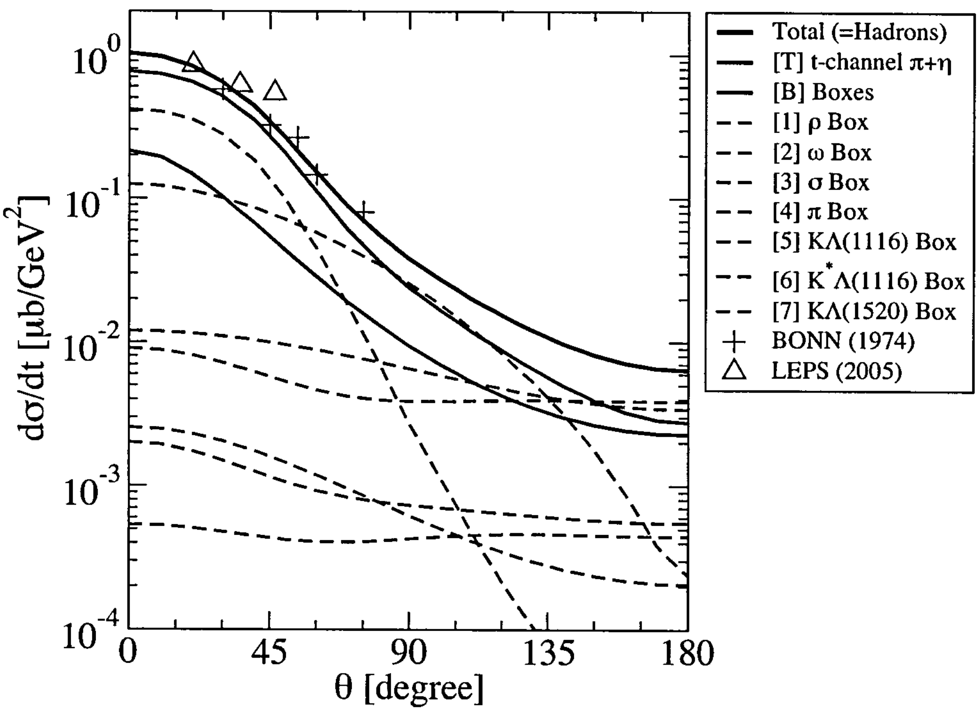

FIG. 7.8: The differential cross section as a function of the scattering angle θ with the photon energy at $E_\gamma = 2$ GeV. The thick solid curve depicts the result with all hadronic contributions included. The solid curves with the symbols T and B represent the contribution of the π- and η-exchanges and those of all the box diagrams, respectively. The dashed curves with numbers in order denote the effects of the seven box diagrams separately.

Considering the fact that the $K^*\Lambda$ threshold energy ($E_{\rm th} \approx 2$ GeV) is very close to that of ϕ photoproduction ($E_{\rm th} \approx 1.96$ GeV), one might ask why the contribution of the $K^*\Lambda$ is suppressed. While the $K\Lambda^*(1520)$ channel ($E_{\rm th} \approx 2$ GeV) is directly related to ϕp, since both are the subreactions of the

$\gamma p \to K\bar{K}p$ process, the $\gamma p \to K^*\Lambda$ reaction is distinguished from those two reactions, because the $K^*\Lambda$ channel is related to $\gamma p \to \pi K\Lambda$ reaction. Thus, one can qualitatively understand why the contribution of the $K^*\Lambda$ box diagrams is suppressed.

In Fig. 7.8, the differential cross section as a function of the scattering angle is depicted at $E_\gamma = 2$ GeV. Since the Pomeron-exchange is suppressed at this photon energy because of $s_{\rm th} = 2.3$ GeV, we can examine each hadronic contribution to the differential cross section more in detail. Figure 7.8 clearly shows that the $K\Lambda(1520)$ box diagram is the most dominant one among the hadronic contributions. Adding all the effects of the box diagrams, we find that the box contributions almost describe the θ dependence. Together with the π- and η-exchanges, the result of the differential cross section is in good agreement with the experimental data [21, 62].

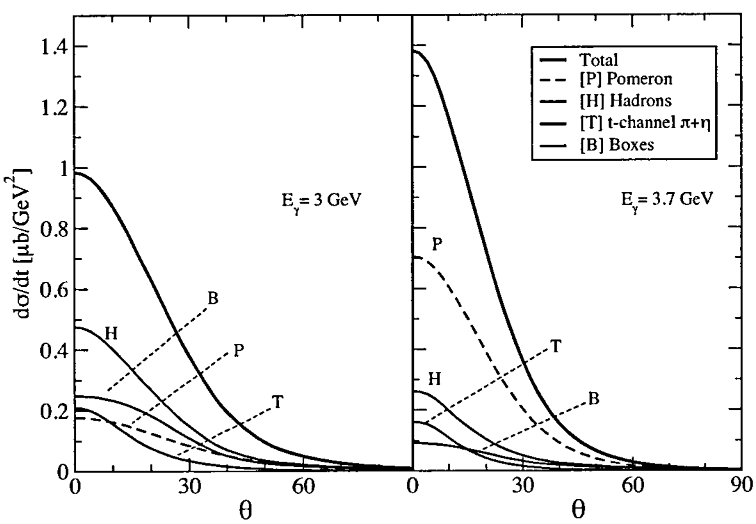

FIG. 7.9: The differential cross section as a function of the scattering angle θ with two different photon energies $E_\gamma = 3$ GeV and 3.7 GeV. The thick solid curve depicts the result with all contributions included. The solid curves with the symbols P, T, B and H represent the Pomeron contribution, those of π- and η-exchanges, those of all the box diagrams, and the total contribution of hadronic diagrams ($T + B$), respectively.

The differential cross section as a function the scattering angle are drawn in Fig. 7.9. The left and right panels correspond to the photon energies $E_\gamma = 3$ and 3.7 GeV, respectively. As expected, the hadronic contribution is dominant over the Pomeron-exchange at the lower photon energy, while at $E_\gamma = 3.7$ GeV, the Pomeron governs the $\gamma p \to \phi p$ process. Interestingly, the effects of the box diagrams, in particular, the $K\Lambda^*(1520)$ one, turn out to be larger than those of the π- and η-exchanges, whereas the box diagrams seem to be suppressed at higher photon energies. It implies that the $K\Lambda^*(1520)$ box diagram influences ϕ photoproduction only in the vicinity of the threshold energy. Figure 7.10 depicts the results of the differential

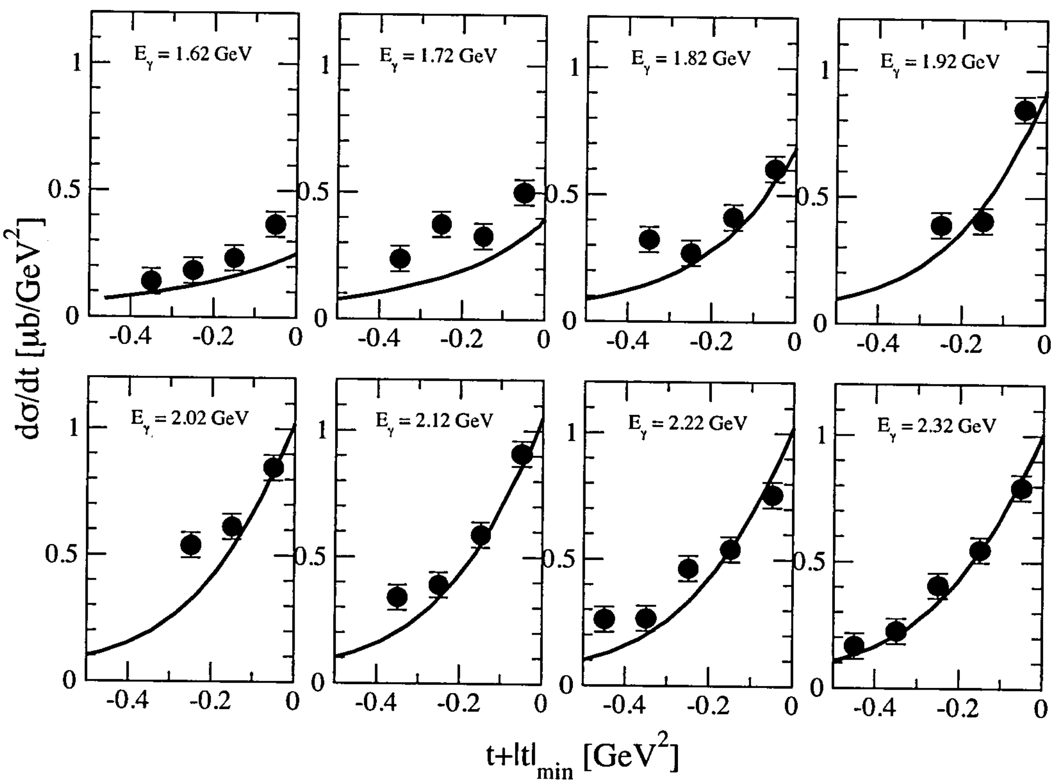

FIG. 7.10: Differential cross sections of the $\gamma p \to \phi p$ reaction as a function of $t + |t|_{\rm min}$ with eight different photon energies. The experimental data are taken from Ref. [21].

cross section as a function of $t + |t|_{\rm min}$ with eight different photon energies, where $|t|_{\rm min}$ is the minimum 4-momentum transfer from the incident photon to the ϕ meson. The results are in good agreement with the experimental data taken from the measurement of the LEPS collaboration [21].

It is of great importance to examine the angular distribution of the $\phi \to K^+K^-$ decay in the ϕ rest frame or in the Gottfried-Jackson (GJ) frame, since it makes the helicity amplitudes accessible to experimental investigation [63, 64]. The detailed formalism for the angular distribution of the ϕ meson decay can be found in Refs. [64, 23]. The decay angular distribution of ϕ photoproduction was measured at SAPHIR/ELSA [65] but the range of the photon energy is too wide. On the other hand, the LEPS collaboration measured the decay angular distribution at forward angles $(-0.2 < t + |t|_{\rm min})$ in two different energy regions: $1.97 < E_\gamma < 2.17$ GeV and $2.17 < E_\gamma < 2.37$ GeV [21], which are related to the energy around the local maximum of the cross section and that above the local maximum, respectively. Therefore, we have computed the decay angular distributions at two photon energies, i.e. $E_\gamma = 2.07$ GeV and $E_\gamma = 2.27$ GeV, which correspond to the center values of the given ranges of E_γ in the LEPS experiment.

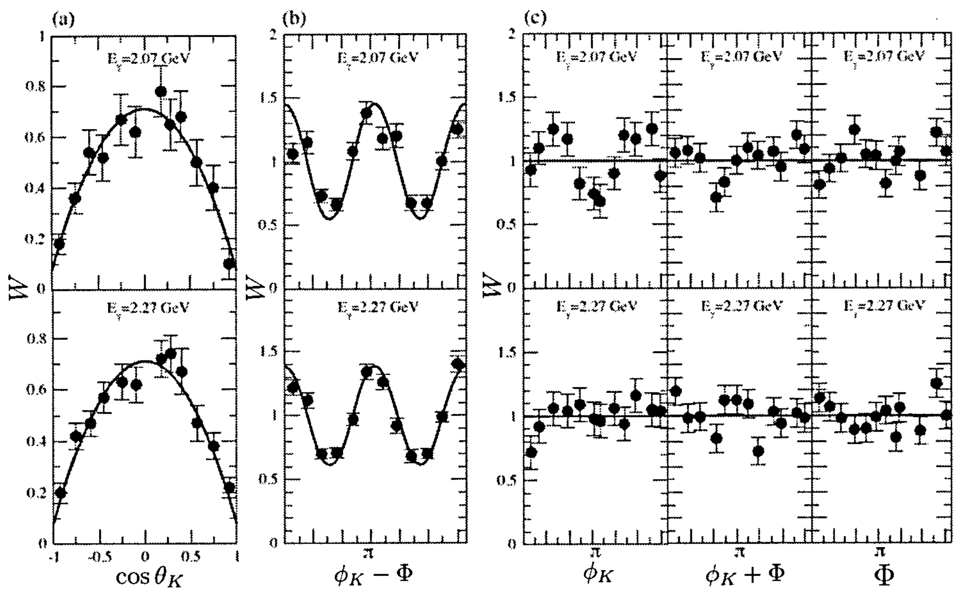

FIG. 7.11: The decay angular distributions for $-0.2 < t + |t|_{\rm min}$ in the Gottfried-Jackson frame. We take the center values of the energy ranges measured by the LEPS collaboration [21], i.e. $E_\gamma = 2.07$ GeV and $E_\gamma = 2.27$ GeV. The experimental data are taken from Ref. [21].

The one-dimensional decay angular distributions $W(\cos\theta_K)$, $W(\phi_K - \Phi)$, $W(\phi_K)$ are presented in Fig. 7.11, which are expressed respectivley as

$$\begin{aligned}
W(\cos\theta_K) &= \frac{1}{2}(1-\rho^0_{00}) + \frac{1}{2}\left(3\rho^0_{00} - 1\right)\cos^2\theta_K, \\
2\pi W(\phi_K - \Phi) &= 1 + 2p_\gamma \bar{\rho}^1_{1-1}\cos 2(\phi_K - \Phi), \\
2\pi W(\phi_K) &= 1 - 2\mathrm{Re}\rho^0_{1-1}\cos 2\phi_K, \\
2\pi W(\phi_K + \Phi) &= 1 + 2p_\gamma \Delta_{1-1}\cos 2(\phi_K + \Phi), \\
2\pi W(\Phi) &= 1 + 2p_\gamma \rho' \cos 2\Phi,
\end{aligned} \tag{7.8}$$

where θ_K and ϕ_K denote the polar azimuthal angles of the decay particle K^+ in the GJ frame. Φ represents the azimuthal angle of the photon polarization in the center-of-mass frame. [1] P_γ stands for the degree of polarization of the photon beam. $\bar{\rho}^1_{1-1}$, Δ_{1-1}, and ρ' are defined as

$$\begin{aligned}
\bar{\rho}^1_{1-1} &= \frac{1}{2}(\rho^1_{1-1} - \mathrm{Im}\rho^2_{1-1}), \\
\Delta_{1-1} &= \frac{1}{2}(\rho^1_{1-1} + \mathrm{Im}\rho^2_{1-1}), \\
\rho' &= 2\rho^1_{11} + \rho^1_{00}.
\end{aligned} \tag{7.9}$$

[1]Definitions of the angles are well described in appendix B.

The expressions for the spin-density matrix elements $\rho^{\alpha}_{\lambda\lambda'}$ with the helicities λ and λ' for the ϕ meson can be found in Appendix B .

The panel (a) of Fig. 7.11 draws the one-dimensional decay polar-angle distributions $W(\cos\theta_K)$. As pointed out by Refs. [21, 22], the decay distribution behaves approximately as $\sim$ $(3/4)\sin^2\theta_K$, which indicates that the helicity-conserving processes are dominant as shown in Eq.(7.8). It means that t-exchange particles with unnatural parity at the tree level do not contribute to $W(\cos\theta_K)$. As will be discussed later, ρ^0_{00} from the π- and η-exchanges, which is related to the single spin-flip amplitude in the GJ frame, exactly vanishes. On the other hand, all hadronic box diagrams contribute to it. Though the Pomeron-exchange might contribute to this spin-density matrix element, it does not play any role below 2.3 GeV. The panel (b) of Fig. 7.11 shows the results of $W(\phi_K-\Phi)$, which are in good agreement with the LEPS data, whereas the panel (c) depicts those of $W(\phi_K)$, $W(\phi_K+\Phi)$, and $W(\Phi)$, respectively, which deviate from the data. In fact, the data show somewhat irregular behavior which does not seem to be easily reproduced.

Table 7.4: ϕ density matrix in the forward scattering at $E_\gamma = 2$ GeV

	ρ^0_{00}	$\overline{\rho}^1_{1-1}$	$\mathrm{Re}\rho^0_{1-1}$	Δ_{1-1}	ρ'
t-channel $\pi^0+\eta$	0	-0.5	0	0	0
ρ box	0.651	-0.175	2.97×10^{-4}	-8.94×10^{-6}	1.37×10^{-2}
ω box	0.035	-0.48	9.26×10^{-4}	-8.72×10^{-7}	-1.05×10^{-3}
σ box	0.254	-0.066	-8.85×10^{-3}	2.03×10^{-4}	-7.93×10^{-4}
π box	0.061	0.448	5.57×10^{-4}	1.79×10^{-4}	1.15×10^{-3}
$K\Lambda(1116)$ box	0.025	0.488	-1.08×10^{-2}	7.85×10^{-5}	-2.21×10^{-2}
$K^*\Lambda(1116)$ box	0.030	0.485	1.39×10^{-3}	1.10×10^{-6}	2.06×10^{-3}
$K^+\Lambda(1520)$ box	3.1×10^{-4}	0.499	-2.95×10^{-3}	5.131×10^{-6}	-6.02×10^{-3}
box all	6.62×10^{-2}	0.455	2.46×10^{-4}	1.74×10^{-4}	5.69×10^{-4}
hadrons	5.13×10^{-2}	0.24	5.64×10^{-4}	1.34×10^{-4}	-1.99×10^{-4}

As shown in Fig. 7.11, the decay angular distributions shed light on the production mechanism of the ϕ meson, since they make it possible to get access experimentally to the spin-density matrix elements, or the helicity amplitudes of ϕ photoproduction. It has important physical implications, because even though some diagrams seem to contribute negligibly to the cross sections, they might have definite effects on the decay angular distributions. In Table 7.4, The contributions of each box diagram to the various spin-density matrix elements at $E_\gamma = 2\,\mathrm{GeV}$ are listed. As expected, the π- and η-exchanges contribute only to $\overline{\rho}^1_{1-1}$. The hadronic box diagrams mainly contribute to ρ^0_{00} and $\overline{\rho}^1_{1-1}$ and are almost negligible to other components. Interestingly, the ρp box diagram is the dominant one for ρ^0_{00}, even though it provides much smaller effects on the differential cross section than the $K\Lambda^*(1520)$ one.

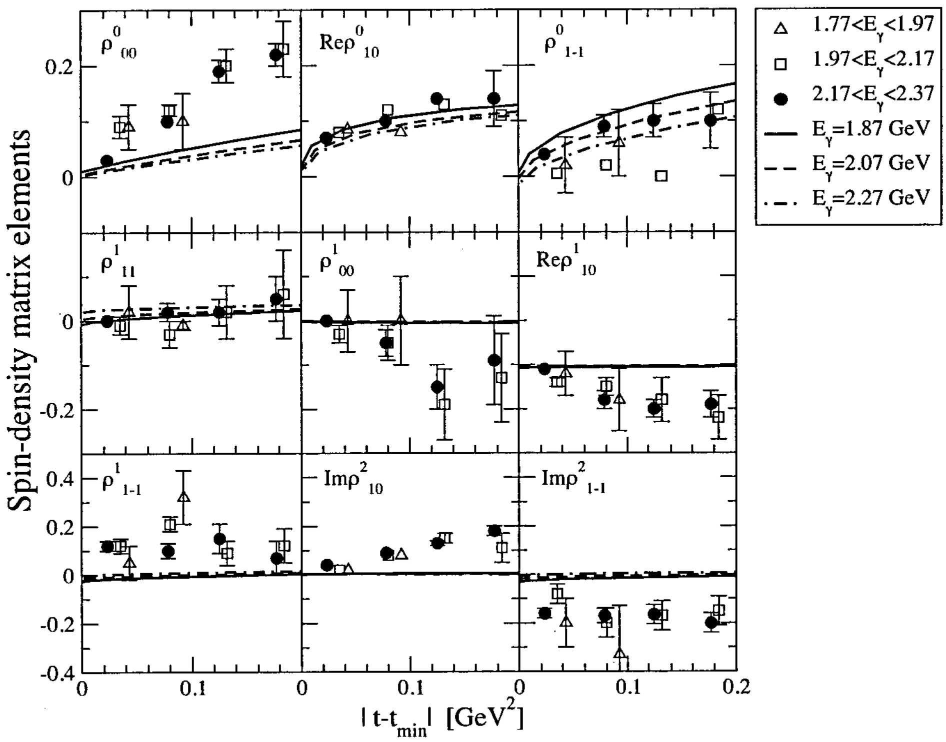

FIG. 7.12: The density matrix elements as a function of $|t - t_{\rm min}|$ for three different photon energies, i.e. 1.87 GeV, 2.07 GeV, and 2.27 GeV, to which the solid, dotted, and dot-solid curves correspond. The experimental data with three different ranges of the photon energy are taken from Ref. [22].

Rcently, the LEPS experiment measured the spin-density matrix elements for $\gamma p \to \phi p$ [22] in the range of $E_\gamma = 1.6 - 2.4$ GeV in which the Pomeron-exchange does not play any important role, in particular, in the present approach. Thus, we can examine the hadronic contributions to each spin-density matrix elements. Figure 7.12 illustrates the various spin-density matrix elements, compared with the LEPS data. Since the experimental data are given in the finite range of E_γ, we just take the three center values corresponding to the ranges, i.e. $E_\gamma = 1.87$, 2.07, 2.27 GeV. The hadronic diagrams considered in the present work describe quantitatively $\mathrm{Re}\rho^0_{10}$, ρ^0_{1-1} and ρ^1_{11}. However, the deviations are found in other spin-density matrix elements as $t - |t|_{\rm min}$ increases.

7.4 Summary

In the present work, we aimed at investigating the coupled-channel effects arising from the hadronic intermediate box diagrams to ϕ photoproduction near the threshold region in addition to the Pomeron-, π-, and η-exchanges. In particular, the bump-like structure near $E_\gamma \approx 2.3$ GeV, which was reported by the LEPS experiment [21], sheds light on the production mechanism of the ϕ meson in the vicinity of the threshold, since the Pomeron-exchange was shown to be not enough to explain this peculiar structure of ϕ photoproduction. Thus, we studied in detail the effects of the seven different box diagrams such as ρN, ωN, σN, πN, $K\Lambda(1116)$, $K^*\Lambda(1116)$, and $K\Lambda(1520)$. In order to take into account the rescattering terms, we employed the Landau-Cutkosky rule in dealing with these box diagrams.

Since it turned out that the $K\Lambda^*(1520)$ box diagram played a dominant role among hadronic contributions in the lower-energy region, we scrutinized its contribution to ϕ photoproduction. We introduced the form factors depending on both the s and t Mandelstam variables in such a way that the total cross section of the $\gamma p \to K\Lambda^*(1520)$ reaction was well reproduced. All other box diagrams were constructed by utilizing the previous theoretical works and by reproducing the corresponding experimental data when they were available. We examined each contribution carefully by computing the differential cross section of ϕ photoproduction. While the $K\Lambda^*$ box diagram was found to be the most dominant near the 2 GeV, all other box diagrams turned out to be very small. The results were in good agreement with the LEPS data including the bump-like structure. We also computed the differential cross section as a function of $t+|t|_{\rm min}$ and found it to be in good agreement with the experimental data.

We investigated the contributions of hadronic box diagrams to the decay angular distributions. While the one-dimensional angular distributions $W(\cos\theta_K)$ and $W(\phi_K-\Phi)$ were in good agreement with the experimental data, other three angular distributions seemed to deviate from the LEPS experimental data. We also examined the various spin-density matrix elements, which were measured recently by the LEPS collaboration. We found that the hadronic box diagrams describe the experimental data for ${\rm Re}\rho^0_{10}$, ρ^0_{1-1} and ρ^1_{11} were well reproduced. While the present results explain near $t-|t|_{\rm min}\approx 0$ relatively well for other spin-density matrix elements, they deviated from the expeimental data as $t-|t|_{\rm min}\approx 0$ increased.

As shown in the present work, the intermediate box diagrams, in particular, the $K\Lambda^*(1520)$ one, play crucial roles in explaining the cross sections of the $\gamma p \to \phi p$ reaction in the vicinity of the threshold. Other box diagrams also provided certain effects on the part of the spin-density matrix elements. We have considered in this work only the imaginary part of the transition amplitudes of the box diagrams based on the Landau-Cutkosky rule. However, the results of the spin-density matrix elements already indicate that we should carry out a theoretical analysis of ϕ photoproduction more systematically and quantitatively. Thus, we need to investigate a full coupled-channel formalism and to solve rescattering equations with the real parts of the box diagrams fully taken into account. Another interesting and important problem is to extend our approach to the neutron target, since some of considered amplitudes are isospin-dependent. The corresponding works are under way.

8

$\gamma\, p \rightarrow K^+K^+\Xi^-$

8.1 Introduction

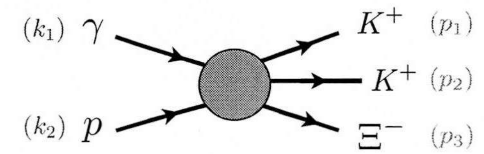

FIG. 8.1: $\gamma p \rightarrow K^+K^+\Xi^-$ scattering process.

Since the late 1980s, no significant progress has been made in cascade spectroscopy because of the closing of the then existing kaon facilities. Recenty, the CLAS Collaboration at the Tomas Jefferson National Accellerator Facility (JLab) initiated a cascade physics plan [16]. They want to understand the strangeness baryon properties more deeply via photoproduction reactions such as $\gamma p \rightarrow K^+K^+\Xi^-$ and $\gamma p \rightarrow K^+K^+\pi^-\Xi^0$.

Cascade physics has recently received special attention in connection with the search for the exotic pentaquark states. In fact, the NA49 Collaboration has reported seeing a signal for the pentaquark cascade Ξ_5^{--} [78]. However, to date, other experiments with much higher statistics have obtained negative results.

In this work, we investigate $\gamma p \rightarrow K^+K^+\Xi^-$ in an effective Lagrangian approach to estimate the cross section of that scattering process.

8.2 Possible diagrams (channels)

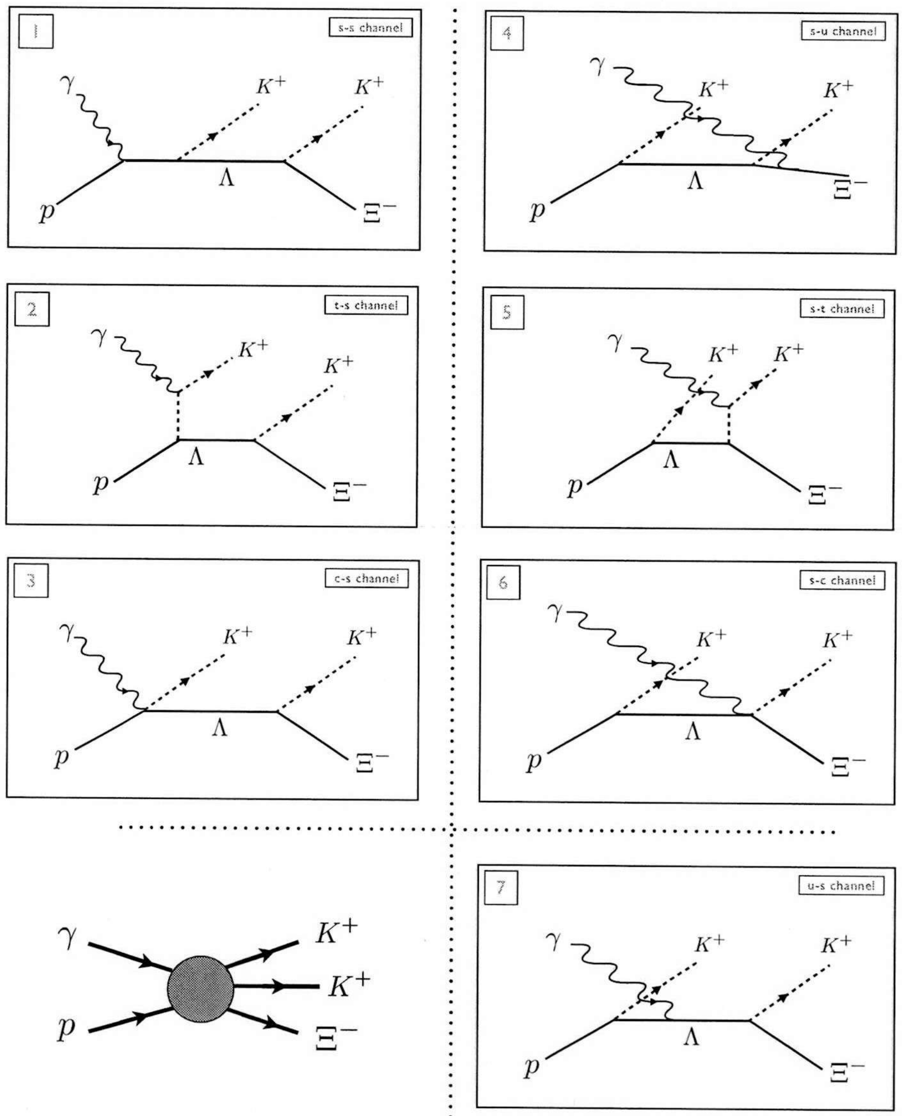

FIG. 8.2: 7 diagrams for $\gamma p \to K K \Xi^-$ scattering process.

FIG. 8.2 shows the seven possible diagrams for $\gamma p \to K K \Xi^-$ scattering process. Each diagram is determined by the position where the photon is coupled to. Since both kaons are charged, there are two diagrams (3 and 6) which contain the contact term. We found that diagram 1, 2 and 3 make gauge invariant set and diagram 4, 5 and 6 make another set. The diagram 7 is self-gauge invariant. We apply the different form factors for each gauge invariant set. We will explain this later.

8.3 Formalism

8.3.1 Effective Lagrangian

We use the following Lagrangian ;

$$\mathcal{L}_{\gamma NN} = -e\overline{N}\left[\gamma_\mu - \frac{\kappa_N}{2M_N}\sigma_{\mu\nu}\partial^\nu\right] NA^\mu \tag{8.1}$$

$$\mathcal{L}_{\gamma KK} = -ie\left[(\partial_\mu K^+)K^- - (\partial_\mu K^-)K^+\right] A^\mu \tag{8.2}$$

$$\mathcal{L}_{KN\Lambda} = g_{KN\Lambda}\,\bar{\Lambda}\gamma^\mu\gamma_5\partial_\mu K^- N \tag{8.3}$$

$$\mathcal{L}_{K\Lambda\Xi^-} = g_{K\Lambda\Xi^-}\,\overline{\Xi}^-\gamma^\mu\gamma_5\partial_\mu K^-\Lambda \tag{8.4}$$

$$\mathcal{L}_{\gamma KN\Lambda} = ieg_{\gamma KN\Lambda}\bar{\Lambda}\gamma^\mu\gamma_5 K^- NA^\mu \tag{8.5}$$

$$\mathcal{L}_{\gamma\Xi^-\Xi^-} = e\bar{\Xi}^-\left[\gamma_\mu + \frac{\kappa_\Xi}{2m_\Xi}\sigma_{\mu\nu}\partial^\nu\right]\Xi^- A^\mu \tag{8.6}$$

$$\mathcal{L}_{\gamma K\Lambda\Xi^-} = ieg_{\gamma K\Lambda\Xi^-}\bar{\Xi}^-\gamma^\mu\gamma_5 K^-\Lambda A^\mu \tag{8.7}$$

$$\mathcal{L}_{\gamma\Lambda\Lambda} = e\bar{\Lambda}\left[\frac{\kappa_\Lambda}{2m_\Lambda}\sigma_{\mu\nu}\partial^\nu\right]\Lambda A^\mu \tag{8.8}$$

We use the following coupling constants and anomalous magnetic moments:

$g_{KN\Lambda}$	6.1512 GeV^{-1}	Ref. [26]
$g_{K\Lambda\Xi^-}$	-2.104 GeV^{-1}	Ref. [24]
κ_p	1.79	Ref. [24]
κ_Λ	-0.613	Ref. [54]
κ_Ξ	0.35	Ref. [54]

Table 8.1: The strong coupling constants and anomalous magnetic moments used in the present work.

Until this step, there is no free parameter. We use the strong coupling constants and magnetic moments which are determined by previous experiments and theoretical calculations. Some free parameters will appear when we introduce form factors. And those free parameters will be determined by the experiment data later.

8.3.2 T-matrix

We use $S = 1 - iT$ convention and T-matrix are given by

$$
\begin{aligned}
T_1 &= -eg_1g_2\bar{u}(p_3)\not{p}_2\frac{\not{k}_1+\not{k}_2-\not{p}_1-M_\Lambda}{(k_1+k_2-p_1)^2-M_\Lambda^2}\not{p}_1\frac{\not{k}_1+\not{k}_2+M_p}{(k_1+k_2)^2-M_p^2}\not{\epsilon}_\gamma\left[I+\frac{\kappa_N}{2M_p}\not{k}_1\right]u(k_2)\,, && (8.9)\\
T_2 &= eg_1g_2\,\bar{u}(p_3)\not{p}_2\frac{\not{k}_1+\not{k}_2-\not{p}_1-M_\Lambda}{(k_1+k_2-p_1)^2-M_\Lambda^2}(\not{k}_1-\not{p}_1)u(k_2)\frac{2p_1\cdot\epsilon_\gamma}{(k_1-p_1)^2-m_K^2}\,, && (8.10)\\
T_3 &= eg_1g_2\bar{u}(p_3)\not{p}_2\frac{\not{k}_1+\not{k}_2-\not{p}_1-M_\Lambda}{(k_1+k_2-p_1)^2-M_\Lambda^2}\not{\epsilon}_\gamma u(k_2)\,, && (8.11)\\
T_4 &= eg_1g_2\bar{u}(p_3)\not{\epsilon}_\gamma\frac{\not{p}_3-\not{k}_1+M_\Xi}{(p_3-k_1)^2-M_\Xi^2}\not{p}_2\frac{\not{k}_2-\not{p}_1-M_\Lambda}{(k_2-p_1)^2-M_\Lambda^2}\not{p}_1u(k_2)\,, && (8.12)\\
T_5 &= eg_{K\Lambda\Xi}g_{Kp\Lambda}\,\bar{u}(p_3)(\not{k}_1-\not{p}_2)\frac{\not{k}_2-\not{p}_1-M_\Lambda}{(k_2-p_1)^2-M_\Lambda^2}\not{p}_1u(k_2)\frac{2p_2\cdot\epsilon_\gamma}{(k_1-p_2)^2-m_K^2}\,, && (8.13)\\
T_6 &= eg_1g_2\bar{u}(p_3)\not{\epsilon}_\gamma\frac{\not{k}_2-\not{p}_1-M_\Lambda}{(k_2-p_1)^2-M_\Lambda^2}\not{p}_1u(k_2)\,, && (8.14)\\
T_7 &= -eg_1g_2\frac{\kappa_\Lambda}{4M_\Lambda}\bar{u}(p_3)\not{p}_2\frac{\not{p}_2+\not{p}_3-M_\Lambda}{(p_2+p_3)^2-M_\Lambda^2}(\not{\epsilon}_\gamma\not{k}_1-\not{k}_1\not{\epsilon}_\gamma)\frac{\not{k}_2-\not{p}_1-M_\Lambda}{(k_2-p_1)^2-M_\Lambda^2}\not{p}_1u(k_2) && (8.15)
\end{aligned}
$$

where $g_1 = g_{KN\Lambda}$ and $g_2 = g_{K\Lambda\Xi^-}$. Except the diagrams which include the contact term, every diagrams have two propagators. Now we are in a position to find the gauge invariant set to apply form facotor. To conserve the gauge invariance, we will apply the form factor to the self-gauge invariant part and the gauge invariant set respectively. The gauge invariant set means that the sum of the invariant amplitudes are gauge invariant but alone is not.

We can easily check that T_1, T_2 and T_3 are consist of one gague invariant set and T_4, T_5 and T_6 make another set. T_7 is self gauge invarinat set. We apply relevent form factors for each gauge invariant set as follows:

$$
T_{\text{total}} = T_1^{\text{inv}}F_1 + +(T_1^{\text{viol}} + T_2 + T_3)F_{1,c} + +(T_4 + T_5 + T_6)F_{2,c}. \qquad (8.16)
$$

T_{total} stands for the sum of each diagram's T-matrix. T_1^{inv} and T_1^{viol} are the self gauge invariant part and the gauge violating part of T-matrix of the diagram 1. F_1 is the form factor which depends on only the virual particle's momenta in diagram 1. $F_{1,c}$ and $F_{2,c}$ are the common form factors which depend on the variable of the gauge invariant set. We introduce the detail of how to construct form factor in Appendix C.

8.4 Numerical result

Before applying form factors, we check the bare contribution of each diagrams.

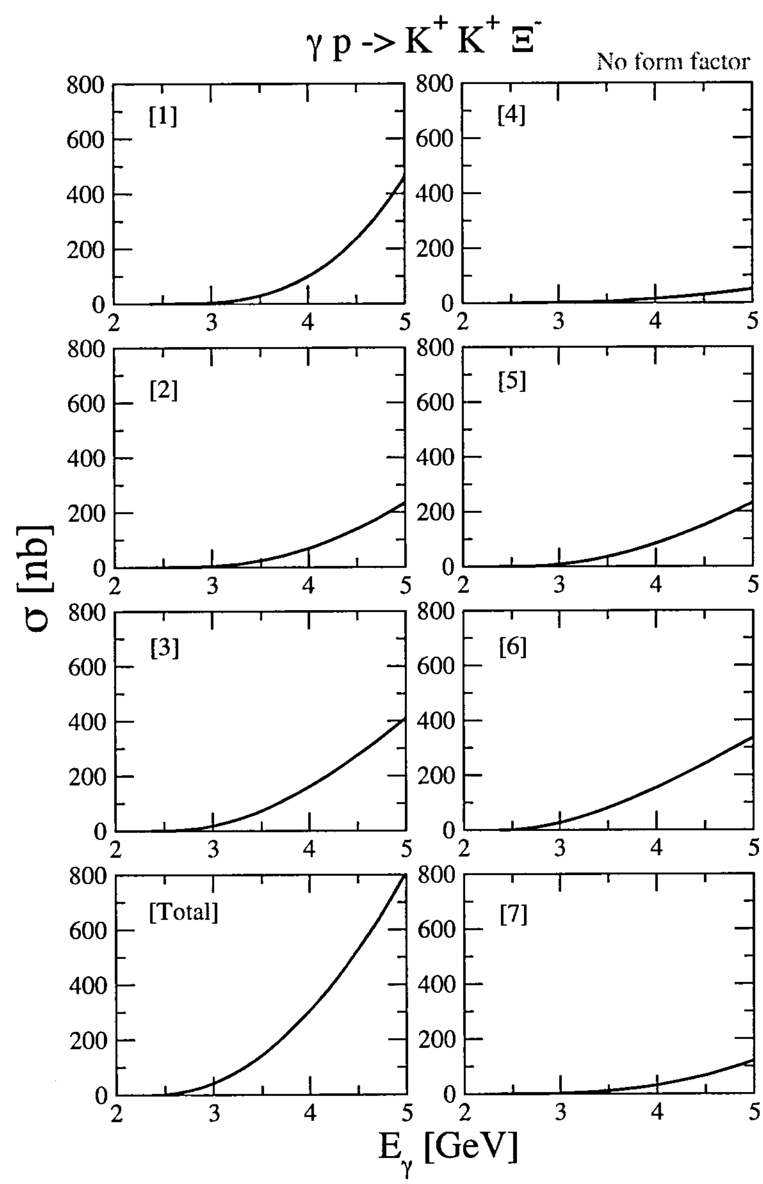

FIG. 8.3: total corss section without form factor

FIG. 8.3 tells us that the first diagram which contains s-channel is most dominant before applying the form factors. We can see that diagrams with photon coupled to the first kaon cotribute more than those with photon and the second kaon coupling. Diagram 2 and 4 contaions t-channel and 3 and 6 have contact term. Next let us consider form facotor contribution.

8.4.1 Type I form factor

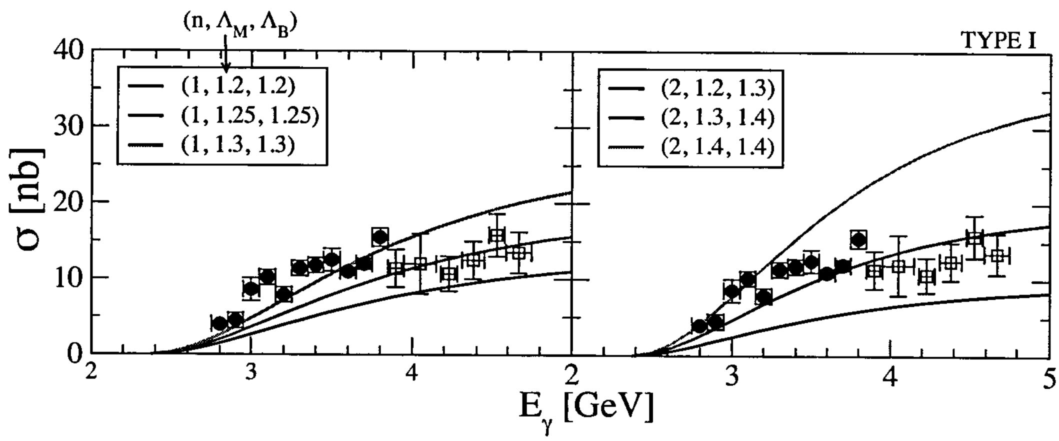

FIG. 8.4: Total corss section with type I form factor. Data are taken from [54].

FIG. 8.4 shows that our results with various parameters. We use type I form factor to reproduce the data and our best fitting is $(n, \Lambda_M, \Lambda_B) = (2, 1.3, 1.4)$. In the present work, we include only ground state baryons. Considering resonance baryons as intermediate states might change.

8.4.2 Type II form factor

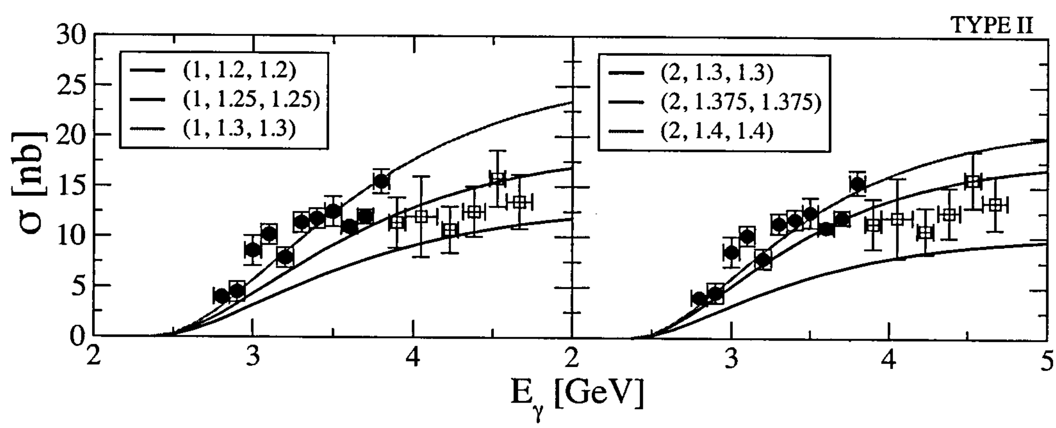

FIG. 8.5: Total corss section with type II form factor. Data are taken from [54].

FIG. 8.5 tells us that type II form factor can reproduce the data with the parameters which are similar values compared with those of the type I form factor. In this calculation, the best choice is $(n, \Lambda_M, \Lambda_B) = (2, 1.375, 1.375)$. This parameter sets can be used to estimate the order calculation of $\gamma p \to K^+K^+K^0\Omega^-$ by extrapolation.

8.5 Summary of this chapter

In summary, we have explored the reaction $\gamma p \rightarrow KK\Xi$ within an effective Lagrangian approach. This is the investigation of this reaction in connection with the cascade spectroscopy program initiated by the CALS Collaboration at JLab. There is a previous theoretical work [54], but we use a different form factor set to preserve the gauge invariance and consider the only ground states as the intermediate states. We found that with similar free parameters value compared with [54], we can reproduce the experiment data.

Our results show that our approach can reproduce the experimental data with reasonable choice of parameters. This calculation is important in the point of view that we can investigate the strangness physics via Ξ photoproduction. Also this calculation is helpful for us to estimate the three $s\bar{s}$ production which is related to Ω^- production. In the previous chapters, we introduced $\gamma p \rightarrow K\Lambda$ as one $s\bar{s}$ production process. This two $s\bar{s}$ production mechanism study, $KK\Xi$ production, is very important to extend three $s\bar{s}$ production process. We will use the results we get in this chapter to extimate $\gamma p \rightarrow KKK\Omega$ photoproduction. Furthermore we can investigate the dynamics of the cascade dynamics more using the machinary which we used in the present work.

Part IV

Three Kaons Photoproduction

9

$\gamma p \rightarrow \quad K^+K^+K^0\Omega^-$

9.1 Motivation

Historically, baryons with mulitple strange quarks have played an important role in the development of the quark model and our understanding of the universe. The prediction and discovery of the Ω baryon certainly was one of the great triumphs of the quark model. However, half a century later, there has been little new information about the Ω and Ξ byryons. In fact, only two Ω states and six Ξ states are considered to be well-established, with at least three-star rating in the PDG [14]. The production mechanism of these states is still unknown to a large extent. Tipically small cross sections make the observation of the higher excited states difficult, which explains our current lack of knowledge in excited hyperon spectroscopy. Production of doubley- or triply-strange baryons by means of a photon beam (such as in the CLAS, at present, and CLAS12 and GlueX, in the future) is expected to shed light on the genesis of these states which involves the production of $s\bar{s}$ pairs from the vacuum. This significant change in baryon strangeness number from intitial ($S = 0$) to final state ($S = -3, \ -2$) could result from direct production via vector-meson dominance or from a sequence of intermediate transitons. Inference on the production mechanism of these states in γp collisions can be obtained from precision measurements of the cross section and invariant mass of these states.

The photoproduction of the ($S = -3$) Ω baryon requires the total strangeness transfer $\Delta S = 3$. This is the largest possible transfer of strangeness number, which makes the measurement of the production of this state and of its decay properties particularly interesting in a photoproduction environment, which have not yet been established.

The 12 GeV upgrade in CLAS12 will provide and order of magnitude higher in luminosity and significantly better multiple-particle final states acceptance than CLAS. It is therefore expected that many aspects of Ω^- and Ξ stats, including the cross section of the ground state Ω^- and Ξ baryons, the mass splittings of ground and excited cascades which would deepen our understanding of the u/d quark mass difference, and the polarization of the Ξ^- baryon.

In this chapter, we calculate the cross section for $\gamma p \to K^+K^+K^0\Omega^-$ based on an effective Lagrangian approach. The ground states Λ, Σ and Ξ are included in this calculation. With the form factor set used in one and two kaons photoproduction, we estimate an order of the total cross section.

9.2 Three type of diagrams

9.2.1 Type I, II and III

Here I would like to explain how to construct the diagrams we consider. At fisrt draw the baryon and meson lines. After that we can draw photon line which is coupled to the charged particle and the particle with the magnetic moment.

Considering the order of three kaon, I have the diagram set which depends on the position of the neutral kaon. Each diagram set is labeled as type I, type II and type III. FIG. 9.1 show the type I diagram which the neutral kaon is third position.

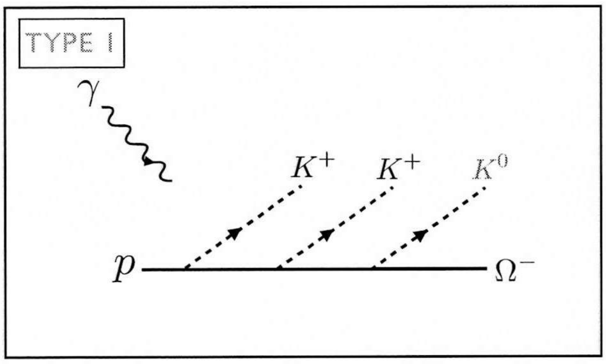

FIG. 9.1: The first type of diagram set. It depends on the position of the neutral kaon.

We couple the photon line to the charged kaons and each baryons. Since we cannot attach the photon line to the neutral kaon, there is no t-channel and contact term related to the neural kaon, K^0. I would like to introduce other two type. After that I will explain how to draw the photon line.

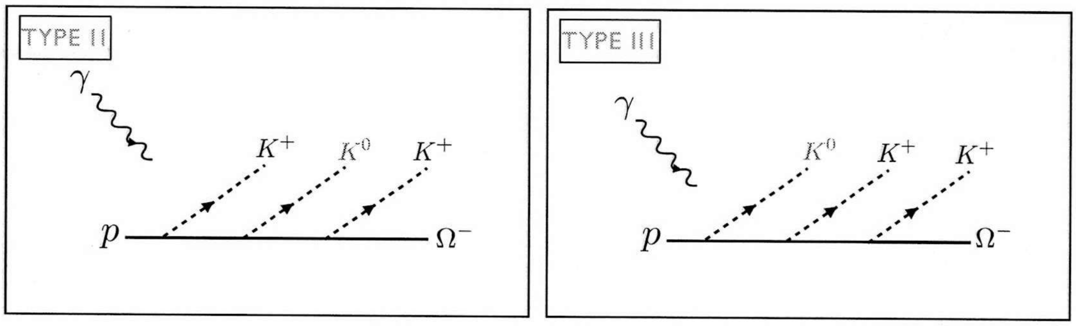

FIG. 9.2: The second and third diagram set.

After we categorize three types, we need to distinguish the diagrams according to the place where photon coupling.

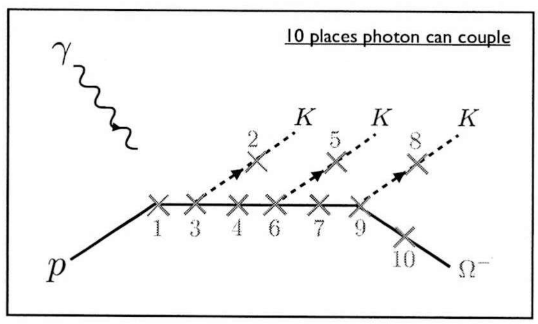

FIG. 9.3: 10 possible places where photon can couple to.

I show 10 possiblities that the photon can couple with, but it depends on the charge of kaon. It means that the photon cannot couple with nuetural kaon, therefore there are 8 possibilites for each type. But I will fix the label of the 10 places. For example, photon doesn't couple with positon 8 and 9 for the type I case. I call the diagram I-7 for the diagram which photon couple with position 7 and call the diagram I-10 for the diagram coupled with position 10 even though there are no photon coupling with position 8 and 9 in the case of type I.

We will show each diagram when we explain the detail formalism in the next section. In the present work, we include the kaon and the ground state of baryons , for example $\Lambda(1116)$ and $Xi^{-}(1321)$. We can improve our result including more intermediate states. That is our next work.

9.3 Formalism : Type I diagrams

8 diagrams of type I are shown. The neutral kaon is the third line which is denoted in a red. In this present work we consider the ground state baryons as intermediate particles. For example, $B_1 = p$, $B_2 = \Lambda$ and $B_3 = \Xi^-$. Furthermore we consider the kaon t-channel exchange in the 2nd and the 5th diagrams.

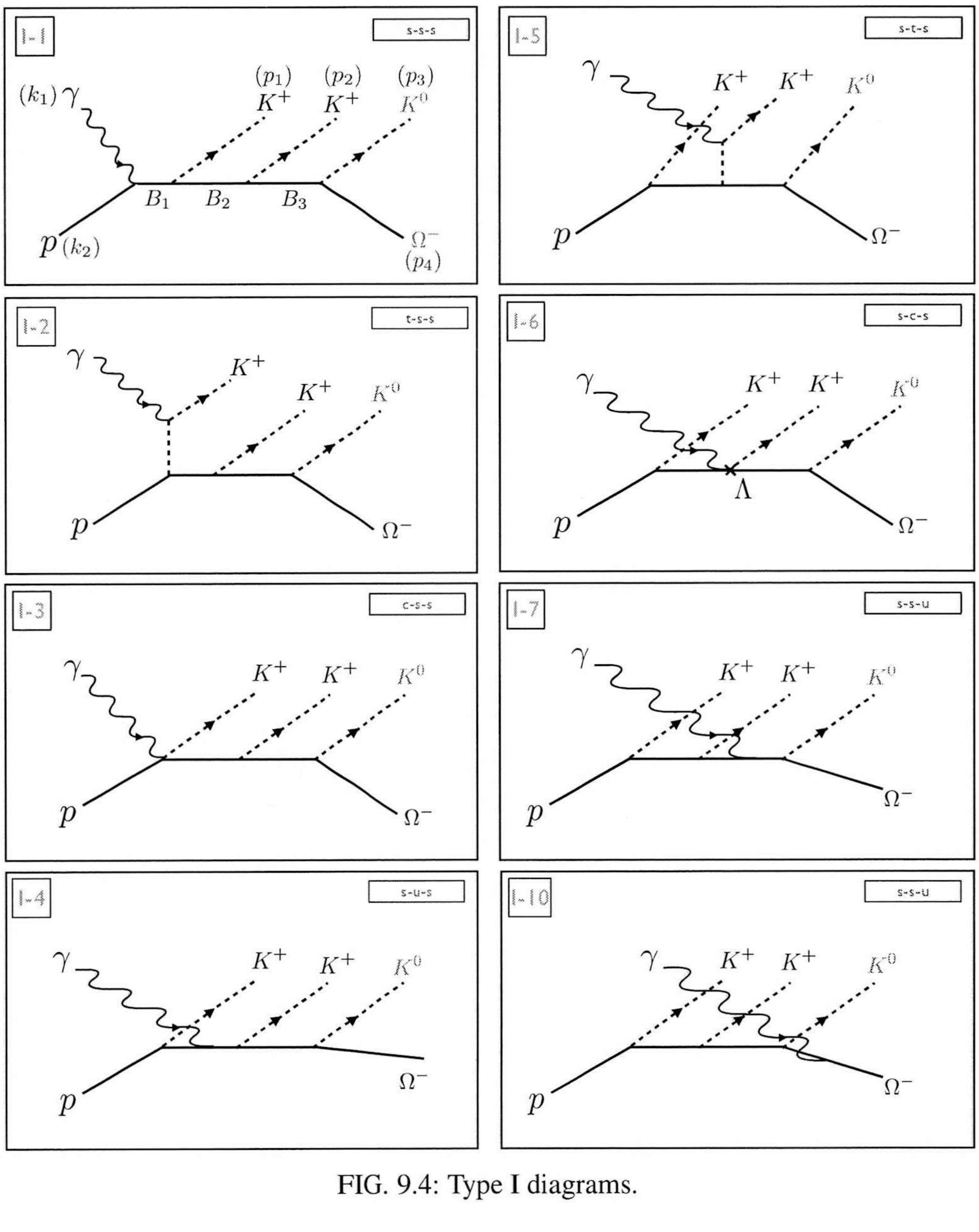

FIG. 9.4: Type I diagrams.

In the next, we will introduce Lagrangian set and T-matrices to calculate this diagrams.

9.3.1 Effective Lagrangian and T-matrix

Effective Lagrangians are given by

$$\mathcal{L}_{\gamma NN} = -e\overline{N}\left[\gamma_\mu - \frac{\kappa_N}{2M_N}\sigma_{\mu\nu}\partial^\nu\right]A^\mu N \tag{9.1}$$

$$\mathcal{L}_{\gamma KK} = -ie\left[(\partial K^+)K^- - \partial(K^-)K^+\right] \tag{9.2}$$

$$\mathcal{L}_{KN\Lambda} = g_{K^+N\Lambda}\overline{\Lambda}\gamma^\mu\gamma_5\partial_\mu K^- N \tag{9.3}$$

$$\mathcal{L}_{K\Lambda\Xi^-} = g_{K^+\Lambda\Xi^-}\overline{\Xi}^-\gamma^\mu\gamma_5\partial_\mu\overline{K}^-\Lambda \tag{9.4}$$

$$\mathcal{L}_{K^0\Xi^-\Omega^-} = g_{K^0\Xi^-\Omega^-}\overline{\Omega}^{-\mu}\partial_\mu\overline{K}^0\gamma_5\Xi^- \tag{9.5}$$

For convention, I define couplings for short as follows:

$$g_1 = g_{KN\Lambda}\,, \quad g_2 = g_{K\Lambda\Xi^-}\,, \quad g_3 = g_{K^0\Xi^-\Omega^-} \tag{9.6}$$

where $\Lambda = \Lambda(1116)$. T-matrixces are given by

$$\begin{aligned} T_{\mathrm{I}-1} &= -ieg_1g_2g_3\overline{u}^\mu(p_4)p_3^\mu\frac{\not{k}_1+\not{k}_2-\not{p}_1-\not{p}_2-M_{\Xi^-}}{(k_1+k_2-p_1-p_2)^2-M_{\Xi^-}^2}\not{p}_2\frac{\not{k}_1+\not{k}_2-\not{p}_1+M_\Lambda}{(k_1+k_2-p_1)^2-M_\Lambda^2} \\ &\times\not{p}_1\gamma_5\frac{\not{k}_1+\not{k}_2+M_p}{(k_1+k_2)^2-M_p^2}\left[I+\frac{\kappa_p}{2M_p}\not{k}_1\right]\not{\epsilon}_\gamma u(k_2) \end{aligned} \tag{9.7}$$

$$\begin{aligned} T_{\mathrm{I}-2} &= ieg_1g_2g_3\overline{u}^\mu(p_4)p_3^\mu\frac{\not{k}_1+\not{k}_2-\not{p}_1-\not{p}_2-M_{\Xi^-}}{(k_1+k_2-p_1-p_2)^2-M_{\Xi^-}^2}\not{p}_2\frac{\not{k}_1+\not{k}_2-\not{p}_1+M_\Lambda}{(k_1+k_2-p_1)^2-M_\Lambda^2} \\ &\times(\not{k}_1-\not{p}_1)\gamma_5u(k_2)\times\frac{2p_1\cdot\epsilon_\gamma}{(k_1-p_1)^2-m_K^2} \end{aligned} \tag{9.8}$$

$$\begin{aligned} T_{\mathrm{I}-3} &= ieg_1g_2g_3\overline{u}^\mu(p_4)p_3^\mu\frac{\not{k}_1+\not{k}_2-\not{p}_1-\not{p}_2-M_{\Xi^-}}{(k_1+k_2-p_1-p_2)^2-M_{\Xi^-}^2}\not{p}_2\frac{\not{k}_1+\not{k}_2-\not{p}_1+M_\Lambda}{(k_1+k_2-p_1)^2-M_\Lambda^2} \\ &\times\not{\epsilon}_\gamma\gamma_5u(k_2) \end{aligned} \tag{9.9}$$

$$
\begin{aligned}
T_{\mathrm{I}-4} &= -ieg_1g_2g_3\frac{\kappa_\Lambda}{2M_\Lambda}\overline{u}^\mu(p_4)p_3^\mu\frac{\not{k}_1+\not{k}_2-\not{p}_1-\not{p}_2-M_{\Xi^-}}{(k_1+k_2-p_1-p_2)^2-M_{\Xi^-}^2} \\
&\times\not{p}_2\frac{\not{k}_1+\not{k}_2-\not{p}_1+M_\Lambda}{(k_1+k_2-p_1)^2-M_\Lambda^2}\not{k}_1\not{\epsilon}_\gamma\frac{\not{k}_2-\not{p}_1+M_\Lambda}{(k_2-p_1)^2-M_\Lambda^2}\not{p}_1\gamma_5u(k_2) \qquad (9.10)
\end{aligned}
$$

$$
\begin{aligned}
T_{\mathrm{I}-5} &= -ieg_1g_2g_3\overline{u}^\mu(p_4)p_3^\mu\frac{\not{k}_1+\not{k}_2-\not{p}_1-\not{p}_2-M_{\Xi^-}}{(k_1+k_2-p_1-p_2)^2-M_{\Xi^-}^2} \\
&\times\not{p}_2\frac{\not{k}_2-\not{p}_1+M_\Lambda}{(k_2-p_1)^2-M_\Lambda^2}\times\not{p}_1\gamma_5u(k_2)\frac{2p_2\cdot\epsilon_\gamma}{(k_1-p_2)^2-m_K^2} \qquad (9.11)
\end{aligned}
$$

$$
\begin{aligned}
T_{\mathrm{I}-6} &= -ieg_1g_2g_3\overline{u}^\mu(p_4)p_3^\mu\frac{\not{k}_1+\not{k}_2-\not{p}_1-\not{p}_2-M_{\Xi^-}}{(k_1+k_2-p_1-p_2)^2-M_{\Xi^-}^2} \\
&\times\not{\epsilon}_\gamma\frac{\not{k}_2-\not{p}_1+M_\Lambda}{(k_2-p_1)^2-M_\Lambda^2}\not{p}_1\gamma_5u(k_2) \qquad (9.12)
\end{aligned}
$$

$$
\begin{aligned}
T_{\mathrm{I}-7} &= ieg_1g_2g_3\overline{u}^\mu(p_4)p_3^\mu\frac{\not{k}_1+\not{k}_2-\not{p}_1-\not{p}_2-M_{\Xi^-}}{(k_1+k_2-p_1-p_2)^2-M_{\Xi^-}^2}\left[I+\frac{\kappa_{\Xi^-}}{2M_{\Xi^-}}\not{k}_1\right] \\
&\times\not{\epsilon}_\gamma\frac{\not{k}_2-\not{p}_1-\not{p}_2-M_{\Xi^-}}{(k_2-p_1-p_2)^2-M_{\Xi^-}^2}\not{p}_1\gamma_5u(k_2)u(k_2) \qquad (9.13)
\end{aligned}
$$

$$
\begin{aligned}
T_{\mathrm{I}-10} &= ieg_1g_2g_3\left[\overline{u}^\mu(p_4)\left\{\gamma_\alpha g_{\mu\nu}-\frac{1}{2}(\gamma_\alpha\gamma_\mu\gamma_\nu+\gamma_\mu\gamma_\nu\gamma_\alpha)\right\}\epsilon_\gamma^\alpha D^{\nu\beta}(k_2-p_1-p_3)\right. \\
&\left.-\frac{\kappa_\Omega}{2M_\Omega}\overline{u}^\mu(p_4)\not{k}_1\not{\epsilon}_\gamma D_\mu^\beta(k_2-p_1-p_3)\right] \\
&\times p_{3\beta}\frac{\not{k}_2-\not{p}_1-\not{p}_2-M_{\Xi^-}}{(k_2-p_1-p_2)^2-M_{\Xi^-}^2}\not{p}_2\frac{\not{k}_2-\not{p}_1+M_\Lambda}{(k_2-p_1)^2-M_\Lambda^2}\not{p}_1\gamma_5u(k_2) \qquad (9.14)
\end{aligned}
$$

where the propagator of the spin3/2 spinor is defined as

$$
D^{\mu\nu}(p)=\frac{\not{p}+M}{p^2-M^2}\left[g^{\mu\nu}-\frac{1}{3}\gamma^\mu\gamma^\nu-\frac{2}{3}\frac{p^\mu p^\nu}{M^2}-\frac{p^\mu\gamma^\nu-p^\nu\gamma^\mu}{3M}\right] \qquad (9.15)
$$

9.4 Formalism : Type II diagrams

8 diagrams of type II are shown. The nuetral kaon is the second line which is denoted in a red.

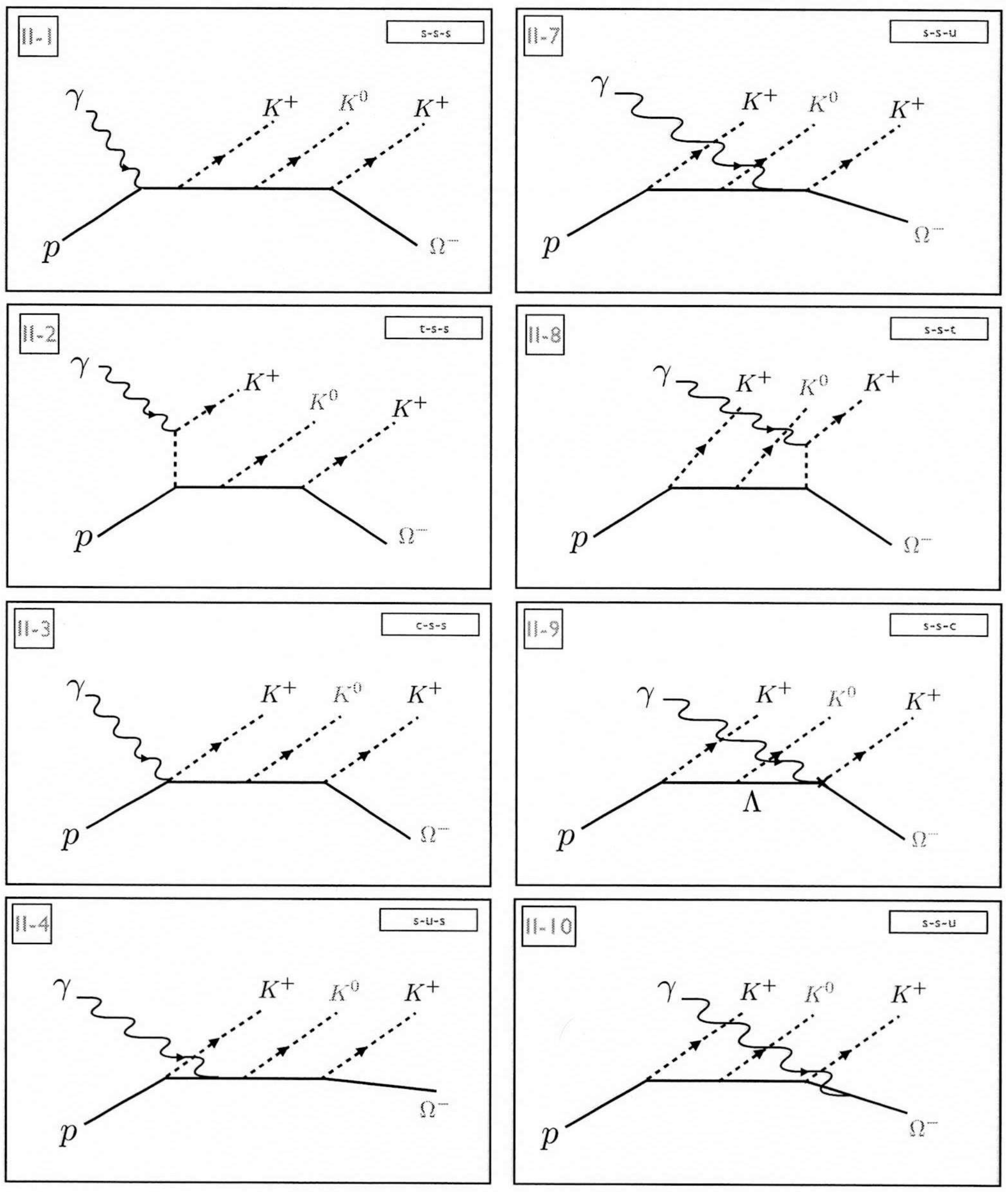

FIG. 9.5: Type II 8 diagrams.

Becareful that the label number is not order of diagrams, but the position where the photon line is coupled to. And there is no contac term related to the neural kaon.

9.4.1 Effective Lagrangian and T-matrix

Effective Lagrangians are given by

$$\mathcal{L}_{\gamma NN} = -e\overline{N}\left[\gamma_\mu + -\frac{\kappa_N}{2M_N}\partial^\nu\right]A^\mu N \tag{9.16}$$

$$\mathcal{L}_{KN\Lambda} = g_{K^+N\Lambda}\overline{\Lambda}\gamma^\mu\gamma_5\partial_\mu K^- N \tag{9.17}$$

$$\mathcal{L}_{K^0\Lambda\Xi^0} = g_{K^0\Lambda\Xi^0}\overline{\Xi}^0\gamma^\mu\gamma_5\partial_\mu\overline{K}^0\Lambda \tag{9.18}$$

$$\mathcal{L}_{K^+\Xi^0\Omega^-} = g_{K^-\Xi^0\Omega^-}\overline{\Xi}^0\gamma_5\partial_\mu\overline{K}^0\Omega^{-\mu} + g_{K^+\Lambda\Xi^0}\overline{\Omega}^{-\mu}\partial_\mu\overline{K}^0\gamma_5\Xi^- \tag{9.19}$$

For convention, I define couplings for short as follows:

$$g_1 = g_{KN\Lambda}\,, \quad g_4 = g_{K^0\Lambda\Xi^0}\,, \quad g_5 = g_{K\Xi^0\Omega^-} \tag{9.20}$$

T-matrixces are given by

$$\begin{aligned} T_{\text{II}-1} &= -ieg_1g_4g_5\overline{u}^\alpha(p_4)p_{3\alpha}\frac{\not{k}_1+\not{k}_2-\not{p}_1-\not{p}_2-M_{\Xi^0}}{(k_1+k_2-p_1-p_2)^2-M_{\Xi^0}^2}\not{p}_2\frac{\not{k}_1+\not{k}_2-\not{p}_1-M_\Lambda}{(k_1+k_2-p_1)^2-M_\Lambda^2}\not{p}_1\gamma_5 \\ &\times\frac{\not{k}_1+\not{k}_2-M_p}{(k_1+k_2)^2-M_p^2}\left[I+\frac{\kappa_p}{2M_p}\not{k}_1\right]\not{\epsilon}_\gamma u(k_2) \end{aligned} \tag{9.21}$$

$$\begin{aligned} T_{\text{II}-2} &= ieg_1g_4g_5\overline{u}^\alpha(p_4)p_{3\alpha}\frac{\not{k}_1+\not{k}_2-\not{p}_1-\not{p}_2-M_{\Xi^0}}{(k_1+k_2-p_1-p_2)^2-M_{\Xi^0}^2}\not{p}_2\frac{\not{k}_1+\not{k}_2-\not{p}_1-M_\Lambda}{(k_1+k_2-p_1)^2-M_\Lambda^2} \\ &\times(\not{k}_1-\not{p}_1)\gamma_5u(k_2)\times\frac{2p_1\cdot\epsilon_\gamma}{(k_1-p_1)^2-m_K^2} \end{aligned} \tag{9.22}$$

$$\begin{aligned} T_{\text{II}-3} &= -ieg_1g_4g_5\overline{u}^\alpha(p_4)p_{3\alpha}\frac{\not{k}_1+\not{k}_2-\not{p}_1-\not{p}_2-M_{\Xi^0}}{(k_1+k_2-p_1-p_2)^2-M_{\Xi^0}^2}\not{p}_2\frac{\not{k}_1+\not{k}_2-\not{p}_1+M_\Lambda}{(k_1+k_2-p_1)^2-M_\Lambda^2} \\ &\times\not{\epsilon}_\gamma\gamma_5u(k_2) \end{aligned} \tag{9.23}$$

$$\begin{aligned} T_{\text{II}-4} &= -ieg_1g_4g_5\frac{\kappa_\Lambda}{2M_\Lambda}\overline{u}^\mu(p_4)p_3^\mu\frac{\not{k}_1+\not{k}_2-\not{p}_1-\not{p}_2-M_{\Xi^-}}{(k_1+k_2-p_1-p_2)^2-M_{\Xi^-}^2} \\ &\times\not{p}_2\frac{\not{k}_1+\not{k}_2-\not{p}_1+M_\Lambda}{(k_1+k_2-p_1)^2-M_\Lambda^2}\not{k}_1\not{\epsilon}_\gamma\frac{\not{k}_2-\not{p}_1+M_\Lambda}{(k_2-p_1)^2-M_\Lambda^2}\not{p}_1\gamma_5u(k_2) \end{aligned} \tag{9.24}$$

$$T_{\text{II}-7} = ieg_1g_4g_5\frac{\kappa_{\Xi^0}}{2M_{\Xi^0}}\bar{u}^\mu(p_4)p_3^\mu\frac{\not{k}_1+\not{k}_2-\not{p}_1-\not{p}_2-M_{\Xi^-}}{(k_1+k_2-p_1-p_2)^2-M_{\Xi^-}^2}$$
$$\times\not{k}_1\not{\epsilon}_\gamma\frac{\not{k}_1+\not{k}_2-\not{p}_1-M_\Lambda}{(k_1+k_2-p_1)^2-M_\Lambda^2}\not{p}_2\frac{\not{k}_2-\not{p}_1+M_\Lambda}{(k_2-p_1)^2-M_\Lambda^2}\not{p}_1\gamma_5u(k_2) \quad (9.25)$$

$$T_{\text{II}-8} = ieg_1g_4g_5\bar{u}^\alpha(p_4)p_{3\alpha}\frac{\not{k}_2-\not{p}_1-\not{p}_2-M_{\Xi^0}}{(k_2-p_1-p_2)^2-M_{\Xi^0}^2}\not{p}_2\frac{\not{k}_2-\not{p}_1+M_\Lambda}{(k_2-p_1)^2-M_\Lambda^2}$$
$$\times\not{p}_1\gamma_5u(k_2)\times\frac{2p_3\cdot\epsilon_\gamma}{(k_1-p_3)^2-m_K^2} \quad (9.26)$$

$$T_{\text{II}-9} = ieg_1g_4g_5\bar{u}^\alpha(p_4)\epsilon_{\gamma\alpha}\frac{\not{k}_2-\not{p}_1-\not{p}_2-M_{\Xi^0}}{(k_2-p_1-p_2)^2-M_{\Xi^0}^2}\not{p}_2\frac{\not{k}_2-\not{p}_1+M_\Lambda}{(k_2-p_1)^2-M_\Lambda^2}$$
$$\times\not{p}_1\gamma_5u(k_2) \quad (9.27)$$

$$T_{\text{II}-10} = ieg_1g_4g_5\Big[\bar{u}^\alpha\Big\{\gamma_\alpha g_{\mu\nu}-\frac{1}{2}(\gamma_\alpha\gamma_\mu\gamma_\nu+\gamma_\mu\gamma_\nu\gamma_\alpha)\Big\}\epsilon_\gamma^\alpha D^{\nu\beta}(k_2-p_1-p_2-p_3)$$
$$-\bar{u}^\mu(p_4)\frac{\kappa_\Omega}{2M_\Omega}\not{k}_1\not{\epsilon}_\gamma D^{\mu\beta}(k_2-p_1-p_2-p_3)\Big]p_{3\beta}\frac{\not{k}_2-\not{p}_1-\not{p}_2-M_\Xi}{(k_2-p_1-p_2)^2-M_\Xi^2}\not{p}_2$$
$$\times\frac{\not{k}_2-\not{p}_1+M_\Lambda}{(k_2-p_1)^2-M_\Lambda^2}\not{p}_1\gamma_5u(k_2). \quad (9.28)$$

T-matrices for type II have three propagators except the diagrams which contain the contact term. We can easily show that the first 3 T-matrices are gauge invariant set. But others are not so trivial. Therefore, in the preliminary result, we check the gauge invariance of $T_{\text{II}-4-\text{II}-10}$ numerically. After that we apply the form factors to the first 3 T-matrices and to the others respectively.

9.5 Formalism : Type III diagrams

Here we will show the 8 diagrams in type III. And we will explain which lagrangians are used and T-matrix expression.

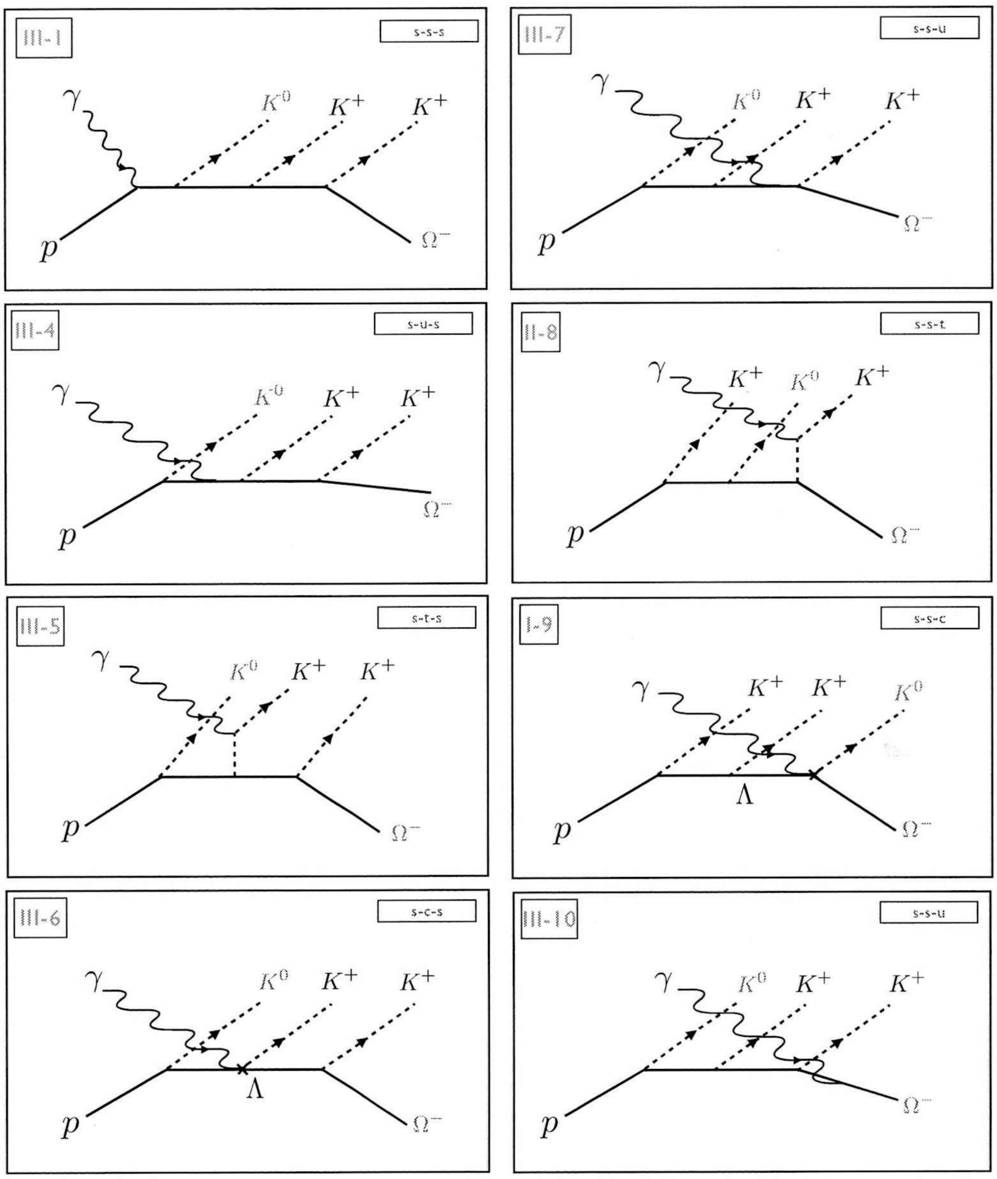

FIG. 9.6: 8 diagrams of Type III

Type III diagrams have different intermediate states because of the order of the neutral kaon. In this case, ground state Σ^+ and Ξ^0 are choosen as the vitual intemediate states.

9.5.1 Effective Lagrangian and T-matrix

Effective Lagrangians for type III are given by

$$\mathcal{L}_{\gamma NN} = -e\overline{N}\left[\gamma^{\mu} - \frac{\kappa_N}{2M_N}\sigma^{\mu\nu}\partial_{\nu}\right]A_{\mu}N \tag{9.29}$$

$$\mathcal{L}_{\gamma KK} = -ie\left[(\partial^{\mu}K)\overline{K} - (\partial^{\mu}\overline{K})K\right]A_{\mu} \tag{9.30}$$

$$\mathcal{L}_{KN\Sigma^0} = g_{KN\Sigma^0}\overline{\Sigma}^{+}\gamma^{\mu}\gamma_5\partial_{\alpha}N \tag{9.31}$$

$$\mathcal{L}_{K\Sigma^+\Xi^0} = g_{K\Sigma^+\Xi^0}\overline{\Xi}^{0}\gamma^{\mu}\gamma_5\partial_{\mu}K^{-}\Sigma^{+} \tag{9.32}$$

$$\mathcal{L}_{\gamma K\Sigma^+\Xi^0} = ieg_{\gamma K\Sigma^+\Xi^0}\overline{\Xi}^{0}\gamma^{\mu}\gamma_5\Sigma^{+}A_{\mu}K^{-} \tag{9.33}$$

$$\mathcal{L}_{K\Xi^0\Omega^-} = g_{K\Xi^0\Omega^-}\overline{\Omega}^{-\mu}\partial_{\mu}K^{+}\gamma_5\Xi^{0} \tag{9.34}$$

$$\mathcal{L}_{\gamma K\Xi^0\Omega^-} = -ieg_{\gamma K\Xi^0\Omega^-}\overline{\Omega}^{-\mu}A_{\mu}K^{+}\gamma_5\Xi^{0} \tag{9.35}$$

$$\mathcal{L}_{\gamma\Sigma^+\Sigma^+} = -e\overline{\Sigma}^{+}\left[\gamma^{\mu} - \frac{\kappa_{\Sigma}}{2M_{\Sigma}}\right]A_{\mu}\Sigma^{+} \tag{9.36}$$

$$\mathcal{L}_{\gamma\Xi^0\Xi^0} = e\overline{\Xi}^{0}\frac{\kappa_{\Xi}}{2M_{\Xi^0}}\sigma^{\mu\nu}\partial_{\nu}A_{\mu}\Xi^{0} \tag{9.37}$$

$$\begin{aligned}\mathcal{L}_{\gamma\Omega^-\Omega^-} &= -e\overline{\Omega}^{-\mu}\left[\gamma_{\alpha}g_{\mu\nu} - \frac{1}{2}(\gamma_{\alpha}\gamma_{\mu}\gamma_{\nu} + \gamma_{\mu}\gamma_{\nu}\gamma_{\alpha})\right]A^{\alpha}\Omega^{-\nu} \\ &\quad -e\overline{\Omega}^{-\mu}\frac{\kappa_{\Omega^-}}{2M_{\Omega^-}}\sigma^{\alpha\nu}(\partial_{\nu}A_{\alpha})\Omega^{-}_{\mu}.\end{aligned} \tag{9.38}$$

For convenience, we redefine the coupling constants as follows:

$$g_6 = g_{K\Xi^0\Omega^-} \tag{9.39}$$

$$g_7 = g_{KN\Sigma^0} \tag{9.40}$$

$$g_8 = g_{K\Sigma^+\Xi^0} \tag{9.41}$$

g_6 and g_7 are determined from previous works. But in our calculation, g_8 which is related to Ω^- is a free parameter. We choose 10 as the coupling constants related to Ω^- verteces in the present work.

T-matrixces of type III are given by

$$T_{\text{III}-1} = -ieg_6g_7g_8\overline{u}^{\mu}(p_4)p_{3\mu}\frac{\not{k}_1+\not{k}_2-\not{p}_1-\not{p}_2-M_{\Xi^0}}{(k_1+k_2-p_1-p_2)^2-M_{\Xi^0}^2}\not{p}_2\frac{\not{k}_1+\not{k}_2-\not{p}_1+M_{\Sigma^+}}{(k_1+k_2-p_1)^2-M_{\Sigma^+}^2}\not{p}_1\gamma_5 \times\frac{\not{k}_1+\not{k}_2+M_p}{(k_1+k_2)^2-M_p^2}\left[I+\frac{\kappa_p}{2M_p}\not{k}_1\right]\not{\epsilon}_\gamma u(k_2) \quad (9.42)$$

$$T_{\text{III}-4} = -ieg_6g_7g_8\overline{u}^{\mu}(p_4)p_{3\mu}\frac{\not{k}_1+\not{k}_2-\not{p}_1-\not{p}_2-M_{\Xi^0}}{(k_1+k_2-p_1-p_2)^2-M_{\Xi^0}^2}\not{p}_2\frac{\not{k}_1+\not{k}_2-\not{p}_1+M_{\Sigma^+}}{(k_1+k_2-p_1)^2-M_{\Sigma^+}^2} \times\left[I+\frac{\kappa_\Sigma}{2M_\Sigma}\not{k}_1\right]\not{\epsilon}_\gamma\frac{\not{k}_2-\not{p}_1+M_{\Sigma^+}}{(k_2-p_1)^2-M_{\Sigma^+}^2}\not{p}_1\gamma_5 u(k_2) \quad (9.43)$$

$$T_{\text{III}-5} = ieg_6g_7g_8\overline{u}^{\mu}(p_4)p_{3\mu}\frac{\not{k}_1+\not{k}_2-\not{p}_1-\not{p}_2-M_{\Xi^0}}{(k_1+k_2-p_1-p_2)^2-M_{\Xi^0}^2}(\not{k}_1-\not{p}_2)\frac{\not{k}_2-\not{p}_1+M_{\Sigma^+}}{(k_2-p_1)^2-M_{\Sigma^+}^2} \times\not{p}_1\gamma_5 u(k_2)\frac{2p_2\cdot\epsilon_\gamma}{(k_1-p_2)^2-m_K^2} \quad (9.44)$$

$$T_{\text{III}-6} = -ieg_6g_7g_8\overline{u}^{\mu}(p_4)p_{3\mu}\frac{\not{k}_1+\not{k}_2-\not{p}_1-\not{p}_2-M_{\Xi^0}}{(k_1+k_2-p_1-p_2)^2-M_{\Xi^0}^2}\not{\epsilon}_\gamma\frac{\not{k}_2-\not{p}_1+M_{\Sigma^+}}{(k_2-p_1)^2-M_{\Sigma^+}^2} \times\not{p}_1\gamma_5 u(k_2) \quad (9.45)$$

$$T_{\text{III}-7} = ieg_6g_7g_8\overline{u}^{\mu}(p_4)p_{3\mu}\frac{\not{k}_1+\not{k}_2-\not{p}_1-\not{p}_2-M_{\Xi^0}}{(k_1+k_2-p_1-p_2)^2-M_{\Xi^0}^2}\not{k}_1\not{\epsilon}_\gamma\frac{\kappa_\Xi}{2M_\Xi}\frac{\not{k}_2-\not{p}_1-\not{p}_2-M_{\Xi^0}}{(k_2-p_1-p_2)^2-M_{\Xi^0}^2}\not{p}_2 \times\frac{\not{k}_2-\not{p}_1-M_{\Sigma^+}}{(k_2-p_1)^2-M_{\Sigma^+}^2}\not{p}_1\gamma_5 u(k_2) \quad (9.46)$$

$$T_{\text{III}-8} = ieg_6g_7g_8\overline{u}^{\mu}(p_4)p_{3\mu}\frac{\not{k}_2-\not{p}_1-\not{p}_2-M_{\Xi^0}}{(k_2-p_1-p_2)^2-M_{\Xi^0}^2}\not{p}_2\frac{\not{k}_2-\not{p}_1+M_{\Sigma^+}}{(k_2-p_1)^2-M_{\Sigma^+}^2} \times\not{p}_1\gamma_5 u(k_2)\frac{2p_3\cdot\epsilon_\gamma}{(k_1-p_3)^2-m_K^2} \quad (9.47)$$

$$T_{\text{III}-9} = ieg_6g_7g_8\overline{u}^{\mu}(p_4)\epsilon_{\gamma\mu}\frac{\not{k}_2-\not{p}_1-\not{p}_2-M_{\Xi^0}}{(k_2-p_1-p_2)^2-M_{\Xi^0}^2}\not{p}_2\frac{\not{k}_2-\not{p}_1+M_{\Sigma^+}}{(k_2-p_1)^2-M_{\Sigma^+}^2}\not{p}_1\gamma_5 u(k_2) \quad (9.48)$$

$$T_{\text{III}-10} = ieg_6g_7g_8\overline{u}^{\mu}(p_4)\left[\gamma_\alpha\left\{g_{\mu\nu}-\frac{1}{2}(\gamma_\mu\gamma_\nu+\gamma_\nu\gamma_\mu)\right\}\epsilon^{\gamma\alpha}D^{\nu\beta}(k_2-p_1-p_2-p_3) -\frac{\kappa_\Omega}{2M_\Omega}\not{\epsilon}_\gamma\not{k}_1 D^{\mu\beta}(k_2-p_1-p_2-p_3)\right]p_{3\beta}\frac{\not{k}_2-\not{p}_1-\not{p}_2+M_{\Xi^0}}{(k_2-p_1-p_2)^2-M_{\Xi^0}^2}\not{p}_2\frac{\not{k}_2-\not{p}_1+M_{\Sigma^+}}{(k_2-p_1)^2-M_{\Sigma^+}^2} \times\not{p}_1\gamma_5 u(k_2) \quad (9.49)$$

9.6 Numerical result

Here we will show the result of our calculation. Af first, we will look around the total cross section of each diagram without form factor. It is always meaningful to see the bare contribution of each diagram in the sense that it help us understand the structure of each T-matrix.

9.6.1 Contributions of each diagram without form factors

Here the totall cross sections of type I diagrams set are shown.

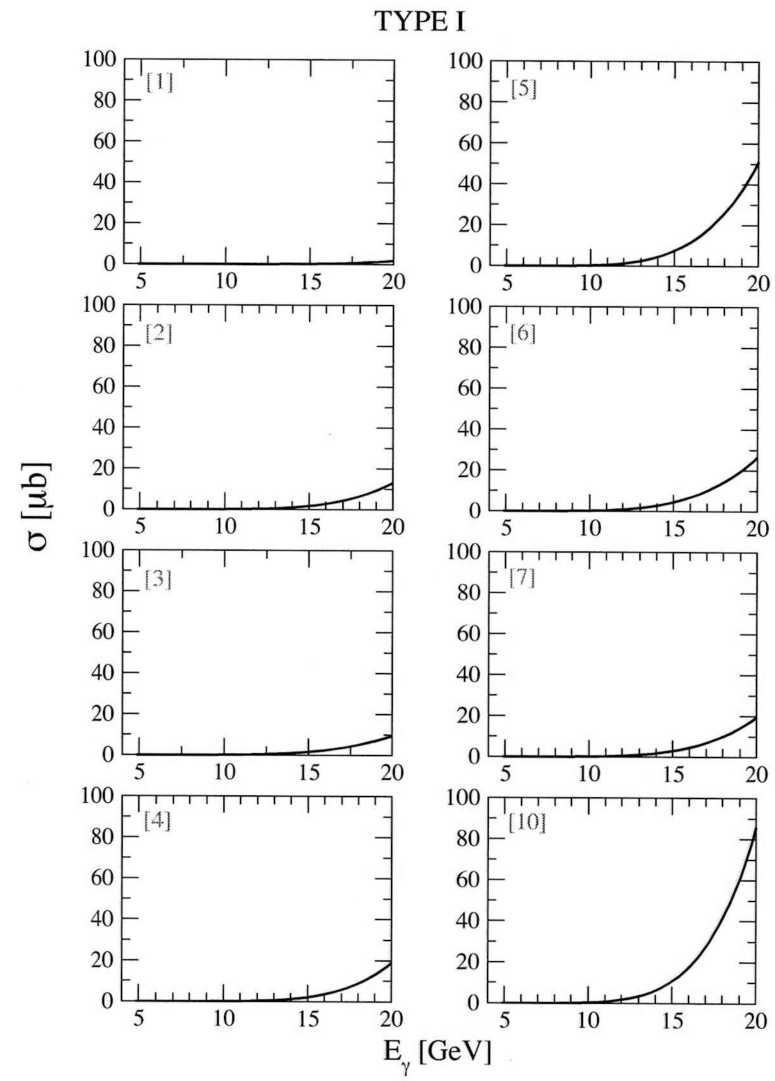

FIG. 9.7: Each contribution of type I diagrams without form factors

Next the totall cross sections of type 2 diagrams set are shown.

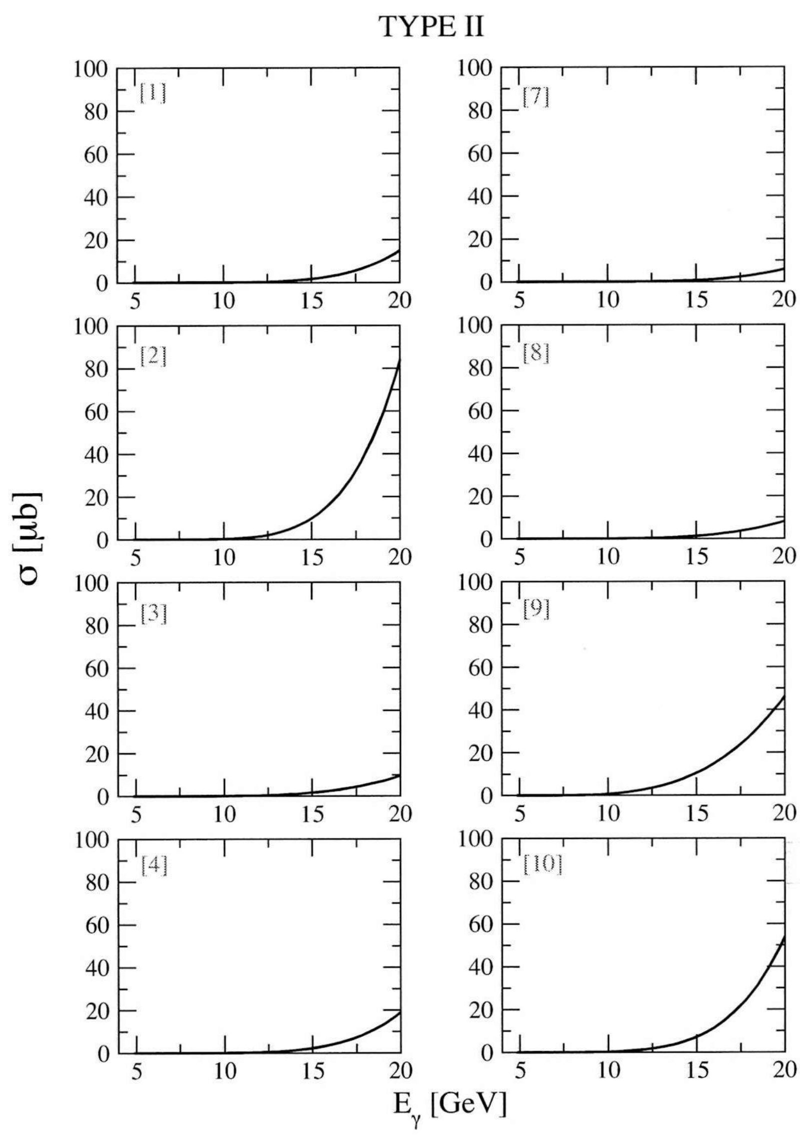

FIG. 9.8: Each contribution of type II diagrams without form factors

We observe that the contributions of the second diagram which include the kaon exchanged t-channel , the 9th diagram with a contact term and the 10th diagram with $\gamma\Omega^-\Omega^-$ coupling are large. Every diagram increases as a function of the photon energy E_γ since there are 4 energy integration in the phase space. Therefore we can expect that we need the stronger form factor to controll these increasing behaviors. The form factors dependent on the three vitual particles can do. We will explain this later.

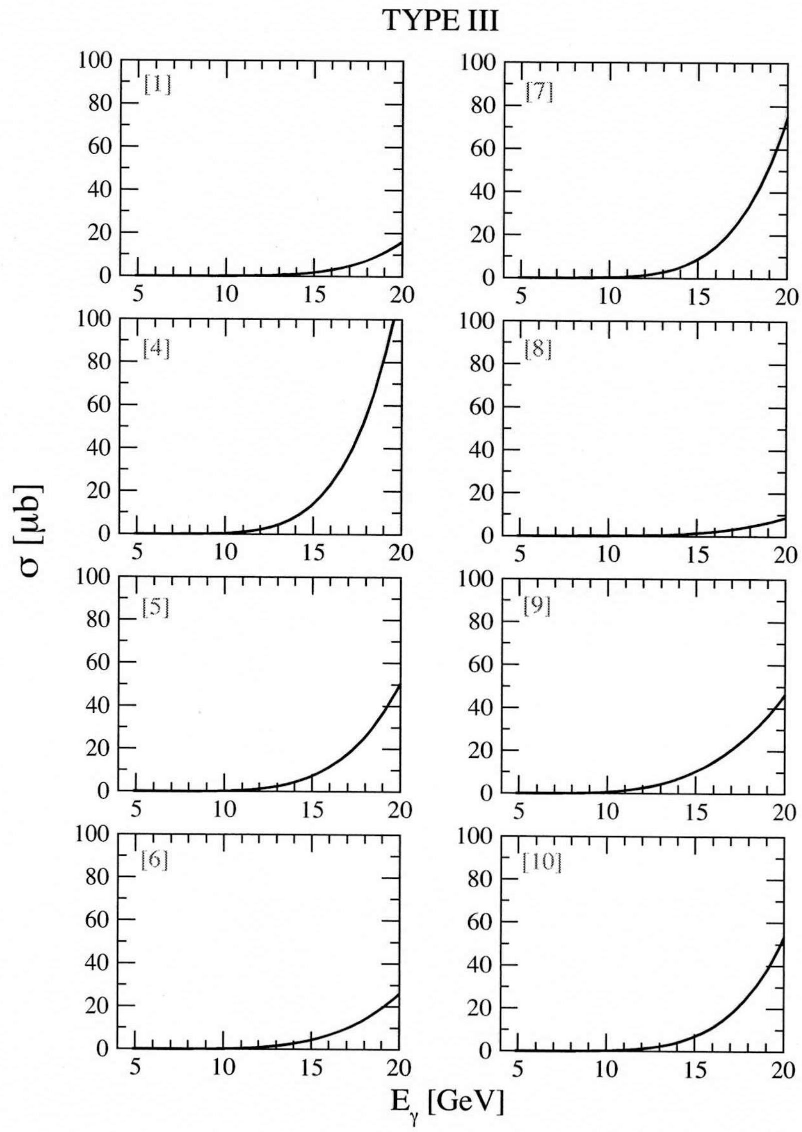

FIG. 9.9: Each contribution of type III diagrams without form factors

FIG. 9.10 shows the total cross section of type III diagrams without form factor. We can see that the 4th and the 7th diagram's contribution are large. We can expect the magnitude of the total cross section of type III can be different from other two types since type III diagrams contains different intermediate states compared with type I and type II. We show the total of each type and total of every diagrams in the next section.

Here we show the contribution of the summation of each diagram set and the total of every diagram we calculated.

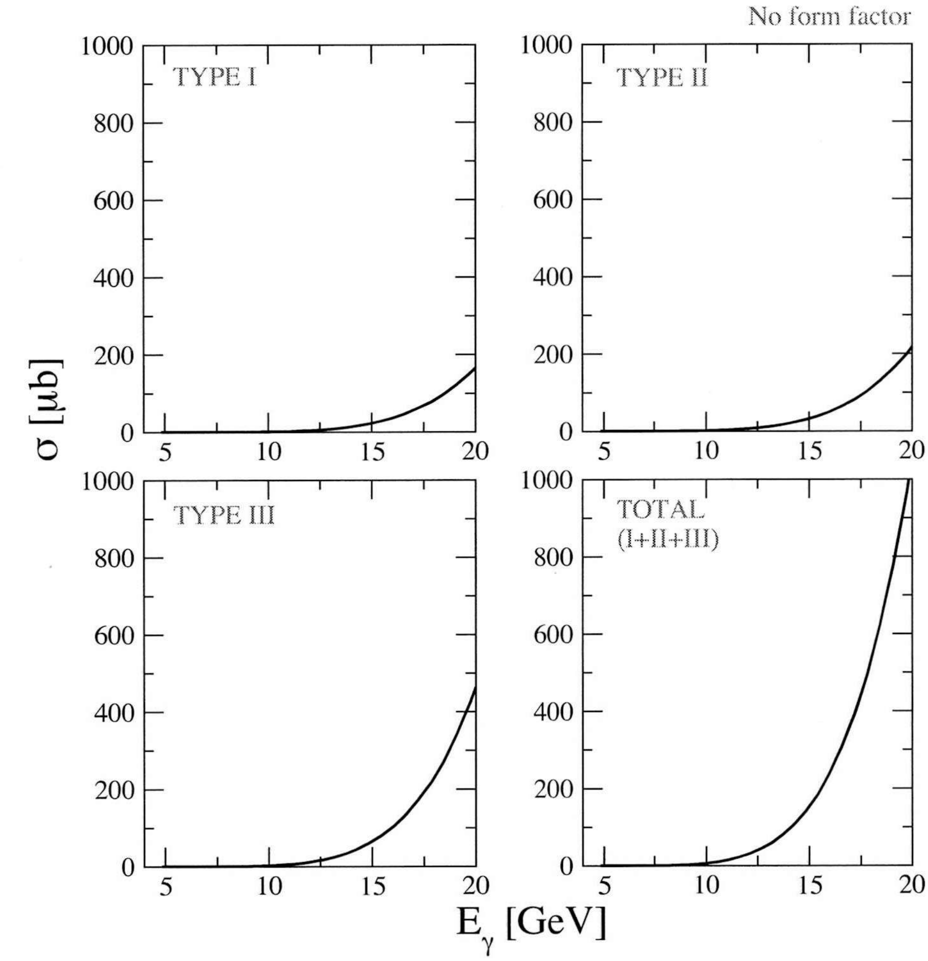

FIG. 9.10: The cross section as a function of E_γ. Each type's contribution and total contribution are shwon.

We observe that the magnitude of the total cross section of type I and type II are similar, but that of thpe III are relatively large. We guess that such a difference is came from the different intermediate particle in the diagrams. The position of the neutral kaon makes the different choice of the intermediate states.

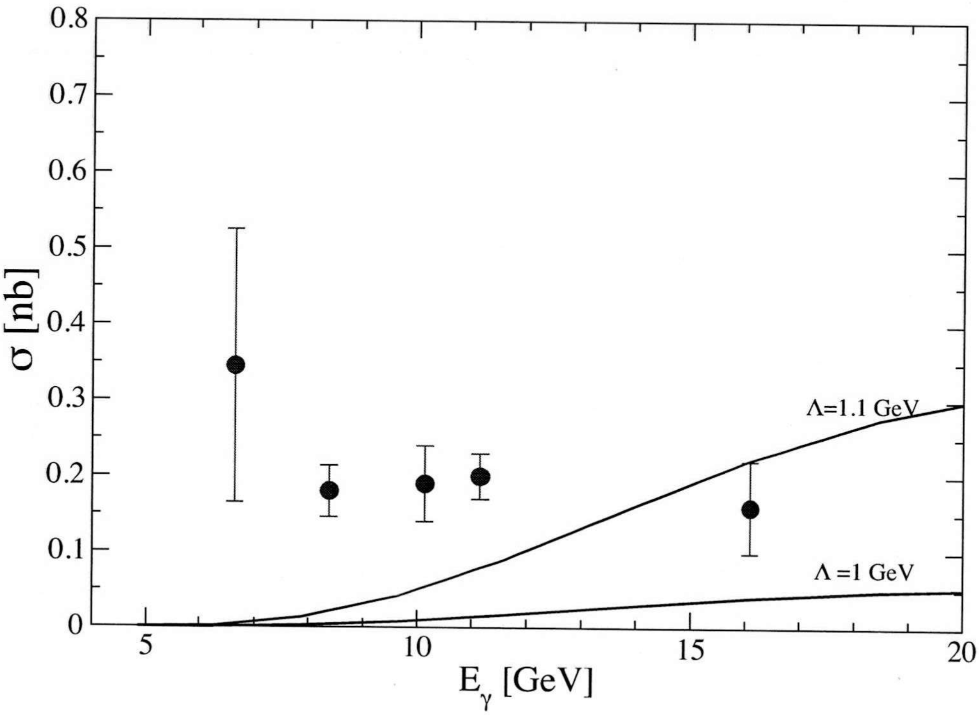

FIG. 9.11: The total cross section as a function of E_γ. The blue points are a extrapolation taken from [79].

Two solid lines in FIG. 9.7 are our result. The extrapolation points are extimated from one $s\bar{s}$ production ($K\Lambda$) and two $s\bar{s}$ production ($KK\Xi$). We try two cut-off parameters in the form factor. We observe that the cross section is very sensitive to the cutoff since cutoff affects 24 diagams. For simplicity we assume that the cutoff of the mesons and that of the baryons are same, $\Lambda_M = \Lambda_B$.

9.7 Summary and outlook

In this work, we calculate order of the total cross section of $\gamma p \to K^+ K^+ K^0 \Omega^-$ in an effective Lagrangian approach. To do this, we consider the 24 Feynman diagrams depending on the position of the photon and the kaon. For simplicity, we consider only the ground state of baryon and kaon as the intermediate states. In our calculation there are two parameters, $g_{K\Xi\Omega}$ and the cutoff Λ. Using $g_{K\Xi\Omega} = 10$, we obtain 0.05 nb around 20 GeV. This work is the first step to predict the Ω^- production. We would like to consider possible resonances to obtain the relevant order calculation in the next work.

10

Summary and Outlook

In this thesis, we have studied kaon photoproductions, starting from single kaon up to three kaons. The general purpose is to understand the mechanism of strangeness production near the threshold region and effect of strangeness in hadron structure. In particular, the strangeness productions are accompanied by a hyperon or its resonance, the reaction is useful to explore the structure of the hyperon resonances.

Single kaon production with ground state hyperons have been studied extensively. Here in this thesis we have studied systematically many different reactions in a common method, that is the effective lagrangian approach. The effective lagrangian is based on the idea which we can construct an effective field with hadronic degrees of freedom instead of quarks and gluons, respecting the symmery of the underlying theory. In most cases, we have not considered explicitly possible nucleon resonances, and just concentrate on the background contributions, which give a smooth behavior of the cross sections as functions of the photon energy. In this regards, our study is not complete but rather qualitative. Nevertheless, systematic study should provide an important aspect of hadron dynamics in the strangeness production reactions.

One general problem is the form factor. This is a necessary ingredient in hadron reactions when compared with experimental data. Physically the form factor is needed to account for the internal structure of hadrons. Practically, this provides a simple mechanism to explain the decreasing tendency of the reaction cross sections for exclusive processes. Nevertheless, the detailed account of the form factor is not given at the microscopic level, and we still need much phenomenological approach. In this regard, we believe that the present study is useful.

As a result of the present study we have found a reasonable set of form factor which can be applied to wide range of processes with parameters of physically reasonable range. This is quite encouraging, because in the previous studies, form factors are always treated as theoretically unknown factors.

As specific subjects, we have studied in detail phi-photoproduction associated two kaons (K+-K-), and three kaons associated with Omega production (KKK). In the former, it is difficult to describe the bump structure of the phi photoproduction with gluon exchchange, Pomeron. And the bump came from the resonance [25] is unkonwn. To explain the bump strucuter near the threthold, we have investicagated several rescattering processes. Including the hadronic process and Pomeron, we explain the bump structure successfully. As the next project, we would like to investigate the phi photoproduction off the neutron with the coupled-channed method. In the latter, we have provided order of the cross sections for the first time prior to experiments. In the present work, only the ground intermediate states are considered. We would like consider the relevant resonaces for the better prediction. In the near future the experiment will be done at JLab and our results can be compared to the results from there.

A

Convention and Kinematics

A.1 Unit, Metric and Dirac matrices

A.1.1 Unit

We use the natual unit($\hbar = c = 1$) in this dissertation. Following this unit system, we obtain some relation between the natual unit and MKS unit as follows:

$$\begin{aligned}
\hbar c &= (6.58 \times 10^{-16}\mathrm{eV}) \times (3 \times 10^{8}\mathrm{m/s}) \\
&= 19.74 \times 10^{-8}\ \mathrm{eV} \cdot \mathrm{m} \\
&= 197.4\mathrm{Mev} \cdot \mathrm{fm} \\
&= 1 \\
\Rightarrow 197.4\ \mathrm{fm} &= \frac{1}{\mathrm{MeV}} \qquad \text{in the natual unit system}
\end{aligned} \tag{A.1}$$

Using the definition $1b = 10^{-28}\mathrm{m}^2$, we obtain

$$\begin{aligned}
1\ \mathrm{GeV}^{-2} &= \left(197.4 \times 10^{-18}\right)^2 \mathrm{m}^2 \\
&= 389.463125\ \mu\mathrm{b}
\end{aligned} \tag{A.2}$$

And the magnitude of electric charge($|e|$) and the fine structure constant(α) are given by

$$
\begin{aligned}
|e| &= \sqrt{\frac{4\pi}{137.04}} && \text{(A.3)}\\
\alpha &= e^2/4\pi = e^2/4\pi\hbar c = 1/137.04 && \text{(A.4)}
\end{aligned}
$$

A.1.2 Metric and Dirac matrix

We follow the convention of Bjorken and Drell [67, 68]. The metric in Minkowski space is defined by

$$
g^{\mu\nu} = g_{\mu\nu} = \begin{pmatrix} 1 & 0 & 0 & 0 \\ 0 & -1 & 0 & 0 \\ 0 & 0 & -1 & 0 \\ 0 & 0 & 0 & -1 \end{pmatrix} \tag{A.5}
$$

Dirac gamma matrices are defined as follows(Bjorken-Drell Notation):

$$
\gamma^0 = \begin{pmatrix} I & 0 \\ 0 & -I \end{pmatrix}, \quad \gamma^i = \begin{pmatrix} 0 & \sigma^i \\ -\sigma^i & 0 \end{pmatrix}, \quad \gamma^5 = \begin{pmatrix} 0 & I \\ I & 0 \end{pmatrix} \tag{A.6}
$$

The Pauli sigma matrices are defined as follows :

$$
\sigma^1 = \begin{pmatrix} 0 & 1 \\ 1 & 0 \end{pmatrix}, \quad \sigma^2 = \begin{pmatrix} 0 & -i \\ i & 0 \end{pmatrix}, \quad \sigma^3 = \begin{pmatrix} 1 & 0 \\ 0 & -1 \end{pmatrix} \tag{A.7}
$$

These matrices satisfy

$$
\begin{aligned}
\{\gamma^\mu, \gamma^\nu\} &= 2g^{\mu\nu}, \quad (\gamma^\mu)^\dagger = \gamma^0\gamma^\mu\gamma^0, \\
(\gamma^0)^2 &= I, \quad (\gamma^0)^\dagger = \gamma^0 \\
\gamma^5 &\equiv i\gamma^0\gamma^1\gamma^2\gamma^3, \quad \{\gamma^\mu, \gamma^5\} = 0, \quad (\gamma^5)^2 = 1, \quad (\gamma^5)^\dagger = \gamma^5 \\
\mathrm{tr}(\sigma^i) &= 0, \quad (\sigma^i)^\dagger = \sigma^i, \quad \sigma^i\sigma^j = \delta^{ij} + i\epsilon^{ijk}\sigma^k && \text{(A.8)}
\end{aligned}
$$

A.2 Spin-1/2 Spinor

Spin-1/2 spinor representation is as follows:

$$u(p, s_z = 1/2) = \begin{pmatrix} \sqrt{E_p + M} \\ 0 \\ \frac{p_z}{\sqrt{E_p+M}} \\ \frac{p_x+ip_y}{\sqrt{E_p+M}} \end{pmatrix}, \qquad u(p, s_z = -1/2) = \begin{pmatrix} 0 \\ \sqrt{E_p + M} \\ \frac{p_x-ip_y}{\sqrt{E_p+M}} \\ -\frac{p_z}{\sqrt{E_p+M}} \end{pmatrix} \tag{A.9}$$

where $E_p = \sqrt{M_p^2 + p^2}$. And normalization condition is given by

$$\bar{u}(p, s)u(p, r) = 2M\delta_{s,r} \tag{A.10}$$

A.3 Spin-3/2 Spinor

We denote the spin-3/2 filelds $u^\mu(p, S)$[1] which satisties the Rarita-Schwinger equations [69]

$$(\not{p} - m)u^\mu(p, s) = 0\,, \quad p_\mu u^\mu(p, s) = \gamma_\mu u^\mu(p, s) = 0 \tag{A.11}$$

A general form of the solutions is obtained by

$$u^\mu(p, S) = \sum_{r,s} C\left(\frac{1}{2}\; 1\; \frac{3}{2}; \frac{s}{2}, \lambda\right) e^\mu_\lambda(p) u(p, s) \tag{A.12}$$

where $S = \lambda + s/2$, $u(p, s)$ is the spin-1/2 spinor defined in Eq. (A.9), and $C(\mathbf{j}_1\; \mathbf{j}_2\; \mathbf{J}; \mu_1\; \mu_2)$ denotes the SU(2) Clebsch-Gordan coefficient for $\mathbf{J}(\mu_1 + \mu_2) = \mathbf{j}_1(\mu_1) + \mathbf{j}_2(\mu_2)$. And $e^\mu_\lambda(p)$ is the basis four-vector and is defined by

$$e^\mu_\lambda = \left(\frac{\hat{e}_\lambda \cdot \vec{p}}{M}, \hat{e}_\lambda + \frac{\vec{p}(\hat{e}_\lambda \cdot \vec{p})}{M(E + M)}\right) \tag{A.13}$$

with

$$\hat{e}_+ = -\frac{1}{\sqrt{2}}(1, i, 0), \quad \hat{e}_0 = (0, 0, 1), \quad \hat{e}_- = \frac{1}{\sqrt{2}}(1, -i, 0) \tag{A.14}$$

[1] $S = +3/2,\; +1/2,\; -1/2,\; -3/2$

More explicitly, Eq. (A.12) can be written as

$$\begin{aligned} u^\mu(p,+3/2) &= e^\mu_+(p,1/2) \\ u^\mu(p,+1/2) &= \sqrt{\frac{2}{3}}e^\mu_0(p,1/2)+\sqrt{\frac{1}{3}}e^\mu_+(p,-1/2) \\ u^\mu(p,-1/2) &= \sqrt{\frac{1}{3}}e^\mu_{-1}(p,1/2)+\sqrt{\frac{2}{3}}e^\mu_0(p,-1/2) \\ u^\mu(p,-3/2) &= e^\mu_-(p,-1/2) \end{aligned} \tag{A.15}$$

A.4 Cross section and Phase space

A.4.1 Cross sections

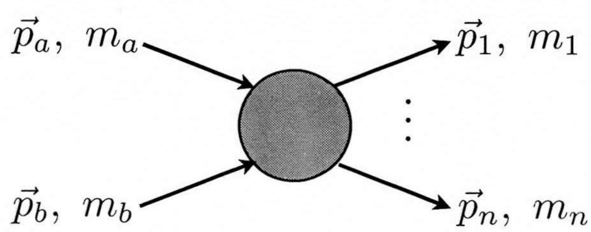

FIG. A.1: Definitions of variables for production of an n-body final state

The definition of the differential cross section in Ref.[73] is given by

$$d\sigma = \frac{(2\pi)^4|\mathcal{M}|^2}{4\sqrt{(p_a\cdot p_b)^2-m_1^2m_2^2}} \times d\Phi_n(p_a+p_b;\ p_1,p_2,\cdots,p_n) \tag{A.16}$$

In the rest frame of m_b, the flux factor in the denominator

$$\sqrt{(p_a\cdot p_b)^2-m_1^2m_2^2} = m_b p_{a\ \mathrm{lab}}\ ; \tag{A.17}$$

while in the center-of-mass frame

$$\sqrt{(p_a\cdot p_b)^2-m_1^2m_2^2} = p_{a\ \mathrm{cm}}\sqrt{s}. \tag{A.18}$$

And the phase space is defined by

$$d\Phi_n(p_a + p_b;\, p_1, \cdots, p_n) = \delta^4\Big(p_a + p_b - \sum_{i=1}^{n} p_i\Big) \prod_{i=1}^{n} \frac{d^3 p_i}{(2\pi)^3 2E_i}. \tag{A.19}$$

A.4.2 Kinematics in two-body scattering process

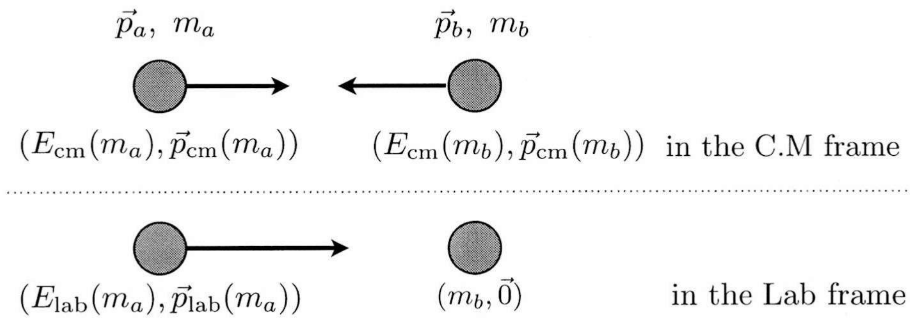

FIG. A.2: Kinematics in the center of mass frame and in the laboratory frame

We consider the two-body scattering process shown in Fig(A.2).

In the center of mass frame, energies of particles are given by

$$E_{\rm cm}(m_a) = \frac{s - m_a^2 + m_b^2}{2\sqrt{s}}, \qquad E_{\rm cm}(m_b) = \frac{s - m_b^2 + m_a^2}{2\sqrt{s}}, \tag{A.20}$$

where $E_{\rm cm}(m)$ is energy as a function of particle mass m. We can easily check the energy conservation relation, $E_{\rm cm}(m_a) + E_{\rm cm}(m_b) = \sqrt{s}$. The absolute values of three momenta are given by

$$|\vec{p}_{\rm cm}(m_a)| = |\vec{p}_{\rm cm}(m_b)| = \frac{\sqrt{(s-(m_a-m_b)^2)(s-(m_a+m_b)^2)}}{2\sqrt{s}} = \frac{\lambda^{1/2}(s, m_a^2, m_b^2)}{2\sqrt{s}}, \tag{A.21}$$

with kinematical function[2] defined by

$$\lambda(x, y, z) = x^2 + y^2 + z^2 - 2xy - 2yz - 2zx. \tag{A.22}$$

In the laboratory frame, where the paricle with mass m_b is the target and that with with m_a is tha beam, the

[2]It is also called the Källen function.

energy and momentum of intital particle are given by

$$E_{\text{lab}}(m_a) = \frac{s - m_a^2 - m_b^2}{2m_b}, \quad E_{\text{lab}}(m_b) = m_b \tag{A.23}$$

and the absolute values of the three momentum of the beam is given by

$$|\vec{p}_{\text{lab}}| = \frac{\lambda^{1/2}(s, m_a^2, m_b^2)}{2m_b} = \sqrt{\left(\frac{s - m_a^2 - m_b^2}{2m_b}\right)^2 - m_a^2} \tag{A.24}$$

And the energy and momentum relation between two frames are given by

$$E_{\text{lab}}(m_a) = \frac{E_{\text{cm}}^2(m_a)}{2m_b} - \frac{m_a^2 + m_b^2}{2m_b}, \qquad |\vec{p}_{\text{cm}}| = |\vec{p}_{\text{lab}}|\frac{m_b}{\sqrt{s}}. \tag{A.25}$$

For the **photoproduction** case, the mass of the beam is zero, $m_a = 0$, we obtain

$$E_{\text{lab}}(m_a) = \frac{E_{\text{cm}}^2(m_a) - m_b^2}{2m_b}, \qquad |\vec{p}_{\text{cm}}(m_a)| = |\vec{p}_{\text{cm}}(m_b)| = \frac{s - m_b^2}{2\sqrt{s}}. \tag{A.26}$$

A.4.3 Two-body phase space

From the definition of phase space in Eq. (A.19), two-boby phase space is given by

$$\begin{aligned}
\Phi_2(P;\, p_1 + p_2) &= \int \frac{d^3p_1}{(2\pi)^3 2E_1} \frac{d^3p_2}{(2\pi)^3 2E_2} \delta^4(P - p_1 - p_2) \\
&= \frac{1}{4(2\pi)^6} \int \frac{d^3p_1}{E_1 E_2} \delta(E - E_1 - E_2) \\
&= \frac{1}{4(2\pi)^6} \int d\Omega_1 \frac{\overline{p}^2 d\overline{p}}{E_1 E_2} \delta(E - E_1 - E_2)
\end{aligned} \tag{A.27}$$

with $P = p_a + p_b = (E, 0)$ and $\overline{p} = |\vec{p}_{1,\text{cm}}| = |\vec{p}_{2,\text{cm}}|$ in the center of mass frame. From the energy conservation,

$$\begin{aligned}
E &= E_1 + E_2 \\
&= \sqrt{m_1^2 + \overline{p}^2} + \sqrt{m_2^2 + \overline{p}^2} \\
\Rightarrow dE &= \frac{\overline{p}d\overline{p}}{E_1} + \frac{\overline{p}d\overline{p}}{E_2} \\
&= \frac{\overline{p}E}{E_1 E_2} d\overline{p}
\end{aligned} \tag{A.28}$$

Substituting Eq. (A.28) to Eq. (A.27), we obtain

$$\Phi_2(P;\, p_1 + p_2) = \frac{1}{4(2\pi)^5} \int d\cos\theta\, \frac{\overline{p}}{E} \tag{A.29}$$

$$= \frac{1}{2(2\pi)^5} \frac{\overline{p}}{E} \tag{A.30}$$

For phase space calculation itselt, we can ues Eq. (A.30), but we use the relation, Eq. (A.29) in the invariant amplitude calculation because there are θ depencence in the integration.

Using the energy and momentum conservation, p is given by

$$\overline{p} = |\vec{p}_{1,\mathrm{cm}}| = \frac{\sqrt{(s-(m_1+m_2)^2)(s-(m_1-m_2)^2}}{2\sqrt{s}} = \frac{\lambda^{1/2}(s, m_1^2, m_2^2)}{2\sqrt{s}}. \tag{A.31}$$

A.4.4 Three-body phase space

For three-body phase space calculation, I use the recursion in Ref. [71]. $\Phi_n(E, \vec{p})$ denotes that the inital state has energy E and momentum $\vec{p}$.

$$\Phi_3(E, \vec{0}) = \int \frac{d^3p_1}{(2\pi)^3 2E_1} \frac{d^3p_2}{(2\pi)^3 2E_2} \frac{d^3p_3}{(2\pi)^3 2E_3} \delta^4(P - p_1 - p_2 - p_3)$$

$$= \int \frac{d^3p_3}{(2\pi)^3 2E_3} \Phi_2(E - E_3, -\vec{p}_3) \tag{A.32}$$

$$= \int \frac{d^3p_3}{(2\pi)^3 2E_3} \Phi_2(\epsilon, 0). \tag{A.33}$$

In the final step, we use the Lorentz invariance of the phase space. And ϵ is defined as follows:

$$(E - E_3)^2 - (-\vec{p}_3)^2 = \epsilon^2 - (\vec{0})^2$$

$$\Rightarrow \epsilon = \sqrt{(E - E_3)^2 - |\vec{p}_3|^2} \tag{A.34}$$

Applying Eq. (A.29) to Eq. (A.33), we obtain

$$\Phi_3(E, \vec{0}) = \int \frac{d^3p_3}{(2\pi)^3 2E_3} \times \left[\frac{1}{2(2\pi)^5} \int d\,\cos\theta \frac{\overline{p}}{\epsilon}\right]$$

$$= \frac{1}{4(2\pi)^8} \int \frac{d^3p_3}{E_3} \int d\,\cos\theta\, \frac{\overline{p}}{\epsilon} \tag{A.35}$$

with

$$\overline{p} = \frac{\lambda^{1/2}(\epsilon^2, m_1^2, m_2^2)}{2\epsilon}. \tag{A.36}$$

A.4.5 Four-body phase space

Similarly let us start with the definition of the four-body phase space.

$$\begin{aligned}\Phi_4(E,\vec{0}) &= \int \frac{d^3p_1}{(2\pi)^3 2E_1}\frac{d^3p_2}{(2\pi)^3 2E_2}\frac{d^3p_3}{(2\pi)^3 2E_3}\frac{d^3p_4}{(2\pi)^3 2E_4}\delta^4(P-p_1-p_2-p_3-p_4)\\ &= \int \frac{d^3p_4}{(2\pi)^3 2E_4}\Phi_3(E-E_4,-\vec{p}_4)\\ &= \int \frac{d^3p_4}{(2\pi)^3 2E_4}\Phi_3(\epsilon_3,0).\end{aligned} \tag{A.37}$$

Applying the relation, Eq.(A.35) to Eq. (A.37), we obtain

$$\begin{aligned}\Phi_4(E,\vec{0}) &= \int \frac{d^3p_4}{(2\pi)^3 2E_4}\times\left[\frac{1}{4(2\pi)^8}\int\frac{d^3p_3}{E_3}\int d\,\cos\theta\,\frac{\overline{p}}{\epsilon_2}\right]\\ &= \frac{1}{8(2\pi)^{11}}\int\frac{d^3p_4}{E_4}\int\frac{d^3p_3}{E_3}\int d\,\cos\theta\,\frac{\overline{p}}{\epsilon_2}\end{aligned} \tag{A.38}$$

with ϵ_3 , ϵ_2 and $\overline{p}$ defined by

$$\epsilon_3 = \sqrt{(E-E_4)^2-|\vec{p}_4|^2} \tag{A.39}$$

$$\epsilon_2 = \sqrt{(\epsilon_3-E_3)^2-|\vec{p}_3|^2} \tag{A.40}$$

$$\overline{p} = \frac{\lambda^{1/2}(\epsilon_2^2, m_1^2, m_2^2)}{2\epsilon_2}. \tag{A.41}$$

B

Additional discussion on the spin density matrix of ϕ photoproduction

B.1 Spin density matrix and decay angular distribution

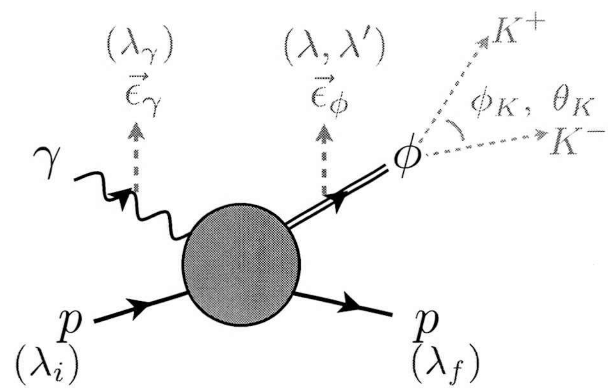

FIG. B.1: Definition of the helicity index and ϕ meson decay

The spin density matrices are correlation function of the phton and ϕ meson polarization. In the laboratory, we cannot measure the phi meson directly. Instead of that, we estimate the properties of phi meson by measuring the decayed kaons from the phi meson. The decay angular distributions of the decayed kaons help us to study the phi meson's properties and they are parameterized by the spin density matrices. We can understand the helicity transition process deeply investigating the spin density matrices of the scattering.

Although we cannot measure the intermediate ϕ meson's helicities, we can get information of helicities of ϕ meson using the decay angular distribution of kaons. This description is shown in FIG. B.1. The spin density matrix of the vector meson is defined as follows:

$$\rho^0_{\lambda,\lambda'} = \frac{1}{N}\sum_{\lambda_\gamma,\lambda_i,\lambda_f} T_{\lambda_f,\lambda;\lambda_i,\lambda_\gamma} T^*_{\lambda_f,\lambda';\lambda_i,\lambda_\gamma} \tag{B.1}$$

$$\rho^1_{\lambda,\lambda'} = \frac{1}{N}\sum_{\lambda_\gamma,\lambda_i,\lambda_f} T_{\lambda_f,\lambda;\lambda_i,-\lambda_\gamma} T^*_{\lambda_f,\lambda';\lambda_i,\lambda_\gamma} \tag{B.2}$$

$$\rho^2_{\lambda,\lambda'} = \frac{i}{N}\sum_{\lambda_\gamma,\lambda_i,\lambda_f} \lambda_\gamma T_{\lambda_f,\lambda;\lambda_i,-\lambda_\gamma} T^*_{\lambda_f,\lambda';\lambda_i,\lambda_\gamma} \tag{B.3}$$

$$\rho^3_{\lambda,\lambda'} = \frac{1}{N}\sum_{\lambda_\gamma,\lambda_i,\lambda_f} \lambda_\gamma T_{\lambda_f,\lambda;\lambda_i,\lambda_\gamma} T^*_{\lambda_f,\lambda';\lambda_i,\lambda_\gamma} \tag{B.4}$$

There are other definitions of the spin density matrix. But I introduce what we need to explain our analysis here. If you want to see more detail explanation, you can find it in many references [64, 80].

The decay angular distribution can be parameterized by the spin density matrix as following;

$$W_1(\cos\theta_K) = \frac{1}{2}(1-\rho^0_{00}) + \frac{1}{2}(3\rho^0_{00}-1)\cos^2\theta_K \tag{B.5}$$

$$W_2(\phi_K - \Phi) = 1 + 2p_\gamma \bar{\rho}^1_{1-1}\cos 2(\phi_K - \Phi) \tag{B.6}$$

$$W_3(\phi_K + \Phi) = 1 + 2p_\gamma \Delta_{1-1}\cos 2(\phi_K + \Phi) \tag{B.7}$$

where $\bar{\rho}^1_{1-1}$ and Δ_{1-1} are defined by

$$\bar{\rho}^1_{1-1} = \frac{1}{2}(\rho^1_{1-1} - \mathrm{Im}\rho^2_{1-1}) \tag{B.8}$$

$$\Delta_{1-1} = \frac{1}{2}(\rho^1_{1-1} + \mathrm{Im}\rho^2_{1-1}). \tag{B.9}$$

Angles in the above equations are defined in the reaction plane in FIG. B.2.

Angles of the decayed kaons are defined in Gottfried-Jackson (G.J.) system. Definitions in G.J. system are shown in FIG. B.3.

In G. J. system, ϕ meson is at rest and the photon momentum is parellelle to the z-axis. Using the formailsm we disscussed above, let us discuss the helicity property of ϕ photoproduction more. It is well known that in the forward angle region, t-channel contribution is dominant. Analysis of the spin density matrix and the

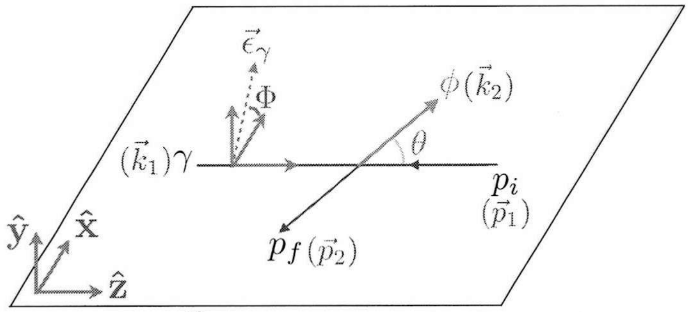

FIG. B.2: Kinematics in C.M. system, $\vec{k}_1 + \vec{p}_1 = 0$. Φ denotes the azimuthal angle for the reaction plane.

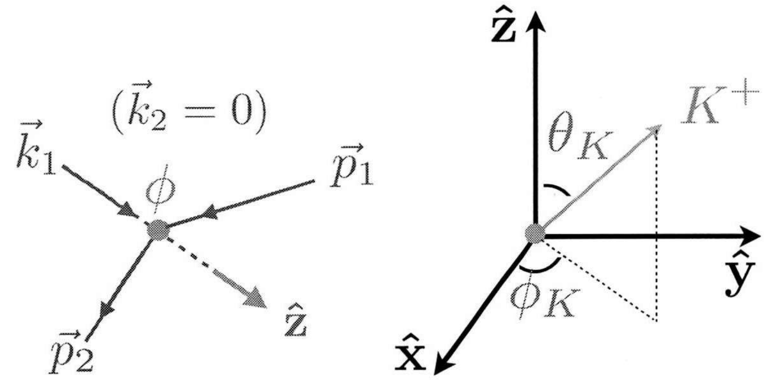

FIG. B.3: Kinematics in G.J. system.

decay angular distributon help us understand the properties of the exchanged particle through t-channel.

B.2 $W_1(\cos\theta_K)$ and spin one-flip process

Here we will discuss about $W_1(\cos\theta_K)$ to understand spin flip process in the ϕ photoproduction. Let me rewrite the definition of $W_1(\cos\theta_K)$ and ρ^0_{00}.

$$W_1(\cos\theta_K) = \frac{1}{2}(1-\rho^0_{00}) + \frac{1}{2}(3\rho^0_{00} - 1)\cos^2\theta_K \tag{B.10}$$

$$\rho^0_{00} = \frac{1}{N}(|T_{0-1}|^2 + |T_{01}|^2) \tag{B.11}$$

$$= \frac{|T_{0-1}|^2 + |T_{01}|^2}{|T_{-1-1}|^2 + |T_{-11}|^2 + |T_{0-1}|^2 + |T_{01}|^2 + |T_{1-1}|^2 + |T_{11}|^2} \tag{B.12}$$

We ignore the helicity indeces of the baryon since they are same in the both helicity amplitude in Eq.(B.1-B.4). From the denominator of Eq.(B.12), we know that ρ^0_{00} is related to the spin one-flip process. If ρ^0_{00} is large enough, it means the the spin one-flip process is dominant in t-channel. Otherwise, the the spin one-flip process is not important in t-channel and it indicates that the exchanged particle through t-channel is a particle with $J = 0$.

To check whether the spin one-flip process is dominant or not, let us consider threee extrem cases:

1. If $\rho^0_{00} = 0$ (no spin one-flip), $W_1(\cos\theta_K) = 0.5 - 0.5\cos^2\theta_K$.

2. If $\rho^0_{00} = 0.5$, $W_1(\cos\theta_K) = 0.25 + 0.25\cos^2\theta_K$.

3. If $\rho^0_{00} = 1$ (only spin one flip exists), $W_1(\cos\theta_K) = \cos^2\theta_K$.

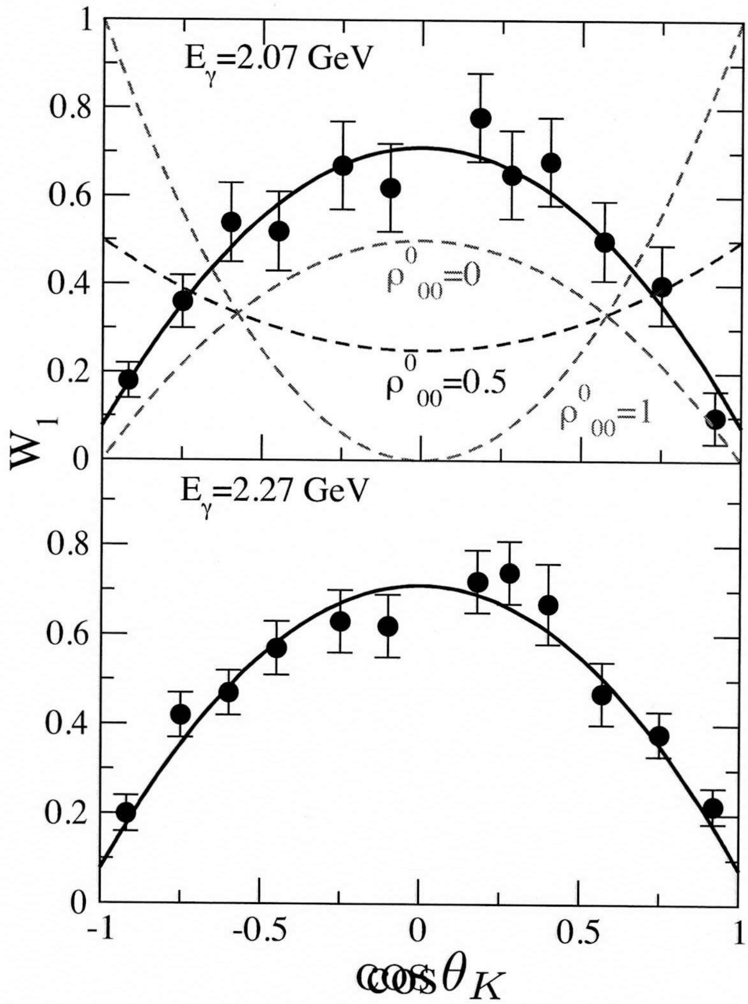

FIG. B.4: W_1 as a function of $\cos\theta$. The dots are LEPS data and solid line is our theoretical result. Threee cases of ρ^0_{00} are also presented.

Even though it looks that the there are some contribution of ρ^0_{00} , but the experimental data and our result support that the spin one-flip process is not dominant. The conclusion of FIG. B.4 is that the exchanged particle through t-channel has the spin quantum number, $J \simeq 0$. This conclusion gives us the consistent description of Pomeron ($J^{PC} = 0^{++}$) exchange process and it shows that the hadronic description can explain $J = 0$ particle exchange process also.

B.3 $W_2(\phi_K - \Phi)$, $W_3(\phi_K + \Phi)$ and natural parity

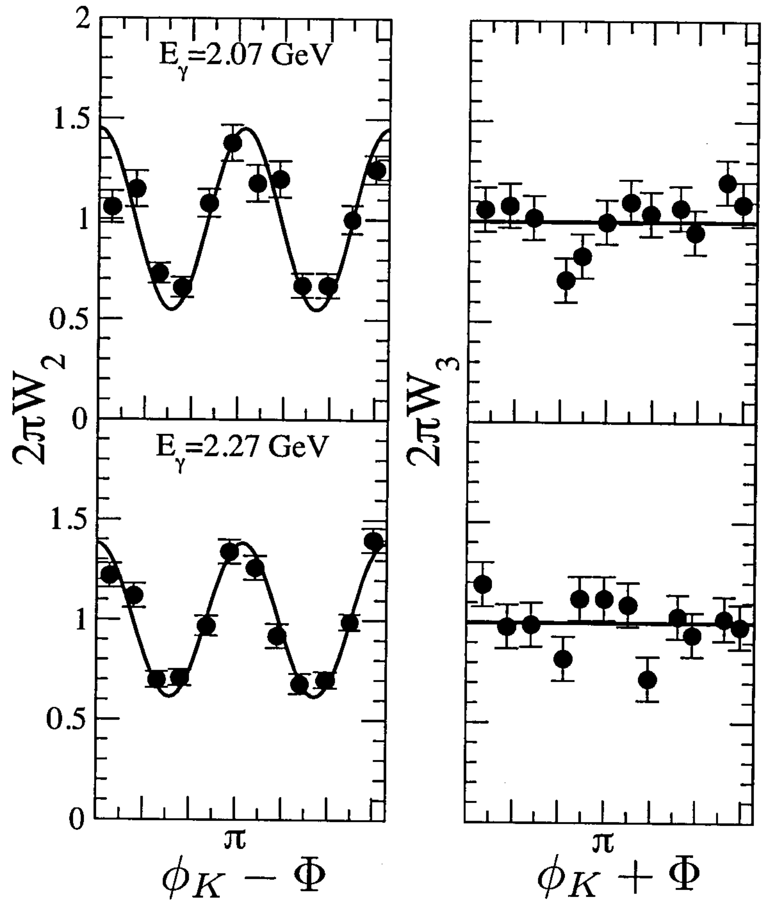

FIG. B.5: W_2 and W_3 as functions of specific angles. The upper pannels are for $E_\gamma = 2.07$ GeV and the lower pannels are for $E_\gamma = 2.27$ in our work. Data are taken from [21].

Let me rewirte definitions of W_2 and W_3 again.

$$W_2(\phi_K - \Phi) = 1 + 2p_\gamma \bar{\rho}^1_{1-1} \cos 2(\phi_K - \Phi) \tag{B.13}$$

$$W_3(\phi_K + \Phi) = 1 + 2p_\gamma \Delta_{1-1} \cos 2(\phi_K + \Phi) \tag{B.14}$$

where p_γ is the photon strenth which is 1 in 100% polarized beam. At high energy, it is known that the following relations are extablished well :

$$T^{N/U}_{-\lambda,-\lambda_\gamma} = \pm(-1)^{\lambda-\lambda_\gamma} T_{\lambda,\lambda_\gamma} \tag{B.15}$$

where the upper $+$ sign is for the natural parity (N), the lower $-$ sign is for the unnatural parity (U). Applying Eq.(B.15) to Eq. (B.13) and Eq. (B.14), we obtain

- If the exchanged particle has the natural parity,

$$\bar{\rho}^1_{1-1} = \frac{1}{N}|T_{11}|^2\,, \qquad \Delta_{1-1} = \frac{1}{N}|T_{1-1}|^2 \tag{B.16}$$

- If the exchanged particle has the unnatural parity,

$$\bar{\rho}^1_{1-1} = -\frac{1}{N}|T_{11}|^2\,, \qquad \Delta_{1-1} = -\frac{1}{N}|T_{1-1}|^2 \tag{B.17}$$

From the relations of Eq. (B.16) and Eq. (B.17), we can learn two things. Firstly, the sign of $\bar{\rho}^1_{1-1}$ and Δ_{1-1}, we can determine the exchanged particle has the natural parity or unnatural parity. Secondly, comparing the magnitudes of $\bar{\rho}^1_{1-1}$ and Δ_{1-1}, we can see that the spin conserved process is dominant or spin two flip prcess is dominant.

Now we are in a position to check the experimental data and our theoretical result. First of all FIG. B.5 tells us that the sign of $\bar{\rho}^1_{1-1}$ is positive. And our result shows that the magnitude of $\bar{\rho}^1_{1-1}$ is larger than that of Δ_{1-1}. It means that the spin conserved process is dominant and the spin two-flip process is ignorable. The finite magnitude of $W_3(\phi_K + \Phi)$ indicates that the Eq. (B.15) is a good approximation at low energy region.

C

Miscellaneous notes

C.1 Unitarity of S matrix, imaginary part of invariant amplitude and cutkosky rule

C.1.1 Imaginary part of invariant amplitude through unitarity of S-matrix

Let us star with definition of S-matrix.

$$\begin{aligned} S_{fi} &= 1 - iT_{fi} && \text{(C.1)} \\ T_{fi} &= (2\pi)^4 \mathcal{M}_{fi} \delta^{(4)}(p_1^i + p_2^i - p_1^f - p_2^f - \cdots p_n^f) && \text{(C.2)} \end{aligned}$$

Using the unitarity of S-matrix, we can obtain the imaginary part of T-matrix.

$$\begin{aligned} S^\dagger S &= 1 \\ (1 + iT^\dagger)(1 - iT) &= 1 - iT + iT^\dagger + T^\dagger T = 1 \\ 2\,\mathrm{Im}T &= -T^\dagger T && \text{(C.3)} \end{aligned}$$

$$\begin{aligned} \Rightarrow\ 2\,\mathrm{Im}\,\langle b|T|a\rangle &= -\langle b|T^\dagger T|a\rangle \\ &= -\int \frac{d\ell}{(2\pi)^3 2E_\ell} \int \frac{d\ell_D}{(2\pi)^3 2E_D} \langle b|T^\dagger|f\rangle \langle f|T|a\rangle && \text{(C.4)} \end{aligned}$$

Here

$$\langle b|T^\dagger|f\rangle = \Big[\langle f|T|b\rangle\Big]^\dagger = T^\dagger_{b\to f} = T_{f\to b} \tag{C.5}$$

In terms of invariant amplitudes,

$$\begin{aligned}
2\,\mathrm{Im}\mathcal{M}(a\to b) &= -\frac{1}{(2\pi)^6}\int\frac{d^3\ell}{2E_\ell}\int\frac{d^3\ell_D}{2E_D}\mathcal{M}^\dagger(b\to f)\mathcal{M}(a\to f)(2\pi)^4\delta(P_a-\ell-\ell_D)\\
&= -\frac{1}{(2\pi)^2}\int\frac{d^3\ell}{2E_\ell}\underbrace{\int\frac{d^3\ell_D}{2E_D}\delta(P_a-\ell-\ell_D)}_{I_1}\mathcal{M}(f\to b)\mathcal{M}(a\to f)
\end{aligned} \tag{C.6}$$

Here $P_a = k_1 + p_1 = (\sqrt{s}, 0)$ in CM frame.

We insert a identity $\int dM_D^2\,\delta(M_D^2-\ell_D^2) = 1$ into I_1 in Eq.(C.6).

$$I_1 = \int\frac{d^3\ell_D}{2E_D}\int dM_D^2\,\delta(M_D^2-\ell_D^2)\,\delta(P_a-\ell-\ell_D) \tag{C.7}$$

And

$$\begin{aligned}
M_D^2 &= E_D^2-\vec{\ell}_D^{\,2}\\
dM_D^2 &= 2E_D dE_D
\end{aligned} \tag{C.8}$$

Applying Eq.(C.8) to Eq.(C.7), we get

$$\begin{aligned}
I_1 &= \int\frac{d^3\ell_D}{2E_D}\,(2E_D dE_D)\,\delta(M_D^2-\ell_D^2)\,\delta(P_a-\ell-\ell_D)\\
&= \int d^4\ell_D\,\delta(M_D^2-\ell_D^2)\,\delta(P_a-\ell-\ell_D)\\
&= \delta\big[M_D^2-(P_a-\ell)^2\big]\,, \qquad (\ell_D = P_a-\ell)
\end{aligned} \tag{C.9}$$

Substituting Eq.(C.9) to Eq.(C.6), we obtain

$$2\,\mathrm{Im}\mathcal{M}(a\to b) = -\frac{1}{(2\pi)^2}\underbrace{\int\frac{d^3\ell}{2E_\ell}\,\delta\big[M_D^2-(P_a-\ell)^2\big]}_{I_2}\,\mathcal{M}(f\to b)\mathcal{M}(a\to f) \tag{C.10}$$

Next let us consider I_2.

$$I_2 = \int \frac{|\vec{\ell}|^2 d|\vec{\ell}|}{2E_\ell} d\Omega\, \delta\left[M_D^2 - (\sqrt{s} - E_\ell)^2 + |\vec{\ell}|^2\right] \tag{C.11}$$

Using $E_\ell dE_\ell = |\vec{\ell}| d|\vec{\ell}|$, we can rewrite Eq. (C.11).

$$\begin{aligned} I_2 &= \int \frac{|\vec{\ell}| dE_\ell}{2} d\Omega\, \delta\left[M_D^2 - s - m_\ell^2 + 2\sqrt{s}E_\ell\right] \\ &= \int \frac{|\vec{\ell}| dE_\ell}{2} d\Omega\, \frac{1}{2\sqrt{s}} \delta(E_\ell - E_\ell') \\ &= \frac{|\vec{\ell}|}{4\sqrt{s}} \int d\Omega \end{aligned} \tag{C.12}$$

Substituting Eq. (C.12) into Eq. (C.10), we obtain

$$\begin{aligned} 2\,\mathrm{Im}\mathcal{M}(a \to b) &= -\frac{1}{(2\pi)^2} \times \frac{|\vec{\ell}|}{4\sqrt{s}} \int d\Omega\, \mathcal{M}(f \to b)\mathcal{M}(a \to f) \\ \Rightarrow \quad \mathrm{Im}\mathcal{M}(a \to b) &= -\frac{|\vec{\ell}|}{32\pi^2\sqrt{s}} \times \int d\Omega\, \mathcal{M}(f \to b)\mathcal{M}(a \to f) \end{aligned} \tag{C.13}$$

C.1.2 Cutkosky Rule

When we calculate a invariant amplitude, we can apply the following rule known as cutkosky rule:

$$T \longrightarrow 2i\,\mathrm{Im}T \tag{C.14}$$

$$\frac{1}{\ell^2 - m^2} \longrightarrow -2\pi i\, \delta(\ell^2 - m^2) \tag{C.15}$$

When we apply the cutkosky rule, we can get the exactly same value $\mathrm{Im}\mathcal{M}$ as we concern in the Eq. (C.13).

C.2 Form factors

There are much ambiguities in how to choose form facters in hadron physics since there no way how to derive form factor from a fundamental theroy. Theoretical physicist have tried sever types of form factors to explain experimental data. Here I will briefly show their compatibilities.

$$F_1(p^2) = \frac{\Lambda^2 - m^2}{\Lambda^2 - p^2} \tag{C.16}$$

$$F_2(p^2) = \left[\frac{n\Lambda^4}{n\Lambda^4 + (p^2 - m^2)^2}\right]^n \tag{C.17}$$

$$F_3(p^2) = \mathrm{Exp}\left[\frac{(p^2 - m^2)^2}{\Lambda^4}\right] \tag{C.18}$$

$F_1(p^2)$ is the dipole type. And F_2 and F_3 have the following relation :

$$F_3 = \lim_{n\to\infty} F_2 \tag{C.19}$$

The following figure shows the behavior of those three form factors.

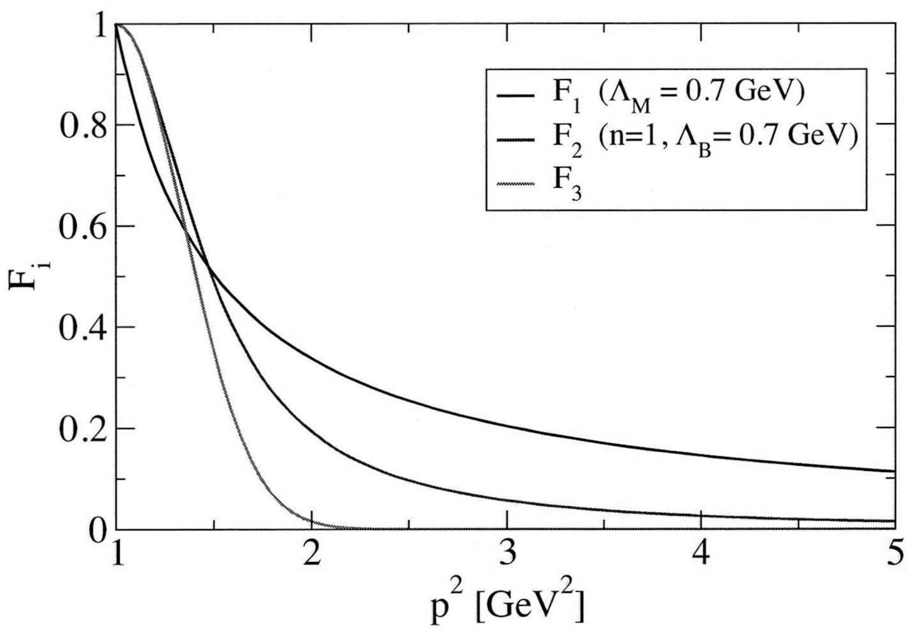

FIG. C.1: Momentum dependence of three form factors

C.2.1 Type I form factor

Type I form fator for meson-meson-baryon vertex is given by

$$
\begin{aligned}
F(q^2,p_1^2,p_2^2) &= F_M(q^2)F_B(p_1^2)F_B(p_2^2) \\
F_M(q^2) &= \frac{\Lambda_M^2 - M_M^2}{\Lambda_M^2 - q^2} \\
F_B(p^2) &= \left[\frac{n\Lambda_B^4}{n\Lambda_B^4 + (p^2 - M_B^2)}\right]^n
\end{aligned} \tag{C.20}
$$

M_M and M_B stands for the meson mass and baryon mass respectively. F_1 type is used for a scalar meson and F_2 type is used for a baryon and a vector meson. These choice of form factor explain many data successfully in several works [54, 66] and it is most recommanded.

C.2.2 Type II form fator

Type I form fator for meson-meson-baryon vertex is given by

$$
\begin{aligned}
F(q^2,p_1^2,p_2^2) &= F_M(q^2)F_B(p_1^2)F_B(p_2^2) \\
F_M(q^2) &= \left[\frac{n\Lambda_M^4}{n\Lambda_M^4 + (q^2 - M_M^2)}\right]^n \\
F_B(p^2) &= \left[\frac{n\Lambda_B^4}{n\Lambda_B^4 + (p^2 - M_B^2)}\right]^n
\end{aligned} \tag{C.21}
$$

F_2 type is used for not only meson but also baryon. This kind of form factor is also available for several cases [26].

C.2.3 Type III form fator : overall type

This overall type is motivaed from ϕ meson photoproduction in chapter 3. We multiply two F_2 type form facotr which depends on t and s respectively to the gauge-invariant invariant amplitude set as follows:

$$
\mathcal{M} = (\mathcal{M}_s + \mathcal{M}_t + \mathcal{M}_c + \cdots)F(s)F(t) \tag{C.22}
$$

C.2.4 F_2 in the limit $n \to \infty$

Firstly we use the following definition of the exponetial to prove $F_3 = \lim_{n\to\infty} F_2$.

$$
e^x = \lim_{n\to\infty}\left[1 + \frac{x}{n}\right]^n \tag{C.23}
$$

Now let us consider the form factor F_2 in the limit $n \to \infty$.

$$\begin{aligned}\lim_{n\to\infty} F_2(n,\ \Lambda,\ p^2) &= \lim_{n\to\infty}\left[\frac{n\Lambda^4}{n\Lambda^4+(p^2-m^2)^2}\right]^n \\ &= \lim_{n\to\infty}\left[\frac{1}{1+\frac{(p^2-m^2)^2}{n\Lambda^4}}\right]^n \end{aligned} \tag{C.24}$$

Here we use the binomial expansion:

$$(1+x)^\alpha = 1+\alpha x+\frac{\alpha(\alpha-1)}{2!}x^2+\cdots \quad . \tag{C.25}$$

Applying Eq.(C.25) to Eq.(C.24), we obtain

$$\lim_{n\to\infty} F(n,\ \Lambda,\ p^2) = \lim_{n\to\infty}\left[1-\frac{(p^2-m^2)^2}{n\Lambda^4}+\frac{-1(-1-1)}{2!}\left(\frac{(p^2-m^2)^2}{n\Lambda^4}\right)^2+\cdots\right]^n \tag{C.26}$$

$$\simeq \lim_{n\to\infty}\left[1-\frac{(p^2-m^2)^2/\Lambda^4}{n}\right]^n \tag{C.27}$$

$$= \mathrm{Exp}\left[-\frac{(p^2-m^2)^2}{\Lambda^4}\right] \tag{C.28}$$

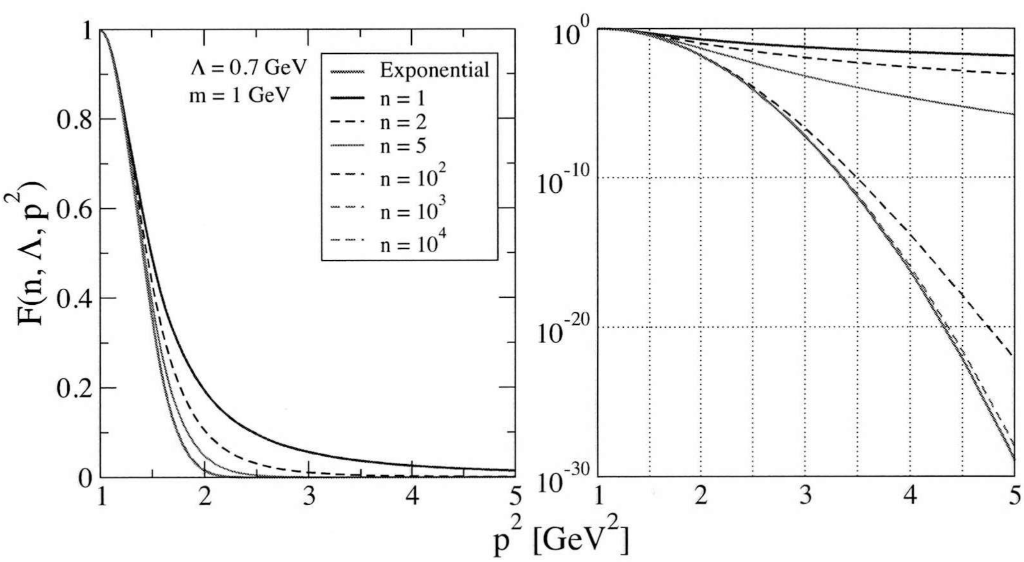

FIG. C.2: The F_2 type form factor for various n values. When $n \to \infty$, the F_2 type form factor approaches to the exponetial function denoted red solid line.

Bibliography

[1] S. Weinberg, Physica A **96**, 327 (1979)

[2] V. G. J. Stoks and T. A. Rijken, Phys. Rev. C **59**, 3009 (1999) [nucl-th/9901028].

[3] M. Q. Tran *et al.* [SAPHIR Collaboration], Phys. Lett. B **445**, 20 (1998).

[4] R. H. Dalitz and S. F. Tuan, Phys. Rev. Lett. **2**, 425 (1959).

[5] R. H. Dalitz and S. F. Tuan, Annals Phys. **10**, 307 (1960).

[6] D. Jido, A. Hosaka, J. C. Nacher, E. Oset and A. Ramos, Phys. Rev. C **66**, 025203 (2002) [hep-ph/0203248].

[7] A. Boyarski, R. E. Diebold, S. D. Ecklund, G. E. Fischer, Y. Murata, B. Richter and M. Sands, Phys. Lett. B **34**, 547 (1971).

[8] D. P. Barber, J. B. Dainton, L. C. Y. Lee, R. Marshall, J. C. Thompson, D. T. Williams, T. J. Brodbeck and G. Frost *et al.*, Z. Phys. C **7**, 17 (1980).

[9] H. Kohri *et al.* [LEPS Collaboration], Phys. Rev. Lett. **104**, 172001 (2010) [arXiv:0906.0197 [hep-ex]].

[10] S. P. Barrow *et al.* [Clas Collaboration], Phys. Rev. C **64**, 044601 (2001) [hep-ex/0105029].

[11] C. Gobbi, C. L. Schat and N. N. Scoccola, Nucl. Phys. A **598**, 318 (1996) [hep-ph/9509211].

[12] M. H. Alston, L. W. Alvarez, P. Eberhard, M. L. Good, W. Graziano, H. K. Ticho and S. G. Wojcicki, Phys. Rev. Lett. **6**, 698 (1961).

[13] S. Janssen, J. Ryckebusch, D. Debruyne and T. Van Cauteren, Phys. Rev. C **65**, 015201 (2002) [nucl-th/0107028].

[14] J. Beringer *et al.* [Particle Data Group Collaboration], Phys. Rev. D **86**, 010001 (2012).

[15] N. P. Samios, M. Goldberg, and B. T. Meadows, Rev. Mod. Phys. **46**, 49 (1974); K.-T. Chao, N. Isgur, and G. Karl, Phys. Rev. **D 23**, 155 (1981).

[16] J. W. Price *et al.* [CLAS Collaboration], Nucl. Phys. A **754**, 272 (2005) [nucl-ex/0402006].

[17] J. W. Price *et al.* [CLAS Collaboration], Phys. Rev. C **71**, 058201 (2005) [nucl-ex/0409030].

[18] Z. Ahmed *et al.* [HAPPEX Collaboration], Phys. Rev. Lett. **108**, 102001 (2012) [arXiv:1107.0913 [nucl-ex]] and references therein.

[19] S. Donnachie, G. Dosch, P. Landshoff, and O. Nachtmann, *Pomeron Physics and QCD* (Cambridge University Press, Cambridge, UK, 2002), and references therein.

[20] F.E. Close and A. Donnachie, in *Electromagnetic Interactions and Hadronic Structure* edited by F. Close, S. Donnachie, and G. Shaw, (Cambridge University Press, Cambridge, UK, 2007).

[21] T. Mibe *et al.* [LEPS Collaboration], Phys. Rev. Lett. **95**, 182001 (2005) [nucl-ex/0506015].

[22] W. C. Chang *et al.* [LEPS Collaboration], Phys. Rev. C **82**, 015205 (2010) [arXiv:1006.4197 [nucl-ex]].

[23] A. I. Titov, T. -S. H. Lee, H. Toki and O. Streltsova, Phys. Rev. C **60**, 035205 (1999).

[24] J. Beringer et al., (Particle Data Group), Phys. Rev. D **86**, 010001 (2012).

[25] S. Ozaki, A. Hosaka, H. Nagahiro and O. Scholten, Phys. Rev. C **80**, 035201 (2009) [Erratum-ibid. C **81**, 059901 (2010)] [arXiv:0905.3028[hep-ph]].

[26] S. -I. Nam, A. Hosaka and H. -Ch. Kim, Phys. Rev. D **71**, 114012 (2005) [hep-ph/0503149].

[27] L. D. Landau, Nucl. Phys. **13**, 181 (1959).

[28] R. E. Cutkosky, J. Math. Phys. **1**, 429 (1960).

[29] A. Donnachie and P. V. Landshoff, Phys. Lett. **B 185**, 403 (1987).

[30] A. I. Titov and T. S. H. Lee, Phys. Rev. C **67**, 065205 (2003) [nucl-th/0305002].

[31] A. I. Titov and B. Kampfer, Phys. Rev. C **76**, 035202 (2007) [arXiv:0705.2010[nucl-th]].

[32] R. Machleidt, Adv. Nucl. Phys. **19**, 189 (1989).

[33] T. .A. Rijken, Phys. Rev. C **73**, 044007 (2006) [nucl-th/0603041].

[34] A. I. Titov and T. S. H. Lee, Phys. Rev. C **66**, 015204 (2002)

[35] U. -G. Meissner, V. Mull, J. Speth and J. W. van Orden, Phys. Lett. B **408**, 381 (1997) [hep-ph/9701296].

[36] P. Mergell, U. G. Meissner and D. Drechsel, Nucl. Phys. A **596**, 367 (1996) [hep-ph/9506375].

[37] R. A. Adelseck, C. Bennhold, and L. E. Wright, Phys. Rev. C **32**, 1681 (1985).

[38] B. Friman and M. Soyeur, Nucl. Phys. A **600**, 477 (1996) [nucl-th/9601028].

[39] H. Kaneko, A. Hosaka and O. Scholten, Eur. Phys. J. A **48**, 56 (2012) [arXiv:1112.4776 [hep-ph]].

[40] A. Kiswandhi and S. N. Yang, Phys. Rev. C **86**, 015203 (2012) [Erratum-ibid. C **86**, 019904 (2012)] [arXiv:1112.6105 [nucl-th]].

[41] A. Kiswandhi, J. -J. Xie and S. N. Yang, Phys. Lett. B **691**, 214 (2010) [arXiv:1005.2105 [hep-ph]].

[42] K. H. Glander, J. Barth, W. Braun, J. Hannappel, N. Jopen, F. Klein, E. Klempt and R. Lawall *et al.*, Eur. Phys. J. A **19**, 251 (2004) [nucl-ex/0308025].

[43] R. Bradford *et al.* [CLAS Collaboration], Phys. Rev. C **73**, 035202 (2006)

[44] M. Sumihama *et al.* [LEPS Collaboration], Phys. Rev. C **73**, 035214 (2006) [hep-ex/0512053].

[45] K. Hicks *et al.* [LEPS Collaboration], Phys. Rev. C **76**, 042201 (2007).

[46] P. Achenbach, C. Ayerbe Gayoso, J. C. Bernauer, S. Bianchin, R. Bohm, O. Borodina, D. Bosnar and M. Bosz *et al.*, Eur. Phys. J. A **48**, 14 (2012) [arXiv:1104.4245 [nucl-ex]].

[47] K. Hicks, D. Keller and W. Tang, AIP Conf. Proc. **1374**, 177 (2011) [arXiv:1012.3129 [nucl-ex]].

[48] S. Janssen, J. Ryckebusch, W. Van Nespen, D. Debruyne and T. Van Cauteren, Eur. Phys. J. A **11**, 105 (2001) [nucl-th/0105008].

[49] Y. Oh and H. Kim, Phys. Rev. C **73**, 065202 (2006) [hep-ph/0602112].

[50] Y. Oh and H. Kim, Phys. Rev. C **74**, 015208 (2006) [hep-ph/0605105].

[51] B. G. Yu, T. K. Choi and W. Kim, Phys. Lett. B **701**, 332 (2011) [arXiv:1104.3672 [nucl-th]].

[52] S. -H. Kim, S. -i. Nam, Y. Oh and H. -Ch. Kim, Phys. Rev. D **84**, 114023 (2011) [arXiv:1110.6515 [hep-ph]].

[53] A. I. Titov, H. Ejiri, H. Haberzettl and K. Nakayama, Phys. Rev. C **71**, 035203 (2005) [nucl-th/0410098].

[54] K. Nakayama, Y. Oh and H. Haberzettl, Phys. Rev. C **74**, 035205 (2006) [hep-ph/0605169].

[55] A. I. Titov *et al.* Phys. Rev. C71 035203 (2005)

[56] A. I. Titov, B. Kämpfer, B.L. Reznik Phys. Rev. C **65**, 065202 (2002).

[57] T. Sato and T.-S. H. Lee Phys. Rev. C **54**, 2660 (1996).

[58] C. Wu, J. Barth, W. Braun, J. Ernst, K. H. Glander, J. Hannappel, N. Jopen and H. Kalinowsky *et al.*, Eur. Phys. J. A **23**, 317 (2005).

[59] [Aachen-Berlin-Bonn-Hamburg-Hedielberg-Munich Collaboration], Phys. Rev. **175**, 1669 (1968).

[60] J. Ballam *et al.* Phys. Rev. D **7**, 3150 (1973).

[61] [BROWN-HARVARD-MIT-PADOVA-WEIZMANN INSTITUTE BUBBLE CHAMBER GROUP], Phys. Rev. **155**, 1468 (1967).

[62] [H.J. BESCH, G. HARTMANN, R. KOSE, F. KRAUTSCHNEIDER, W. PAUL and U. TRINKS], Nucl. Phys. **70**, 257 (1974).

[63] K. Gottfried and J. D. Jackson, Nuovo Cim. **33**, 309 (1964).

[64] K. Schilling, P. Seyboth and G. E. Wolf, Nucl. Phys. B **15**, 397 (1970) [Erratum-ibid. B **18**, 332 (1970)].

[65] J. Barth, W. Braun, J. Ernst, K. H. Glander, J. Hannappel, N. Jopen, F. J. Klein and F. Klein *et al.*, Eur. Phys. J. A **17**, 269 (2003).

[66] Y. Oh, C. M. Ko and K. Nakayama, Phys. Rev. C **77**, 045204 (2008) [arXiv:0712.4285 [nucl-th]].

[67] J. D. Bjorken and S. D. Drell, *Relativistic quantum mechancis* (McGraw-Hill, New York, 1964)

[68] J. D. Bjorken and S. D. Drell, *Relativistic quantum field* (McGraw-Hill, New York, 1965)

[69] W. Rarita and J. S. Schwinger, Phys. Rev. **60**, 61 (1941)

[70] R. HAGEDORN, *RELATIVISTIC KINEMACITS* (W. A. BENJAMIN, INC 1964)

[71] Edited by M. Nikolic, *KINEMATICS AND MULTIPARTICLE SYSTEM* (GORDEON AND BREACH Science Publishers 1968)

[72] E. Byckling and K. Kajantie, *Particle kinematics* (John Wiley & Sons Ltd 1973)

[73] Particle Data Group, J. Phys. G: Nucl. Part. Phys. **37** (2010) 075021

[74] V. E. Barnes, P. L. Connolly, D. J. Crennell, B. B. Culwick, W. C. Delaney, W. B. Fowler, P. E. Hagerty and E. L. Hart *et al.*, Phys. Rev. Lett. **12**, 204 (1964).

[75] B. Aubert *et al.* [BABAR Collaboration], Phys. Rev. Lett. **97**, 112001 (2006) [hep-ex/0606039].

[76] H. -Y. Ryu, A. I. Titov, A. Hosaka and H. -C. Kim, arXiv:1212.6075 [hep-ph].

[77] M. Gell-Mann and Y. Neèman, *The Eight-fold Way* (W.A. Benjamin, Inc. NY, 1964).

[78] C. Alt *et al.* [NA49 Collaboration], Phys. Rev. Lett. **92**, 042003 (2004) [hep-ex/0310014].

[79] Lei Guo, the presentation in International Workshop on New Hadron Spectroscopies (2012)

[80] Sandy Donnachie *et al*, Pomeron Physics and QCD, Cambridge university press, 2002.

Index